Inside-out electrical capacitance tomography for downhole multiphase flow evaluation

Kjærsgaard-Rasmussen, Jimmy

Publication date:
2010

Document Version
Publisher's PDF, also known as Version of record

Inside-out electrical capacitance tomography for downhole multiphase flow evaluation

PhD Thesis

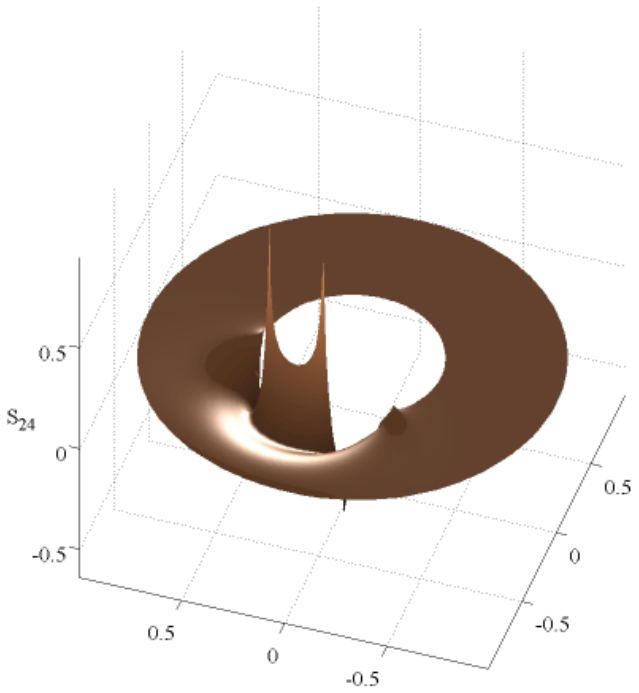

Jimmy Kjærsgaard-Rasmussen
April 2010

DTU Mechanical Engineering
Department of Mechanical Engineering

Preface

The research documented in this dissertation was mainly performed at Welltec, Allerød and at the Technical University of Denmark from November in 2006 to April 2010. Some related work, which is presented in the paper included in this dissertation, was performed in the period from January 2008 to April 2008 during a visit at the School of Electrical and Electronic Engineering at the University of Manchester.

I would like to thank Lektor Knud Erik Meyer for much appreciated guidance and many discussions and Professor Wuqiang Yang for giving me a crash course in ECT systems and welcoming me as part of the research group, during the brief stay in Manchester.

I would also like to thank Mathias for many discussions and assistance with countless derivations on the whiteboard as well as Anders, Torben and Søren for their excellent work and patient advice. Finally, I would like to thank the group in Manchester for a very pleasant stay.

Abstract

The management of a hydrocarbon reservoir is based on measurements made in and around the well. The available information is used as input into models of the reservoir, so as to operate the well in the most optimal way. A reservoir managers success thus depends on the quality and type of information available. The objective of the work presented in this report was to develop a method for providing high quality mobile measurements from the inside of oil wells.

It is shown that electrical capacitance tomography is a suitable method for the purpose. The conventional methods are only partially applicable, since the demands on the sensor results in a new 'inside-out' sensor geometry, where the permittivity on an annulus is reconstructed and the electrodes are placed on the inner boundary. In specific, it is found that the normalization normally applied to obtain a pseudo-inverse for the sensitivity matrices, causes artifacts to appear in the reconstructed images for the inside-out geometry. A reconstruction method which can handle these problems is developed.

Sensitivity matrices for the inside-out geometry are calculated. To assist in investigating the sensitivity matrices, an analytical expression for the electric field inside the sensor is derived and subsequently an analytical expression for the sensitivity matrix is found. The analytical solution is for a slightly idealized geometry, so numerical methods are applied to obtain the sensitivity matrix for the exact sensor geometry. The numerical methods used were a finite difference method and a finite element method.

A few different reconstruction methods are employed to investigate which one to use. The recorded capacitance data are transmitted over the wireline, which is a cable used in the oil-industry to lower tools into a well and to supply the tool with power, and the data can be used to perform live tomography with linear backprojection. A customized version of Landweber was developed and is demonstrated to work very well for the inside-out geometry.

Several test setups were constructed. It is found that a resolution of 5fF is achieved and that the system is able to operate in temperatures of 120°C. The image quality of the

customized Landweber algorithm is superior to other reconstruction methods for the inside-out geometry.

The system was tested in a well under surface conditions. Live tomography could be provided over the wireline and the sections with water could be clearly identified. It was concluded that the system is ready for field-test. Three sensors were shipped for offshore field test, but unfortunately the test was canceled because of problems with the well.

Resumé

For at styre produktionen på et olie- eller gas-felt, tager man beslutninger som er baseret på målinger i og rundt om brøndene. Måledata bliver så brugt som input til modeller af reservoiret, så brønden kan styres på den mest optimale måde. At styre produktionen optimalt afhænger således af den type og kvaliteten af de data som der er tilgængelige. Målet med det arbejde der præsenteres i denne afhandling var at udvikle en metode til at kunne producere data af høj kvalitet, fra et hvilket som helst sted inden i en brønd.

Det bliver vist at ECT (Electrical Capacitance Tomography) er en metode der passer godt til formålet. Det vises at de konventionelle metoder indenfor ECT, kun er delvist anvendelige, eftersom kravene til den mobile sensor resulterer i en ny 'inside-out' sensor geometri, hvor permittiviteten rekonstrueres på en cirkelring og hvor elektroderne sidder på den inderste rand. Mere specifikt vises det, at den normalisering som normalt anvendes til at opstille en pseudo-invers for systemets sensitivitets-matrice, resulterer i artefakter i det rekonstruerede tomogram. En rekonstruktionsmetode der kan håndtere problemerne er blevet udviklet.

Sensitivitets matricer for inside-out geometrien udregnes. Som en del af analysen af sensitivitets matricer, udledes et analytisk udtryk for det elektriske felt inden i sensoren. Et analytisk udtryk for sensitivitets matricen for inside-out geometrien udledes efterfølgende. Den analytiske model er baseret på en delvist idealiseret geometri, så nummeriske metoder anvendes for at udregne sensitivitets matricerne for den eksakte sensor geometri. De anvendte nummeriske metoder var finite differences og finite elements.

Et par forskellige rekonstruktionsmetoder anvendes for at sammenligne resultaterne og finde ud af hvilke metoder er de bedst egnede. Det er muligt at opnå live-tomografi over wireline (et kabel der bruges som strømforsyning til tools og til at sænke dem ned i en brønd) med linear backprojection som rekonstruktionsmetode. En specielt tilpasset version af Landweber algoritmen blev udviklet og det blev demonstreret at den virker særdeles godt for inside-out geometrien.

Flere testopstillinger blev konstrueret. Det findes at opløsningen af kapacitans målingen er på 5fF og at elektronikken virker i en temperatur på 120°C. Billede-kvaliteten af den tilpassede Landweber teknik er bedre end for de andre rekonstruktionsteknikker for inside-out geometrien.

Systemet blev afprøvet i en brønd under overflade betingelser. Det blev vist at live-tomografi over wireline virkede ved en framerate på 10Hz og at sektioner i brønden med vand nemt kunne identificeres. Det blev konkluderet at systemet er klar til field-test. Tre sensorer blev sendt afsted til field-test på en boreplatform, men testen blev desværre aflyst på grund af problemer med brønden.

Contents

Chapter 1

Introduction

Through the life of an oil-well, the operating conditions for the well change continuously. Hydrocarbons are extracted from the reservoir and replaced by liquids (typically sea water) or gas. The reservoir is thus in constant transformation and the well itself even changes in several ways. Optimization of a well's production rate thus requires repeated logging of well parameters and subsequent intervention in the way the well is operated.

The objective of this project has been to develop a flow-logging tool, suited for wireline operations in the oil industry. A wireline is a cable used to lower tools into a well and to supply it with power. Tools can also be run on coiled tubing in which case the tools can be pushed into the well and are powered by the pressure difference between the well fluid and the fluid which is pumped through the tube and into the well, through the tool.

A wealth of wireline tools and loggers exists and the developed logging tool is intended to be able to operate in cooperation with these. Apart from being able to operate in downhole conditions, which typically means being able to withstand 300bar and 120°C, the logging tool should be as light and short as possible. Wireline operations are often preferred over coiled tubing operations because of their much smaller footprint and because most wireline equipment can be transported by helicopter, as opposed to by ship. Making a tool that is shorter makes it easier to handle and to include in long tool strings and making it lighter has the same advantages.

To perform logging and/or intervention jobs, tools can simply be lowered into the well on the wireline, if the borehole is relatively vertical. Many modern wells are substantially horizontal though. The horizontal section of such wells, can stretch for several kilometers through the hydrocarbon-rich layer of the reservoir. To reach into such hor-

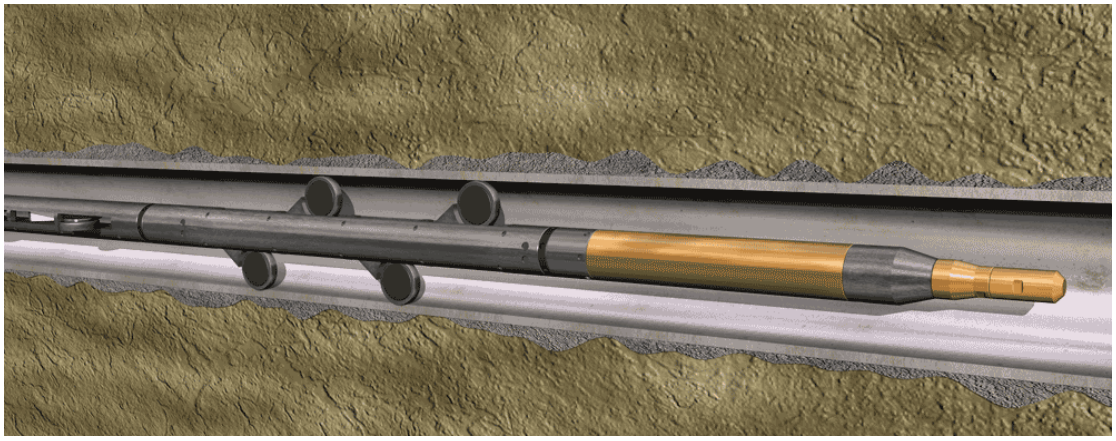

Figure 1.1: The illustration shows a toolstring inside a cased well. The section of the toolstring which has wheels is a part of the tractor. Several other sections can be mounted on the toolstring. The choice of sections to mount, depends on which kind of job to perform with the toolstring.

izontal sections of a well, mobile robots, called tractors, are deployed in the well, to push all sorts of equipment into the horizontal part of the well.

As part of a tool string, the logging tool will need to be able to be powered by the internal power bus of the tool string, as well as connect to the internal communication protocol to send data over the wireline. The bandwidth for data-traffic over wireline is limited, so it is important to consider whether it is possible to transmit all sensor-data or if it should be stored in the sensor. Typical sizes for tools are either 53.9mm or 79.3mm in outer diameter. Since the tool will have to be able to withstand large pressures, the inner diameter of the tool is even smaller. This causes some constraints for the electronics of the logging tool which will have to fit on circuit boards no wider than 45mm or 70mm.

1.1 Logging - prior technology

Logging tools provide valuable information about the well and the formation in the nearest vicinity of the well and a multitude of different logging sensors exist.

The most simple tools include mechanical calipers which measure the inner geometry of the casing and casing collar locators (CCL) which identify locations where the sensor passes a junction between two sections of casing. Slightly more advanced tools measure pressure and temperature and even record sound. A few types of sensors can provide information about the formation in the vicinity of the well. The resistivity of the formation can be measured by current injection and the density can be logged by radiation based sensors.

A subgroup of sensor tools focus on measuring properties of the flow inside the well. Some of them provide flow rate measurements of each flow component and others aim to represent a rheological cross-section of the flow. A collection of sensors which are run by Aker, Halliburton and Sondex [1] use bow springs which protrude from the sensor body and into the flow. Resistance probes, capacitance probes or mechanical spinners are mounted on the bow springs, providing point measurements of conductivity, impedance or flow speed, respectively. A rheological cross-section is created on the basis of an assumption of a layered flow and then interpolating the point measurements to the entire domain inside the well bore.

The spinner approach to measuring volume flow has also been adopted in one of Schlumberger's [1] sensors; their Flow Scanner. The flow scanner deploys a set of five sensors on a mechanical arm. The five sensing areas are situated along a straight line, vertically in the center of the well bore. In each area, the flow is investigated by a spinner, an impedance probe and an optical probe. Again, a rheological cross section is created based on an assumption of a layered flow.

Volume flow measurements are thus mainly based upon the use of mechanical spinners and the rheology of the flow in the well is based upon local measurements and assumptions about the flow regime.

1.2 Choosing a logging candidate

The objective of developing a flow logging solution was not accompanied by any suggestions, as to the method. Finding a viable candidate for that task thus became the first milestone of the project. The final result of the flow measurement would ideally be the flow-component and flow velocity at each point in a cross-section of the flow. This would enable the calculation of flow rates of each flow-component as well as provide a means to inspect the places of inflow/outflow in the well-casing. None of the considered candidates were able to provide this ideal result. Finding the best candidate thus became a question of finding the best compromise.

To evaluate the many different viable candidates, each candidate was evaluated according to a compact list of parameters and subsequently awarded a final score, as the weighted sum of each parameter:

$$s_j = \sum_i v_{ji} w_i, \tag{1.1}$$

[1] Aker, Halliburton, Sondex and Sclumberger are all major service companies in the oil industry.

where s_j is the score for the j'th candidate, v_{ji} is that candidates score on each of the i parameters and w_i is the weight of that parameter in the evaluation.

Evaluation parameters

To provide a means of comparing the candidates, a compact list of evaluation parameters was constructed. Each parameter was given a weight (from 0 to 10), according to its perceived importance for the success of a given candidate.

Measurement type

The reviewed methods mainly provided either measurements of the velocity field or of the cross-sectional distribution of some component-specific parameter. There was no preference as to which variable was the most important, so each of the two end-results, **velocity** or **tomography**, were given a weight of 5.

Resolution

The first evaluation parameter was the **resolution** of each method, meaning the spatial density of the resulting measurements. For the tomographic methods as well as the methods which provide cross-sectional velocity fields, resolution was interpreted as the size of structures the method can resolve.

The methods which provide point-measurements naturally received low scores in this parameter. The resolution of the method was perceived as an important parameter and was given a weight of 8.

Safety

The second evaluation parameter was **Safety**. The definition of safety for each method means both how many safety precautions would need to be taken by R&D personnel during development and how many precautions would need to be taken by field engineers during operation of the final product. The safety was given a weight of 5.

Robustness and size

Robustness and size was the third and final parameter. The challenges for a logging tool is that it has to be small and robust. It is also important that it should not be able to get stuck on valves or other structures inside the well. Naturally it is an important

consideration that the sensor is able to be designed in such a way that it can comply with these demands.

Well conditions are harsh. Pressures of several hundred Bar and temperatures over 100°C are common. For any of the sensing-methods, the electronics would have to be able to withstand well-conditions as well as to fit inside a cylindrical housing with a diameter less than 8cm. Robustness and size was considered the most important parameter and was given a weight of 10.

Evaluation of candidates

Electrical capacitance tomography

Electrical capacitance tomography is a measurement technique that produces cross-sectional images of the permittivity distribution inside a chosen domain[1, 2]. Capacitance measurements are performed by simple electronic circuits[3] between electrodes, which are placed at the boundary of the domain of investigation. Based on a numerical model of the sensitivity of each capacitance measurement to permittivity changes, a tomogram of the permittivity distribution is calculated. Chapter 2 describes the method in further detail.

Resolution: 5
The resolution of an ECT system is moderate. The images themselves can have a high resolution, but flow-structures tend to become blurred by the reconstruction algorithms.
Safety: 10
There are no safety issues with this method.
Robustness and size: 10
It seems that it would be possible to fit the needed electronics inside a tractor housing and to make sure that they can withstand well-conditions.

Ultrasonic tomography

As with any kind of tomography, this method utilizes measurements at the boundary of a reconstruction domain to create a cross-sectional image (tomogram) of some variable. Ultrasonic transducers are placed in a circle around the domain of investigation.

Ultrasonic tomography can be performed in different modes, which are able to provide images of slightly different parameters inside the domain of investigation [4].

Transmission mode [5] works under a hard-field assumption and the reconstruction is thus very similar to e.g. X-ray tomography. The underlying model for the sound-waves is particle like in nature. The imaged variable in transmission mode is some combination (depending on the choice of reconstruction algorithm) of the speed of sound of the medium and the acoustic absorption coefficient of the medium. Reconstruction uses the Radon transform.

Reflection mode is slightly more sophisticated than transmission mode, since it is based an a more wave-like model for the sound-waves. In reflection mode, the imaged variable is the ultrasonic reflectivity inside the domain of investigation.

Resolution: 8
The resolution is high, but limited by the wavelength of the ultrasonic waves.
Safety: 10
There are no safety issues with this technique.
Robustness and size: 7
The greatest concern with an ultrasonic approach lies in the signal acquisition. A turbulent flow, filled with bubbles and dirt, may prove a great challenge to acquire usable echoes from. As well as the flow, the short distance to the metal casing and the risk of echoes traveling back and forth between the casing and the tool string would be an issue.

Finally advanced electronics would have to fit inside the housing along with the transducers, since sending large amounts of data over the wireline is not an option.

Ultrasonic (speckle) velocimetry

Ultrasonic velocimetry provides images of the velocity field in the imaging plane. An ultrasonic plane wave signal is emitted from a transducer array. The return signals are then recorded by each transducer in the array and processed into an 'instantaneous' image of the ultrasonic reflectivity via traditional delay-and-sum beamforming. The mean velocity of speckles in the image is then obtained by correlation of subsequent beamformed images [6].

Resolution: 7
The resolution of the ultrasonic velocimetry technique is high and only limited by the wavelength of the sound waves.
Safety: 10
There are no safety issues with this system.

Robustness and size: 7
The concerns are the same as with the ultrasonic tomography technique. The hardware for velocimetry would be slightly less bulky, but the differences are negligible.

Particle image velocimetry

Particle image velocimetry provides a measurement of the velocity field on a plane of investigation. A laser-sheet is produced by a pulsed laser and recorded by a camera[7]. Subsequent images are correlated, creating measurements of the local velocity at places with 'spots' in the image which are recognized from one image to the next[8]. A comparison with ultrasonic speckle velocimetry will reveal that the acquired images are processed in very similar ways.

Resolution: 10
The resolution is very high. The velocity field has sub-pixel resolution since the intensity profiles are curve-fitted to find continuous-space-center of peaks.
Safety: 8
There are no serious safety issues, but since the technique involves high voltage and high intensity laser-light, there are a few precautions that would need to be taken.
Robustness and size: 5
It seems it would be challenging to fit a high powered lases-system inside of a relatively small cylinder, especially considering the high temperature under which it is required to operate. Another issue is that any optical method will have problems in dirty bubbly flows, which must be expected in an oil well.

Mechanical spinners

Mechanical spinners are traditional anemometers. Local velocity measurements are performed by interacting mechanically with the flow at discrete locations. The angular velocity of each spinner is a function of the flow-velocity where the sensor is placed[9].

Resolution: 1
The resolution is very poor with mechanical spinners. Besides performing single point measurements, it is not possible to perform several measurements in a fine grid. Spinners need to be large enough to interact with the flow, so in order for measurements to be substantially independent, they must be spatially well dispersed.
Safety: 10

There are no safety issues.

Robustness and size: 5

Spinners are well proven for down-hole applications, but they need to be mounted on some mechanically protruding parts of the tractor and will tend to get stuck on well structures as well as in sand and shale.

Constant temperature anemometry

Constant temperature anemometry is a well known technique for the measurement of the local velocity of fluids[10]. A small piece of wire or film is kept at a constant temperature by the sensor electronics while being cooled by the surrounding flow. If the temperature of the flow is constant, the power needed to keep the wire at constant temperature is a function of the flow-velocity.

Resolution: 2

The resolution is poor since the technique provides only point measurements. Sensor heads can be placed closely together, since the are relatively small and only interact weakly with the flow.

Safety: 10

There are no safety issues with this technique.

Robustness and size: 5

The wire or film in the sensor needs to interact directly with the flow, so they would be prone to mechanical damage.

Laser-Doppler velocimetry

Laser-Doppler anemometry is a non-invasive measurement technique that measures the flow velocity in a small volume which is illuminated by two laser-beams[11]. An interference pattern is created inside the flow, by superimposing the two continuous mode laser-beams (typically originating from a single laser beam which is passed through an optical splitter). The investigation volume will contain light-fringes caused by the interference. Particles that scatter light at the high-intensity fringes will cause the light to Doppler-shift which is recorded by the sensor.

Resolution: 2

The resolution of the laser Doppler technique is poor since it is a point-measurement technique. Measurements can be placed very closely together though since the size of

investigation volumes is small and they do not interact with the flow.

Safety: 8

The same issues as with particle imaging velocimetry are relevant.

Robustness and size: 5

The same issues as with particle imaging velocimetry are relevant.

Radio frequency resonance

Radio frequency resonance is a global measurement of (a part of) the electrical impedance of a section of flow[12, 13]. The impedance between two electrodes which surround the flow is measured and the fractions of water and oil are derived directly as a function of the impedance.

Resolution: 0

The RF resonance measurement has no resolution - it is a mean over the entire volume of investigation.

Safety: 10

There are no safety issues.

Robustness and size: 10

The electronics for a radio-frequency resonator device would be very easy to fit inside a tractor housing and it would interfere as little as possible with the flow.

Radiation tomography

Radiation tomography covers both neutron, X-ray and gamma tomography[14, 15]. They are all hard field tomographic techniques which employ the Radon transform for the creation of tomograms. Radiation transceivers are placed in a circle and the flow composition inside the circle is investigated.

Resolution: 8

The resolution of hard-field tomography methods is high.

Safety: 5

There are several safety issues with these methods. The use of neutron-, gamma- or X-rays would cause a lot of safety procedures to be obeyed and would cause very high demands on the design of the sensor housing.

Robustness and size: 0

It would be extremely difficult to design the signal processing hardware and the trans-

ducers for these methods such that they could fit inside a tractor housing, not to mention endure the pressures and temperatures inside an oil-well.

Scorecard

The results of the scorecard are shown in table 1.1. Electrical capacitance tomography received the highest overall score (even through several different versions of the scorecard) and ultrasonic methods ranked highly as well.

Property	Velocity	Tomography	Resolution	Safety	Robustness and size	Score
Weight	**5**	**5**	**8**	**5**	**10**	
Electrical capacitance tomography	0	10	5	10	10	**7,3**
Ultrasonic tomography	0	10	8	10	7	**7,1**
Ultrasonic velocimetry	10	0	7	10	7	**6,8**
Particle image velocimetry	10	0	10	8	5	**6,7**
Mechanical spinners	10	10	1	10	5	**6,3**
Constant temperature anemometry	10	0	2	10	5	**5,0**
Laser-Doppler velocimetry	10	0	2	8	5	**4,7**
RF resonance	0	0	0	10	10	**4,5**
Radiation tomography	0	10	8	5	0	**4,2**

Table 1.1: The table shows a comparison of the initial list of candidates for a logging technology.

The choice of an ECT system as the logging solution, means that the sensor will be producing tomograms as an output. Measuring volume flow rates of the flow components will not be achieved by tomography alone. Measurement of volume flow rates by correlation of tomograms from 2 ECT systems has been reported though [16, 17].

The reason that ECT received the top score is mainly that the hardware which is needed by the sensor is likely to be able to meet the demands for a wireline sensor. No experimental results from using ECT systems in a high temperature was found though, so that will need to be tested (see chapter 7).

Chapter 2

ECT theory and history

Electrical Capacitance Tomography is a non-invasive imaging technique. It is possible to construct images relatively quickly with an ECT system (ie. at 10-100Hz), so live monitoring of many industrial processes is possible.

Electrical Capacitance Tomography was developed at UMIST[1] in the 1980's [1, 18, 19]. Companies such as Tomoflow and Process Tomography Limited can provide off-the-shelve ECT systems.

This chapter presents the general theory of electrical capacitance tomography. Later chapters will provide information about more specialized parts of the project such as the capacitance measurements and image reconstruction algorithms.

2.1 Prior work

Electrical capacitance tomography (and the related electrical impedance tomography) is an increasingly widely adopted measuring technique. Tomogram literally means a cross-sectional image, but ECT is also moving into volume imaging ([20],[21]) and the 'tomography' part of the name is in some cases probably used more because of tradition than because it is an illustrative description.

The foundations of ECT are described very briefly by Huang, Plaskowski, Xie and Beck in 1988[1] and by Xie, Plaskowski and Beck in 1989[2]. An 8 electrode system is demonstrated to produce tomograms of sand/air distribution. The early system which is described uses some very simple circuits. A single capacitance-to-voltage transducer is used with a multiplexer to measure the 28 electrode combinations. All

[1]University of Manchester Institute of Science and Technology. In 2004 UMIST merged with (Victoria) University of Manchester to become University of Manchester.

control of analog-to-digital conversion, the multiplexer and image processing (linear backprojection) was done on a computer. The short article concludes that ECT can provide fast data collection, but the IBM PC, or the algorithm used in the setup, would spend 10 seconds reconstructing each tomogram, so live imaging was not yet possible.

The capacitance resolution of ECT circuits need to be able to resolve capacitance changes in the femto-farad (**fF**) range. Since the magnitude of the measured capacitances is so small, it is essential that capacitance measurement methods for ECT are stray-immune. This means that they should not be affected by the capacitance from either side of the capacitor and ground[22, 23]. The two dominant capacitance measurement methods, charge transfer and the AC-based technique, were treated by Yang in an article from 1995[3]. It is shown that the AC-based technique is superior to charge transfer circuits in signal-to-noise ratio and resolution, but it is also noted that a disadvantage of the AC-based method is that it is both complicated and expensive. The charge transfer technique was described in more detail by Huang et al. in several articles [19, 22, 23] and the AC-based technique was treated by Yang [24]. Other techniques were described by Lu, Shao and Gou [25] who described a high voltage method for industrial applications and by Kuhn and vanHalderen [26] who described an active differentiator-based capacitance measuring technique.

The charge transfer technique is, by far, the most simple method, which is an advantage for a downhole application since size and robustness is an important design parameter. The drawback is the lower capacitance resolution. The circuits measure the capacitance between electrodes, so if the electrodes are large, the resolution of the capacitance measurement need not be as high. Avoiding to use a high number of electrodes, will make it possible to use larger electrodes and thus to use capacitance measuring circuits with a lower resolution. The drawback of this solution is that a smaller number of measurements is achieved, which has consequences for the reconstruction.

The forward ECT problem is described in detail by Alme and Mylvaganarn [27], who also focuses on the design of ECT sensors. It is shown that the forward problem can be modeled as a 2D problem as long as the electrodes are long enough and the permittivity contrast is not too large. The ability to treat the measurements as integrals on a 2D surface simplifies the mathematical models. This dissertation will present a new sensor geometry and it is uncertain whether the results of the article extend to this geometry, but it will be assumed that, as long as the length of the electrodes is sufficiently large, this is indeed the case.

The mathematical foundations of tomogram reconstruction was treated by Yang and Peng in 2003 [28] where an excellent overview of several different reconstruction tech-

niques was provided. The theory of each technique is treated and they are compared through both simulation and experiment with a square ECT sensor.

Several reconstruction methods are used for ECT. Linear backprojection, Landweber and Tikhonov seem to be the most common, but neural network approaches, fuzzy logic approaches and countless other approaches have been reported. An extended Tikhonov reconstruction method is treated by Lei, Liu, Li and Sun [29] and an adaption of Landweber reconstruction for ECT imaging is demonstrated by Jang et al. and Lu et al. [30, 31]. Both of these report good results, but based on the huge number of reported methods for different geometries, it seems that finding a suitable reconstruction method for a new sensor geometry is a matter of trial and error.

2.2 Tomography

Tomography in general pertains to the construction of cross sectional images of bodies based on measurements at the boundary. The measurements, m_i, can be modeled as weighted integrals over the reconstruction domain:

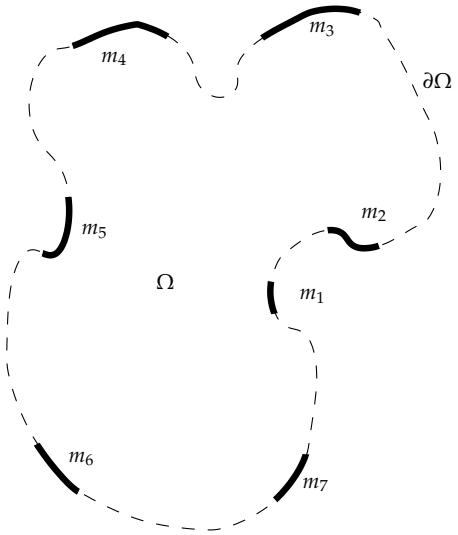

Figure 2.1: Tomography is an imaging technique. Images represent some distribution, f, on a domain Ω. The figure shows a domain, Ω, with a boundary $\partial\Omega$ in which measurements, m_i, are made. The measurements are drawn as separate lines, but they could overlap or fill the entire boundary. Usually some kind of perturbation is applied from one point along $\partial\Omega$ and the effect is measured somewhere else. Each measurement, m_i, is sensitive to different parts of the domain and this sensitivity is represented by S_i. The relationship between all these variables is represented by equation (2.1).

$$m_i = \int_\Omega f(\boldsymbol{x}) S_i(\boldsymbol{x}) \quad \mathrm{d}a \tag{2.1}$$

where Ω is the reconstruction domain, S_i are the weighting functions, $\boldsymbol{x}$ is a point (x, y) and f is the distribution to be represented by the tomogram. Equation (2.1) is a special case of a Fredholm equation of the first kind. Figure 2.1 is a generalized representation of how measurements are made at the boundary of a certain domain. The finite set of measurements are used to reconstruct a distribution inside the domain.

There are many other kinds of tomography; ultrasonic, X-ray, optical and seismic for example. The common denominator for them all is the reliance on boundary measurements of a subject and they are all thus inherently non-invasive methods.

X-ray tomography

The physical meaning of the distribution, f, varies from one kind of tomography to the next. In X-ray tomography[2] f is the density distribution and the measurements, m_i, are of the intensity of the radiation at a specific point. Each measurements samples the density along a straight line from the source to the point of measurement.

For measurement i, the sensitivity S_i is thus zero everywhere except along the line, where it has some constant value. Figure 2.2 shows a diagram of a few of such measurements. The source sends out radiation in a fan-shaped pattern, but only the radiation which has traveled along certain lines is measured. Each measurement is performed by a scintillator. The intensity of the radiation decays exponentially as a function of the absorption coefficient μ

$$I_k = I_0 e^{-\int_\Omega S_k \mu(x,y) da}$$

where I_k is the intensity measurement at scintillator number k and I_0 is the intensity at the source. A measurement m_k can thus be expressed in the same form as (2.1) where the sensitivity field has a value of zero everywhere else than along the line L_k

$$\begin{aligned} m_k &= \ln\left(\frac{I_0}{I_k}\right) = \int_\Omega S_k \mu(x,y) \quad da \\ &= \ln\left(\frac{I_0}{I_k}\right) = \int_{L_k} \mu(x,y) dl \end{aligned}$$

[2]CAT (Computerized Axial Tomography) scan, or simply CT (Computed Tomography), is a more well-known name for X-ray tomography.

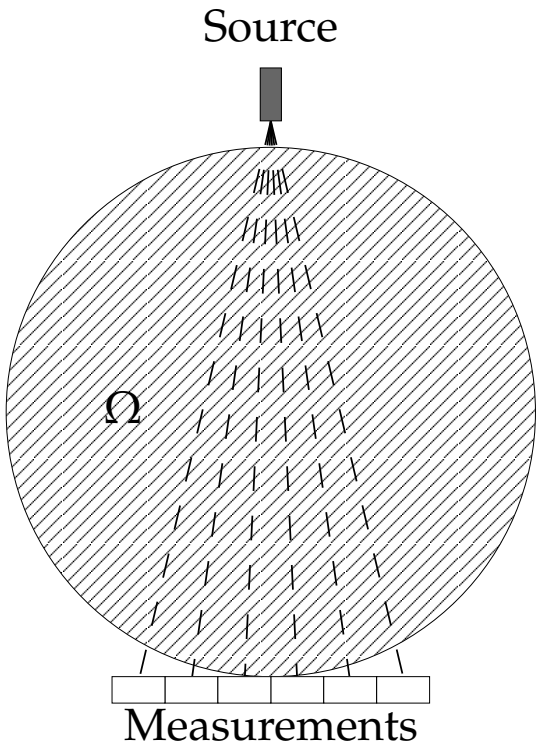

Figure 2.2: The figure shows a principal drawing of X-ray tomography. An X-ray source send radiation through a domain, Ω, in a fan-shaped pattern. The intensity of the transmitted radiation is measured at the opposite side of the reconstruction domain by an array of scintillators. By rotating the source and scintillator array, the domain can be investigated from all sides.

The sensitivity for each measurement is very well defined and only has a non-zero value in a small part of the reconstruction domain. Another very valuable feature of X-ray tomography is that the sensitivity is independent of the absorption coefficient-distribution. Tomography which relies on measurements with this kind of sensitivity method are called hard-field methods; probably because the field is not deflected/scattered. Methods where the sensitivity depends on the measured distribution are called soft-field [32, 33] methods. Many hard-field methods can use the inverse Radon transform for reconstruction of f. Soft field methods must use other methods which can often prove more problematic.

2.3 Electrical capacitance tomography

In the case of ECT, the boundary measurements, m_i, are capacitance values and the tomogram is an image of the permittivity distribution on the domain Ω. Typically, the capacitances are very small and a resolutions as high as **fF**-level are achieved by the capacitance measuring circuits of ECT systems.

A characteristic 'feature' of ECT is it's soft field imaging. Capacitance values between the electrodes are affected by permittivity values in the entire domain; the sensitivity is not localized, but spread out. The small number of measurements and the soft-field effect causes blurred images even at relatively low resolutions.

A typical ECT sensor is constructed by placing electrodes on the outside of a tube like in figure 2.3. Shielding electrodes are placed up- and down-stream of the sensor and a screen are placed on the outside of the electrodes to prevent interference from external electric fields.

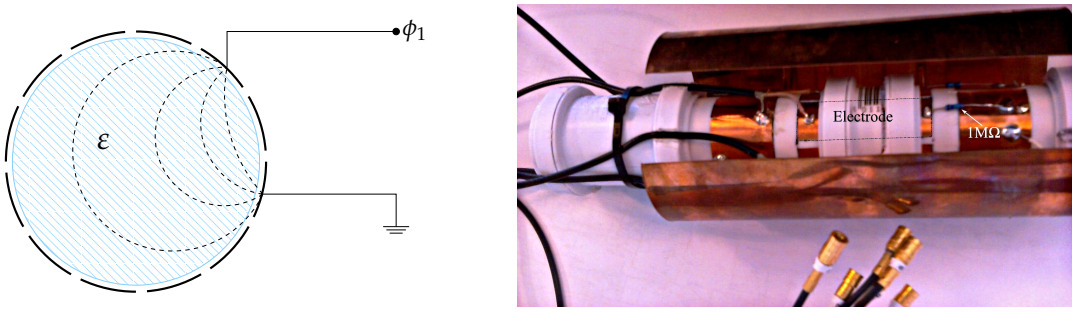

Figure 2.3: The sketch on the left figure shows 12 electrodes placed in a ring. One electrode, the source, is kept at a constant potential and the others are grounded. The capacitance between each grounded electrode to the source is then measured. On the right, a picture of a test-sensor is shown. This sensor has only 6 electrodes. The position of one of the electrodes is marked by a dashed line. On either side of the electrodes are placed screening electrodes that reach all the way around the tube.

Measurements are then made by applying an excitation signal to one electrode and measuring on another. The measuring electrode is connected to a filter that converts the capacitance to a voltage which will be explained in section 5. The capacitance measurements are made between N electrodes in the following order:

$$\begin{array}{cccc} 1 \to 2 & 1 \to 3 & \dots & 1 \to N \\ 2 \to 3 & \dots & 2 \to N & \\ \vdots & & & \\ (N-1) \to N & & & \end{array}$$

where the arrows indicate the active and measuring electrode (active $\to$ measuring) and the triangular shape shows that as each electrode is sequentially selected as the active electrode, fewer and fewer measurements need to be made. The $(N-1)$'th electrode is only used once as the active electrode and the N'th is never used. The self-capacitance is not measured and since the capacitance between electrodes i and j is equal to the capacitance between the capacitance between j and i it is only necessary

to measure either one of those. A total of $N\frac{N-1}{2}$ unique capacitance measurements then form the basis for the reconstruction.

A set of $N\frac{N-1}{2}$ capacitances can be acquired several times each second, so it is possible to use ECT for live-imaging, provided that a tomogram can be constructed before the next capacitance-set has been acquired. Since iterative reconstruction techniques are slower than linear back projection (LBP), live-imaging is typically based on LBP and thus provides only smeared images.

The paper in section 8.4 describes the construction of a compact ECT system with 6 electrodes and a geometry as described above.

2.4 The sensitivity matrix

The subject of this section will be the calculation of the Jacobian for the forward problem which is stated in general terms by (2.1). More specifically, the forward problem involves calculating a set of capacitances from a known permittivity distribution. The derivation does not depend upon any specific geometry, but for any practical examples, the conventional ECT geometry with a disk as reconstruction domain will be used. We will proceed in a fashion similar to that of Fang and Cumberbatch from 2005 [34], which gives an excellent analysis of some properties of the capacitances of ECT sensors and Fang from 2006 [35], which provides a detailed description of a perturbation-based linearization of the forward ECT problem. A conventional ECT geometry is shown in figure 2.4(a). The reconstruction domain is a disk and the electrodes are placed on the outer rim of the disk, inside a grounded screen.

The electric potential inside the sensor depends on the boundary conditions. The screen is grounded as are most of the electrodes, except one. The potential, u_j, on electrode j, when a potential is applied to the i'th electrode, can be expressed by the Kronecker delta function

$$\begin{aligned} u_j &= \begin{cases} 0, & j \neq i \\ 1, & j = i \end{cases} \\ &= \delta_{ij} \end{aligned}$$

If the active electrode is electrode number 2, the potentials of all the electrodes are thus $u_1 = \delta_{21} = 0$, $u_1 = \delta_{22} = 1$, $u_1 = \delta_{23} = 0$ and so on.

The conventional way of defining the capacitance between two electrodes, is as the ratio between the charge accumulated on the electrodes and the voltage which caused

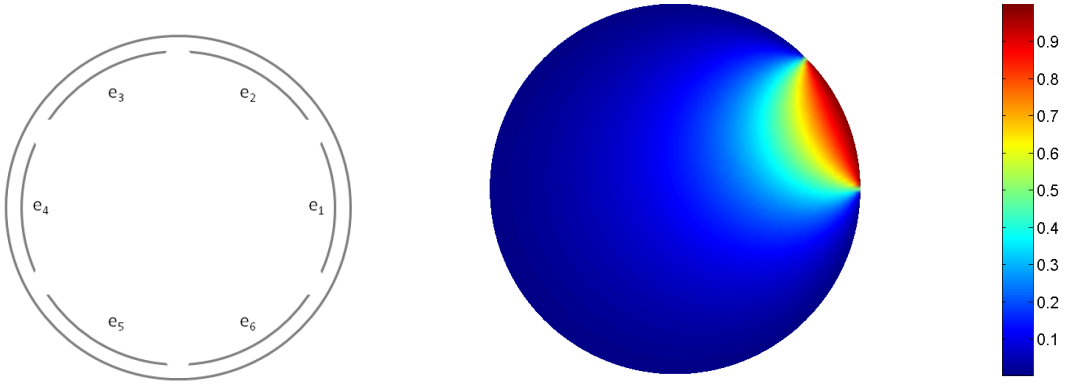

(a) Conventional ECT geometry. The capacitance between the electrodes, e_i, is dependent on the permittivity distribution on the domain Ω inside the bounding screen.

(b) The shape of the potential with the electrodes placed on the screen.

Figure 2.4: The figure shows the electrode placement and the potential distribution inside the radius of the electrodes when a single one of the electrodes has a potential of 1 and the rest are grounded.

the charge to build up.

$$c = \frac{q}{\phi} \tag{2.2}$$

The continuity equation facilitates a calculation of the charge, q, from the gradient of the potential field ϕ, so, with Maxwell's equations, (2.2) can be expanded, so it only depends, explicitly, on the potential. The continuity equation will be used several times later, so here it is in its two dimensional form (where it is equivalent to Green's theorem) in vector notation. Integrating the divergence of the field, $\boldsymbol{F}$, over a surface Ω is equivalent to integrating the flux of F through the boundary, $\delta\Omega$.

$$\int_{\Omega} \nabla \cdot \boldsymbol{F} \quad da = \oint_{\delta\Omega} \boldsymbol{F} \cdot \boldsymbol{n} \quad ds \tag{2.3}$$

The charge, q_{ij}, on the electrode e_i caused by the potential u_j is then

$$q_{ij} = \oint_{\delta e_i} \varepsilon \nabla u_j \cdot \mathbf{n} \quad dl \tag{2.4}$$

where $\varepsilon = \varepsilon(x, y)$ is the permittivity distribution.

The final object of these derivations, the sensitivity matrix, can be constructed numerically from (2.4). The sensitivity matrix is the Jacobian for the system and can be expressed as

$$[S]_{ip} = \frac{\partial}{\partial \varepsilon_p} q_i(q).$$

So the element ip of the Jacobian is the derivative of the i'th charge with respect to the p'th basis function for the permittivity.

By calculating the change in charge caused by perturbations in the permittivity distribution, the sensitivity matrix can be constructed. Numerically that would involve solving (2.4) for many different permittivity distributions which would be an expensive way to obtain the sensitivity matrix. Fortunately a much faster way to calculate the sensitivity matrix which involves only a single solution to (2.4), will be derived.

The simple, but slow, method can be important though, since it provides a way to experimentally measure the sensitivity matrix. This would be done by placing a small object of high permittivity inside the sensor, at a specified point in the reconstruction domain. By measuring the capacitance/charge and recording the position of the high-permittivity object an empirically constructed sensitivity matrix can be obtained.

Here we will continue with the derivation of a fast numerical approach. The potential is the solution to

$$\nabla \cdot [\varepsilon \nabla u_i] = 0 \tag{2.5}$$

where u_i is the potential field caused by applying a potential to electrode i and keeping the others grounded. At the boundary of the domain, Ω, the electric field is perpendicular to the boundary. This condition is valid both at the screen and at the electrodes.

$$\begin{aligned} u_i &= \delta_{ij} && \text{on} \quad e_j \\ \varepsilon \nabla u_i \cdot n &= 0 && \text{on} \quad \delta\Omega \end{aligned}$$

where e_j is electrode j. The field u_i is now used as a test function to find the charge q_{ij} through a weak solution to (2.5). Notice that in (2.4) the potential is applied to electrode j and the integral is on the boundary around electrode i.

The starting point for theses derivations was to apply a potential on e_j and then integrate around e_i to calculate the charge on that electrode.

The path for the integral can be moved arbitrarily close to the electrode, so if a field with a value of 1 on the integration path is included, the value of the integral will not change (see figure 2.5). Since

$$u_i = 1 \quad \text{on} \quad e_i,$$

the following variation of (2.4) is valid.

$$q_{ij} = \int_{\delta e_i} \varepsilon(\nabla u_j) u_i \cdot \mathbf{n} \quad dl \tag{2.6}$$

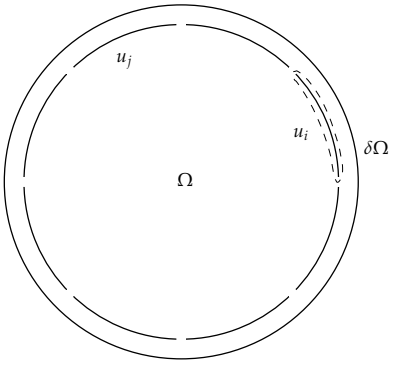

Figure 2.5: The dashed line shows the contour, δe_i, along which the integral is evaluated. The original potential was applied to electrode j. Since the integral in (2.6) is evaluated along δe_i, the value of the integral will not change of a factor of u_i is included; when δe_i is moved closer to the electrode, u_i approaches 1.

There are now two fields inside the integral. The original expression contained only the field from electrode j and now the field from electrode i has been added. With Green's theorem, (2.6) can be converted to an area integral.

$$\begin{aligned} q_{ij} &= \int_\Omega \nabla \cdot [\varepsilon(\nabla u_j)u_i] \quad da \\ &= \int_\Omega \varepsilon(\nabla u_i)\cdot(\nabla u_j) + u_i \nabla \cdot [\varepsilon \nabla u_j] \quad da \end{aligned}$$

Equation (2.5) ensures that the second term vanishes.

$$q_{ij} = \int_\Omega \varepsilon(\nabla u_i)\cdot(\nabla u_j) \quad da \tag{2.7}$$

Equation (2.7) is an expression for the charge, and hence the capacitance between two electrodes (see (2.2)). It is an important result but nothing new has yet been revealed.

The total charge on an electrode depends on the two solutions to (2.5). One with the potential δ_{ij} on the electrodes and the other with the potential δ_{ji}.

As already mentioned, the sensitivity matrix is the Jacobian of the system and we will now proceed to find the Jacobian by linearizing (2.7).

Adding a small perturbation to ε, leads to small changes in the resulting potentials.

$$\begin{aligned} \tilde{\varepsilon} &= \varepsilon + \delta\varepsilon \\ \tilde{u_k} &= u_k + \delta u_k \end{aligned}$$

The perturbation is considered to be 'small' and constrained such that it can have a non-zero value only on the interior of the domain Ω. On the boundary, $\delta\Omega$, of the

domain the perturbation vanishes. The resulting change in the charge is

$$\begin{aligned}\delta q_{ij} &= \tilde{q}_{ij} - q_{ij} \\ &= \int_\Omega \tilde{\varepsilon}(\nabla \tilde{u}_i)\cdot(\nabla \tilde{u}_j) \quad da \quad - \int_\Omega \varepsilon(\nabla u_i)\cdot(\nabla u_j) \quad da \\ &= \int_\Omega \delta\varepsilon(\nabla \tilde{u}_i)\cdot(\nabla \tilde{u}_j) + \varepsilon[\nabla u_j \cdot \nabla \delta u_i + \nabla \delta u_j \cdot \nabla u_i + \nabla \delta u_j \cdot \nabla \delta u_i] \quad da \end{aligned} \tag{2.8}$$

The last term inside the square brackets is second order in the perturbation and is ignored.

$$\delta q_{ij} = \int_\Omega \delta\varepsilon(\nabla \tilde{u}_i)\cdot(\nabla \tilde{u}_j) + \varepsilon[\nabla u_j \cdot \nabla \delta u_i + \nabla \delta u_j \cdot \nabla u_i] \quad da$$

The fields, u_k, are solutions to (2.5), so the second term in the integral in (2.8) can be rewritten with the following identity.

$$\begin{aligned}\nabla \cdot [\varepsilon \delta u_k \nabla u_l] &= \varepsilon \nabla \delta u_k \cdot \nabla u_l + \delta u_k \nabla \cdot [\varepsilon \nabla u_l] \\ &= \varepsilon \nabla \delta u_k \cdot \nabla u_l\end{aligned}$$

Green's theorem is now utilized to convert the second term of the integral back into a closed path integral around electrode j.

$$\begin{aligned}\delta q_{ij} &= \int_\Omega \delta\varepsilon(\nabla \tilde{u}_i)\cdot(\nabla \tilde{u}_j) + \nabla \cdot [\varepsilon \delta u_i \nabla u_j + \varepsilon \delta u_j \nabla u_i] \quad da \\ &= \int_\Omega \delta\varepsilon(\nabla \tilde{u}_i)\cdot(\nabla \tilde{u}_j) \quad da \quad + \quad \oint_{\delta e_j} \varepsilon \delta u_j \nabla u_i \cdot \mathbf{n} \quad dl + \quad \oint_{\delta e_i} \varepsilon \delta u_i \nabla u_j \cdot \mathbf{n} \quad dl\end{aligned}$$

Since the perturbations, δu_k, has a value of zero on δe_l the closed path integral vanishes. The single remaining term is now expanded.

$$\begin{aligned}\delta q_{ij} &= \int_\Omega \delta\varepsilon(\nabla \tilde{u}_i)\cdot(\nabla \tilde{u}_j) \quad da \\ &= \int_\Omega \delta\varepsilon[(\nabla u_i)\cdot(\nabla u_j) + (\nabla \delta u_i)\cdot(\nabla u_j) + (\nabla u_i)\cdot(\nabla \delta u_j) + (\nabla \delta u_i)\cdot(\nabla \delta u_j)] \quad da\end{aligned}$$

Again, the second order terms and the third order term are dismissed. The result a surprisingly simple estimate of the change in charge caused by the perturbation $\delta\varepsilon$.

$$\delta q_{ij} = \int_\Omega \delta\varepsilon(\nabla u_i)\cdot(\nabla u_j) \quad da \tag{2.9}$$

The occurrence of the second field inside the integral in (2.6) was allowed since it did not alter the value of the integral; it had a value of 1 everywhere along the contour integral. After the conversion to an area integral, both fields have an effect on the value of the integral. It is not intuitively clear why the charge on electrode i, from a potential on j can be derived from what the field would look like if the potential was on i instead. This expression, though, does state the symmetry of the charge (capacitance), $q_{ij} = q_{ji}$, very explicitly.

2.5 Discretization

It is useful to think of (2.9) as a projection of a kernel, $(\nabla u_i) \cdot (\nabla u_j)$, onto the perturbation, $\delta\varepsilon$. After choosing a basis in which to express the perturbation, the change in the charge can be calculated in a piecewise manner by projecting onto one basis function of the perturbation at a time.

Before choosing a basis, (2.9) will be discretized. In polar coordinates (r, θ) an equidistant $[M \times N]$ grid becomes

$$\begin{aligned} r_m &= \frac{R}{M}(m-1) \\ \theta_n &= \frac{2\pi}{N}(n-1) \\ da_k &= \frac{2\pi}{N}\frac{R}{M}r_k \end{aligned}$$

where m is the index for the discretized radius, n is the index for the discretized angle, M is the number of elements of the r_m vector, N is the number of elements in the θ_n vector and $k = (m, n)$ for a more compact notation. Equation (2.9) can be written

$$\delta q_{ij} = \sum_k \delta\varepsilon_k \nabla u_i(r_k, \theta_k) \cdot \nabla u_j(r_k, \theta_k) da_k$$

where $\delta\varepsilon_k$ value of the permittivity change at the k'th pixel. The sum clearly shows the piecewise manner in which the change in charge is calculated. The sensitivity matrix is now defined as

$$S_{ik} = \nabla u_x(r_k, \theta_k) \cdot \nabla u_y(r_k, \theta_k) da_k \tag{2.10}$$

Since we, from this point onwards, will not be concerned with the individual potentials, the electrode-pair will now have a single index i such that $i = 1$ corresponds to electrodes 1 and 2 , $i = 2$ corresponds to electrodes 1 and 3 and so forth. The index of the individual potentials is indicated by the indexes x and y in the equation. The sensitivity matrix now has two indexes and the charge and the permittivity changes will each have a single index.

$$\delta q_i = \sum_k \delta\varepsilon_k S_{ik}$$

where S_{ik} is the sensitivity of the charge for electrode-pair i. The sum can be written more compactly in matrix notation.

$$\boldsymbol{\delta q} = \boldsymbol{S}\boldsymbol{\delta\varepsilon} \tag{2.11}$$

The linearized and discretized model of the ECT system in (2.11) is the basis of reconstruction of the permittivity distribution. Since the equation have been linearized it

is important to calibrate the system such that permittivity distributions can be considered to be perturbations of a $\boldsymbol{\varepsilon}_0$. The linearization usually also includes a normalization, which is shown here and discussed in section 4.1.

The total charge for electrode-pair i is

$$q_i = q_i^0 + \boldsymbol{S}_{ik}\left(\boldsymbol{\varepsilon}_k - \boldsymbol{\varepsilon}_k^0\right) \tag{2.12}$$

where $\boldsymbol{q}_i^0$ is a calibration measurement and $\boldsymbol{\varepsilon}_k^0$ is the corresponding calibration distribution. The permittivity distribution, the tomogram, could then be calculated as

$$\varepsilon_j = \boldsymbol{S}_{ij}^{-1} \cdot (\boldsymbol{q}_i - \boldsymbol{q}_i^0) + \varepsilon_j^0$$

but S is rarely a square matrix and thus, does not have an inverse. A closed form solution can thus not be found. Originally we were interested in capacitance values. By cleaning up the notation and normalizing the equation with another calibration measurement, the capacitance will re-appear in the equation. The gray-level vector, $\boldsymbol{g}$ and the normalized capacitance $\tilde{c}$ are defined by a 'high' and a 'low' calibration set, $(c_{high,i}, \varepsilon_{high,i})$, and $(c_{low,i}, \varepsilon_{low,i})$.

$$g_j = \frac{\varepsilon_j - \varepsilon_{low,j}}{\varepsilon_{high,j} - \varepsilon_{low,j}} \qquad \tilde{c}_i = \frac{c_i - c_{low,i}}{c_{high,i} - c_{low,i}} = \frac{q_i - q_{low,i}}{q_{high,i} - q_{low,i}} \tag{2.13}$$

The forward problem can then be written

$$\tilde{\boldsymbol{c}}_i = \boldsymbol{S}_{ij}\boldsymbol{g}_j \tag{2.14}$$

A mathematical framework for imaging has now been presented and the continuous linearization has been discretized onto a pixel-basis.

The developed model, is for the forward problem; calculating capacitances from a known permittivity distribution. The number of pixels will usually be much larger than the number of available capacitance measurement, so the system is massively over-determined. Finding a solution to the inverse problem, which is what we are really interested in, thus promises to present quite a challenge.

Chapter 3

The Welltec Flow Imager: an inside-out ECT geometry

Up to this point, the geometry of the sensor has been considered to be the conventional configuration where electrodes are mounted on the outside of some tube and the flow is moving inside the tube. A few articles investigate other configurations and here yet another geometry is presented.

The objective of this project has been to produce a logging solution with an ability to provide live images anywhere inside an oil well. A conventional geometry has been well proven for flow imaging, but it is an impractical choice for a mobile sensor.

To provide a mobile logging solution, the sensor needs to be mounted on a tractor, so if the normal geometry was implemented, the electrodes would somehow need to be mounted outside of the tractor. It is not impossible to have some fingers sticking out in front of a tractor and against the casing wall, but the risk of getting the electrodes stuck inside the well would be high. Furthermore, the electrodes would probably have to be folded inside the tractor while it is being lowered into the well. This could cause problems with the electrodes not being placed at the same position every time and consequently a mismatch between the geometry used for calculation of sensitivity matrices and the actual geometry.

Instead mounting the electrodes on the well tractor and measuring 'inside out' seemed like a viable solution. This will make it possible to place the electrodes inside of the tractor, which has the benefit of providing protection for the electrodes and to place them close to the processing circuits.

The consequence of an inside-out geometry is that it causes the sensitivity matrices of a significantly different shape than for the traditional case. The same general theory

can of course be used to construct sensitivity matrices (and images) with this new geometry, but there are some interesting artifacts that need to be investigated. Also, since the sensitivity matrices (the Jacobian) has been significantly altered, it is possible that reconstruction approaches that work well for a conventional geometry are not optimal for an inside-out geometry.

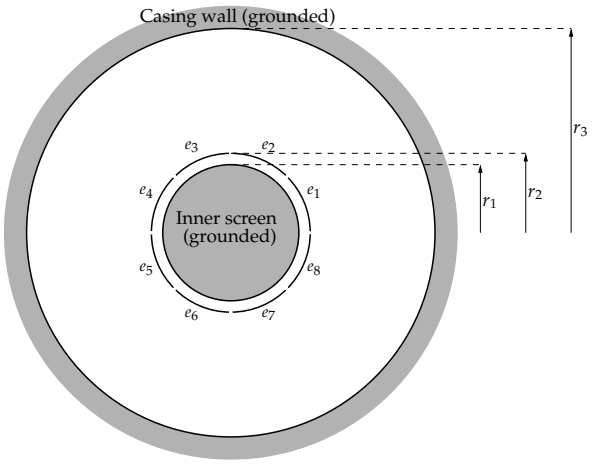

Figure 3.1: With an inside-out geometry, there are two grounding screens. One grounding screen is placed close to and inside of the electrodes and the other screen is placed outside of the electrodes. The domain of reconstruction is the area between the electrodes and the outer screen. To isolate the electrodes electrically from the reconstruction domain, they are mounted on the inside of a non-conducting tube which is not shown on the figure.

The reconstruction domain for the inside-out geometry is an annulus. Figure 3.4 shows how the electrodes are placed close to the inner boundary of the annulus. The permittivity inside the annulus can be reconstructed from measurements of the inter-electrode capacitances.

3.1 A sensitivity matrix for the inside-out geometry

The sensitivity matrix for the inside-out geometry was calculated by both analytical and numerical methods.

Series Solution

For both the conventional and the inside-out geometry it is possible to obtain an analytical solution, if the boundary conditions are slightly idealized.

The analysis will be carried out for the inside-out geometry since this is the most complex of the two. The solution for a conventional geometry is very similar and will be

stated without proof.

The first objective is is to derive an expression for the potential inside the sensor. The Laplace equation must be solved on the domain $\Omega = \{(r, \theta) : r_1 < r < r_2 0 \leq \theta < 2\pi\}$.

$$\nabla \cdot \varepsilon \nabla u = 0$$

where u is the potential from electrode 1 (for now). Figure 3.2 shows the domain and the boundary condition on the inside boundary ($r = R_1$). The electrodes are placed on the inner boundary, so the boundary conditions for r are homogeneous except for on the part of the inner boundary which is occupied by the active electrode.

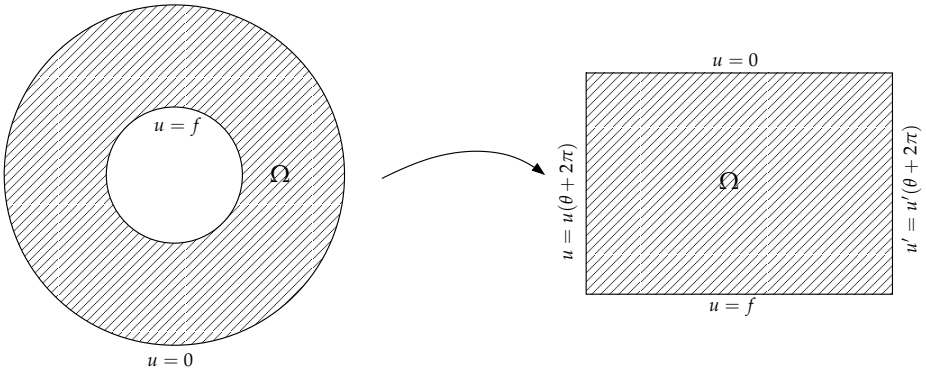

Figure 3.2: The figure shows the geometry of the reconstruction domain and the boundary conditions. The left side is illustrated in Cartesian coordinates. The inner and outer radius of the annulus is r_1 and r_2, respectively. The boundary at r_2 is grounded and at r_1 an excitation, $f(\theta)$, is applied. On the θ-boundaries, periodic boundaries are in effect.

The Laplacian in polar coordinates is

$$\Delta = \frac{1}{r}\frac{\partial}{\partial r}(r\frac{\partial}{\partial r}) + \frac{1}{r^2}\frac{\partial^2}{\partial \theta^2}$$

Looking for a product solution, $u = R(r)T(\theta)$, to the partial differential equation leads to

$$\frac{1}{r}R'T + R''T + \frac{1}{r^2}RT'' = 0$$

where R' is the $r-$derivative of R, R'' is the second $r-$derivative of R and T'' is the second $r-$derivative of T. The two functions are now separated.

$$-\frac{rR' + r^2R''}{R} = \frac{T''}{T} = k$$

where k is the separation constant.

The θ-direction yields the equation for a harmonic oscillator (at least for negative k)

$$T'' - kT = 0$$

for which the solutions to is combinations of sin and cos functions or, in the case of positive k, their hyperbolic counterparts. For $k = 0$ the solutions are first order θ-polynomials (straight lines).

For θ we are looking for solutions that can satisfy periodic boundary conditions, so we demand $k \leq 0$ since hyperbolic functions do not satisfy that demand. In the case of $k = 0$ the solution must be a constant, again because of the boundary conditions. The solution for T is then

$$T = \begin{cases} a\cos\lambda\theta + b\sin\lambda\theta, & k < 0 \\ K, & k = 0 \end{cases}$$

Furthermore, because of periodicity condition, the solution for non-zero k can be specified to functions which have a whole number of wavelengths on the interval $[0, 2\pi[$.

$$k < 0: \qquad T_k = a_k \cos k\theta + b_k \sin k\theta, \quad k \in [-1, -2, ...]$$

The coefficients a_k and b_k will be specified at a later point.

In the radial direction a second order Euler equation was obtained.

$$r^2 R'' + rR' + kR = 0$$

For non-zero (negative) k the solutions are polynomials and in the case of $k = 0$ the solution is a logarithmic function of r.

$$R = \begin{cases} a_k r^k + b_k r^{-k}, & k < 0 \\ a_0 \ln r + b_0, & k = 0 \end{cases}$$

To emphasize that the separation constant is an integer and to later avoid negative indexes, the substitution $n = -k$ will be made. Notice that since the coefficients have not yet been determined, the substitution makes no major difference to the solutions, except to swap a and b.

The constants in the solution are determined by applying the boundary conditions in the radial direction. At the outer boundary the field is grounded, so the solution must vanish ($u(r_2) = 0$).

$$0 = \begin{cases} a_n r_2^n + b_n r_2^{-n}, & n > 0 \\ a_0 + b_0 \ln r_2, & n = 0 \end{cases} \qquad \begin{matrix} b_n & = -a_n r^{2n} \\ b_0 = -a_0 \ln r_2 \end{matrix}$$

Inserting the constants and combining the two parts of the product solution gives:

$$u = a_0(\ln r_2 - \ln r) + \sum_{n=1}^{N} (r^n - r_2^{2n} r^{-n})(a_n \cos n\theta + b_n \sin n\theta)$$

The remaining boundary condition is the one at the inner boundary, $r = r_1$, where the field is fixed by the potential of the electrodes.

$$\begin{aligned} u(r_1) &= a_0(\ln r_2 - \ln r_1) + \sum_{n=1}^{N} (r_1^n - r_2^{2n} r_1^{-n})(a_n \cos n\theta + b_n \sin n\theta) \\ &= f \end{aligned}$$

The above expression is an expansion in sin and cos. Expanding the boundary condition, f, in the same basis yields:

$$f = \tilde{a}_0 + \sum_{n=1}^{N} \tilde{a} \cos n\theta + \tilde{b} \sin n\theta$$

where $\tilde{a}_n$ and $\tilde{b}_n$ are the cos- and sin expansion coefficients, respectively. Comparing the two expansions gives

$$a_0(\ln r_2 - \ln r_1) + \sum_{n=1}^{N} (r_1^n - r_2^{2n} r_1^{-n})(a_n \cos n\theta + b_n \sin n\theta) = \tilde{a}_0 + \sum_{n=1}^{N} \tilde{a} \cos n\theta + \tilde{b} \sin n\theta$$

The constant terms on each side must be equal

$$a_0(\ln r_2 - \ln r_1) = \tilde{a}_0 = \frac{1}{2\pi} \int_0^{2\pi} f \quad d\theta$$

and the terms of the expansion are orthogonal, so, for each k, the expansion coefficients must be equal.

$$\begin{aligned} (r_1^n - r_2^{2n} r_1^{-n}) a_n = \tilde{a}_n &= \frac{1}{\pi} \int_0^{2\pi} f \cos n\theta \quad d\theta \\ (r_1^n - r_2^{2n} r_1^{-n}) b_n = \tilde{b}_n &= \frac{1}{\pi} \int_0^{2\pi} f \sin n\theta \quad d\theta \end{aligned}$$

The expansion coefficients for the inner boundary condition can then be used to determine a set of expansion coefficients for the solution for the entire domain.

$$\begin{aligned} a_0 &= \frac{1}{(\ln r_2 - \ln r_1)} \frac{1}{2\pi} \int_0^{2\pi} f \quad d\theta \\ a_n &= \frac{1}{(r_1^n - r_2^{2n} r_1^{-n})} \frac{1}{\pi} \int_0^{2\pi} f \cos n\theta \quad d\theta \\ b_n &= \frac{1}{(r_1^n - r_2^{2n} r_1^{-n})} \frac{1}{\pi} \int_0^{2\pi} f \sin n\theta \quad d\theta \end{aligned}$$

The electric potential inside the domain can thus be expressed by a series expansion. A few of the terms in the expansion have been plotted in figure 3.3.

It is possible to use the weak solution from (2.10) to construct the sensitivity matrix from the expression for the electric potential. First we will find an expression for the

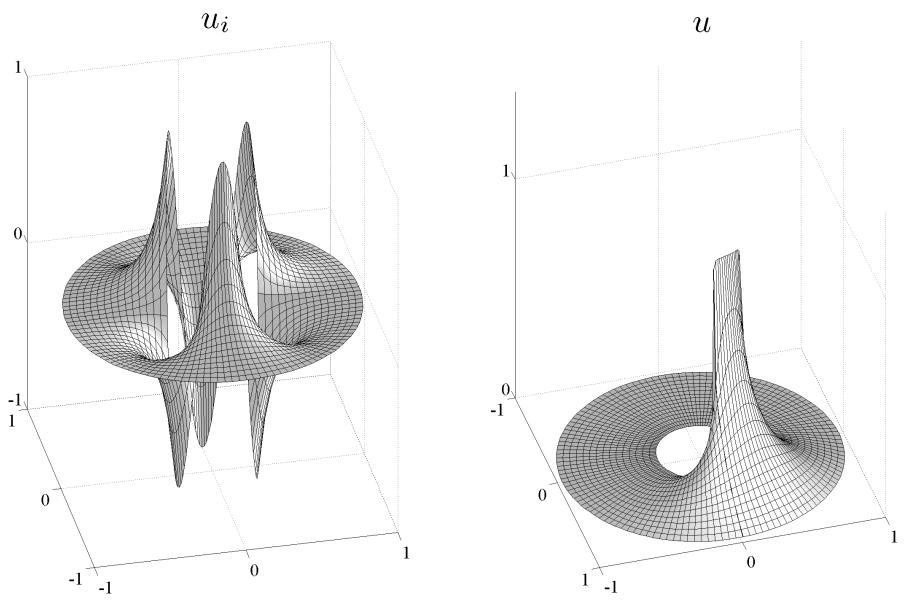

Figure 3.3: A term of the series expansion for the electric potential. The boundary conditions are clearly satisfied; the solution is periodic in the θ direction and vanishes at the outer boundary. The final boundary condition is only satisfied by the weighted sum of all the terms. It is clear though, that the term describes a harmonic function along the inner boundary and that the potential at the inner boundary can then be constructed as a trigonometric expansion.

electric field; the gradient of the potential:

$$\nabla u = \begin{bmatrix} \frac{\partial}{\partial r} \\ \frac{1}{r}\frac{\partial}{\partial \theta} \end{bmatrix} u = \begin{bmatrix} a_0 \frac{\ln \frac{r_1}{r_2}}{r} + \sum_{n=1}^{N} n r^{-1} r_-^n + (a_n \cos n\theta + b_n \sin n\theta) \\ \sum_{n=1}^{N} n r^{-1} r_-^n (-a_n \sin n\theta + b_n \cos n\theta) \end{bmatrix}$$

$$= \frac{1}{r} \begin{bmatrix} a_0 \ln \frac{r_1}{r_2} + \sum_{n=1}^{N} n r_-^n (a_n \cos n\theta + b_n \sin n\theta) \\ \sum_{n=1}^{N} n r_-^n (a_n \cos(n\theta + \frac{\pi}{2}) + b_n \sin(n\theta + \frac{\pi}{2})) \end{bmatrix}$$

In the expression above, the potential has a value of 1 on the inner boundary between $\theta = 0$ and $\theta = \frac{2\pi}{N_e}$, since electrode 1 is the active electrode. The boundary condition for the potential from electrode i is

$$f_i = \begin{cases} 1, & \frac{2\pi}{N}(i-1) \leq \theta < \frac{2\pi}{N} i \\ 0, & \text{otherwise} \end{cases}, \quad \theta \in [0, 2\pi[$$

where N is the total number of electrodes. The boundary conditions for the N different solutions are thus just rotated versions of the same basic function. To avoid calculating the expansion coefficients N times, it is easier to also rotate the base functions of the expansion. Rotating the base functions by the same angle as the boundary condition ensures that the expansion coefficients do not change.

The field from the i'th potential is then:

$$\nabla u_i = \frac{1}{r}\begin{bmatrix} a_0 \ln\frac{r_1}{r_2} + \sum_{n=1}^{N} n r_-^n (a_n \cos(n\theta + \frac{2\pi}{N}i) + b_n \sin(n\theta + \frac{2\pi}{N}i)) \\ \sum_{n=1}^{N} n r_-^n (a_n \cos(n\theta + \frac{\pi}{2} + \frac{2\pi}{N}i) + b_n \sin(n\theta + \frac{\pi}{2} + \frac{2\pi}{N}i)) \end{bmatrix}$$

Using the result from (2.10) the sensitivity matrix between electrodes i and j is

$$\begin{aligned} S_{ij}(l,m) &= \nabla u_i(l,m) \cdot \nabla u_j(l,m) da \\ &= \nabla u_i(l,m) \cdot \nabla u_i\left(l, m - (i-j)\frac{M}{N}\right) r_l \frac{2\pi}{M}\frac{r_2 - r_1}{L-1} \end{aligned} \tag{3.1}$$

where (l,m) is the discretization of the reconstruction domain with L pixels in the radial direction and M pixels in the tangential direction.

Equation (3.1) is efficient for numerical computations since it is only necessary to calculate the electric field of a single electrode to obtain all $\frac{N}{2}(N-1)$ sensitivity matrices. The sensitivity matrices for the inside out geometry are presented in figure 3.4. The expression derived here, for the sensitivity matrices, are useful for investigating the effect of changing the radii of the inner and outer boundaries and makes it easy to calculate a sensitivity matrix with an arbitrary resolution. We have even confirmed that it is possible to create relatively successful tomograms with the sensitivity matrices based on the series solution. The boundary conditions of the model do not correspond to those of the real sensor though, so they should not be used in the actual reconstruction.

Conventional Geometry

A series expansion for the conventional geometry can also be derived. The derivation is very similar to the one for the inside out geometry, so it will be omitted here. The difference between the two solutions is the base functions in the radial direction. The conventional geometry has no inner boundary and thus no boundary condition at the inner boundary. In a polar representation, the virtual boundary condition that the solutions must be finite at $r = 0$ can be applied though.

The field inside a sensor with conventional geometry and the boundary condition ap-

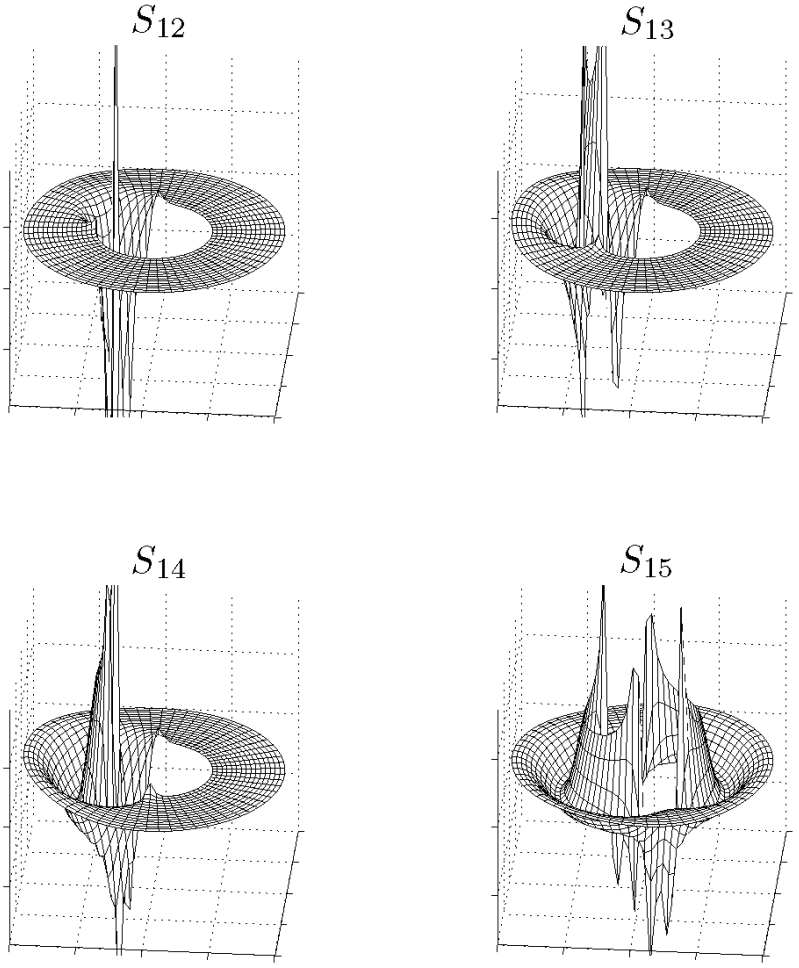

Figure 3.4: The figure presents the sensitivity matrices produced by the series expansion. In this case, with 8 electrodes, there are four basic types of sensitivity matrices. Each of the 28 sensitivity matrices used in the reconstruction can be produced by rotating one of the four basic types.

plied for electrode i is

$$\nabla u_i = \begin{bmatrix} \sum_{n=1}^{N} r^n (a_n \cos(n\theta + \frac{2\pi}{N_e} i) + b_n \sin(n\theta + \frac{2\pi}{N_e} i)) \\ \sum_{n=1}^{N} r^n (a_n \cos(n\theta + \frac{\pi}{2} + \frac{2\pi}{N_e} i) + b_n \sin(n\theta + \frac{\pi}{2} + \frac{2\pi}{N_e} i)) \end{bmatrix}$$

where the expansion coefficients are given by

$$a_n = \frac{1 - \cos\frac{Nn}{2}}{n}$$
$$b_n = \frac{\sin\frac{Nn}{2}}{n}$$

The series expansions for both geometries are well suited for a quick investigations of simple geometry changes. Since they are much simpler to calculate than using e.g. a finite difference scheme they are also a convenient instrument for investigation of reconstruction techniques where the focus is the reconstruction algorithm and not, initially, the exact sensitivity matrix.

3.2 Finite element solution with COMSOL

The sensitivity matrix is a central part of capacitance tomography, so the calculation of S was investigated from several perspectives. To be able to construct a sensitivity matrix that can better incorporate the real boundary conditions, a finite elements approach was used.

COMSOL[36] was scripted from MATLAB to produce accurate simulations of the electric field inside the inside-out sensor. The reason a finite element method was used was mainly to be able to easily obtain the solutions on a non-regular mesh, but using COMSOL also made it easy to include all the design details of the sensor and thus get even more accurate simulations of the electric field.

Figure 3.5 shows a detail that was included in the FEM model of the sensor. The electrodes are mounted on the outside of a tube. The material of the tube has a permittivity value that differs from the permittivity between the tube and the screens. The tube is indicated by the red patch on the figure. The mesh shown on the figure is the basic mesh. Prior to the simulation of the potential, the mesh was refined further than what is shown on the figure. The rougher mesh is better for visualization though.

The potential calculated by COMSOL is plotted in figure 3.6. As with the other two methods, the potential is the basis for a calculation of the electric field and then the sensitivity matrix. The electric field can be calculated directly in COMSOL and the results where then imported in MATLAB where the sensitivity matrix was calculated on the basis of (2.10).

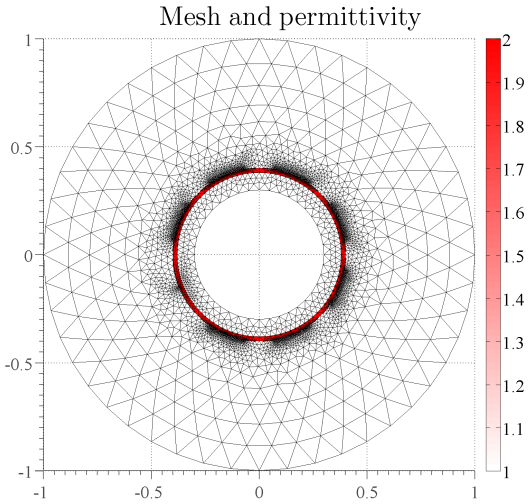

Figure 3.5: The figure shows a plot from COMSOL. The permittivity inside the model of the sensor has a relative value of 1 in most of the solution domain. The annulus (tube) just inside of the electrodes has a different permittivity. In this plot, the permittivity is set to one, but the specific value depends of the material of the tube. Plastic, PEEK and ceramics are the three types of tube that has been used for the sensors in this project.

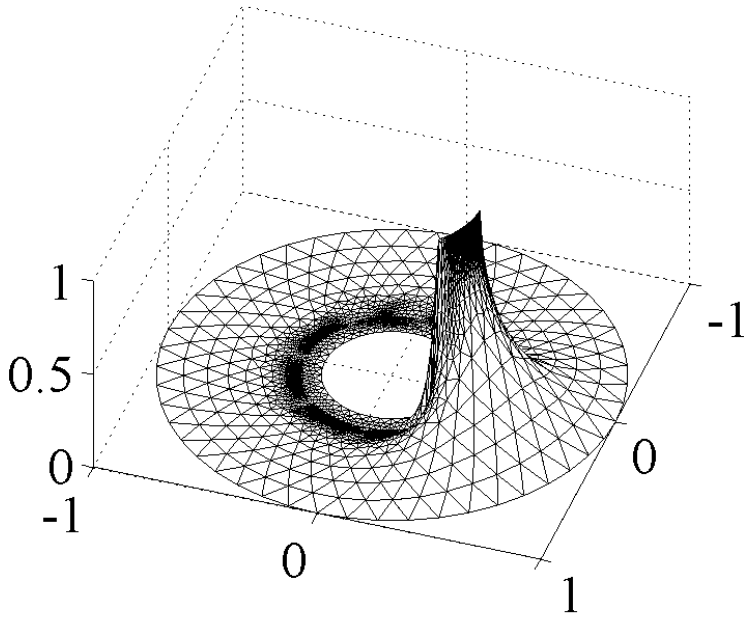

Figure 3.6: The potential inside the sensor is the basis for a calculation of the sensitivity matrix. The potential field in the plot was calculated with COMSOL which uses a finite elements approach. The solution was calculated on a finer grid than the one used for the plot.

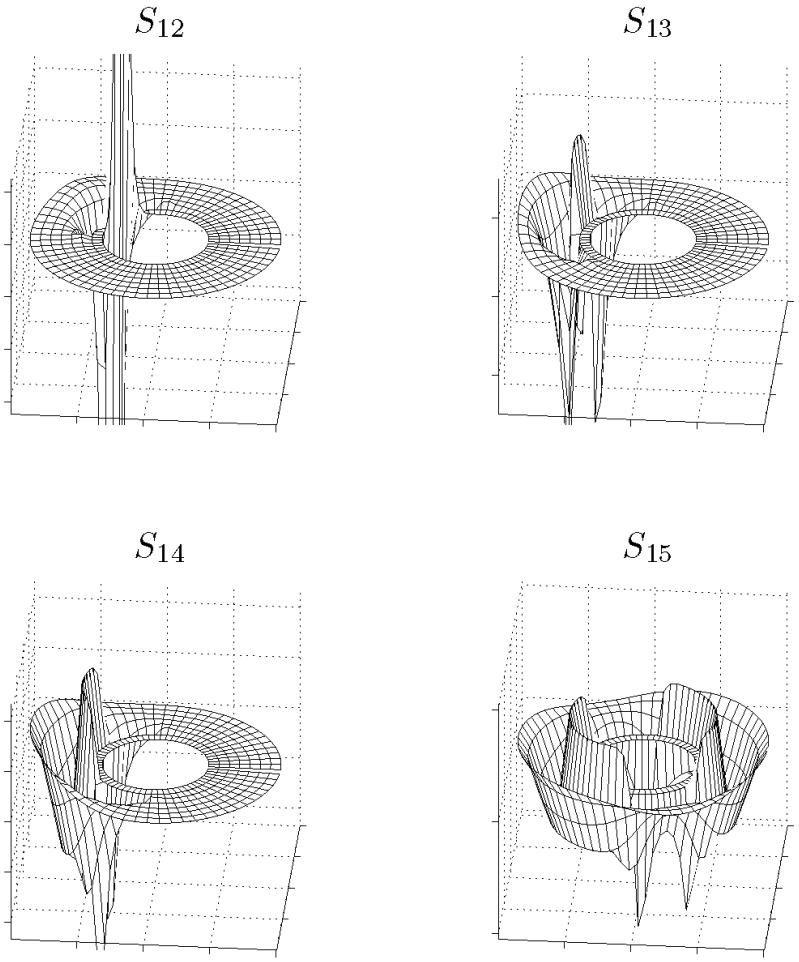

Figure 3.7: The figure shows the four basic kinds of sensitivity matrices. The sensitivity matrices have been calculated in COMSOL which uses a finite elements approach on a mesh which was also generated by COMSOL. The plotted values for the four surfaces are sampled on a regular polar grid, like the finite difference solution. The values where 'transfered' from the mesh to the grid using COMSOL's built-in postinterp function.

3.3 Discussion of the Sensitivity of the Inside Out Sensor

Since the two methods, presented here, vary both in the numerical approach and in the model on which the calculations are based, the resulting sensitivity matrices are slightly different. An inspection of figures 3.4 and 3.7 will confirm this, but also show that the qualitative shape of the matrices are very similar.

It is worth noting that, independent of the calculation method, the sum of the sensitivity-images vanishes at a characteristic radius. It will be shown later that, combined with

the normalization technique usually used for linear back-projection, this causes some problems during reconstruction.

The average value of the sum of the sensitivity matrices at each radius will be called S_r.

$$S_r = \frac{1}{2\pi} \oint_0^{2\pi} \sum_i S_i d\theta \tag{3.2}$$

A conventional geometry results in a positive definite S_r, but this is not the case for the inside out geometry. This results in some obvious problems with the normalization since it results in division by zero at a characteristic radius in the image.

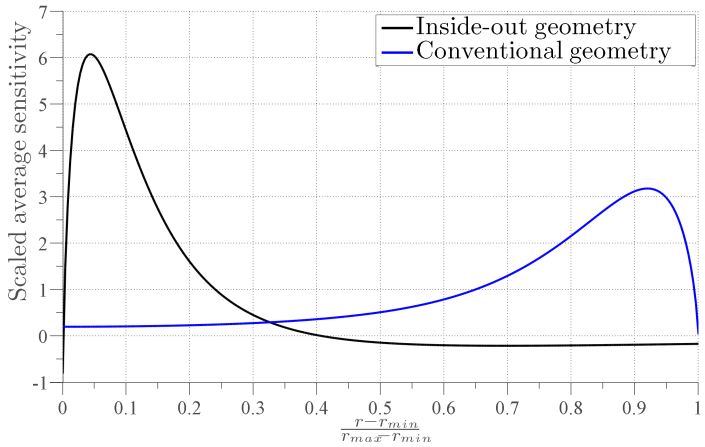

Figure 3.8: ...

The effects of the normalization of sensitivity matrices for inside-out reconstruction will be discussed in detail in section 4.1.

Chapter 4

Tomograms: the inverse problem

Calculation of a sensitivity matrix for the sensor was the subject of chapter 3. The sensitivity matrix is the Jacobian for the forward problem; calculating capacitance values for a given distribution of the permittivity. This chapter will investigate the inverse problem; how to produce a tomogram from capacitance data, based on the sensitivity matrix. The nature of this problem is within the field of discrete inverse problems.

Other types of discrete inverse problems include almost any kind of tomography, ultrasonic imaging and image de-blurring. Discrete inverse problems are typically ill-posed and ill-conditioned and this is also the case for ECT reconstruction[37].

As shown in chapter 2, the sensitivity matrix is a discretized version of a set of continuous integral equations. A set of capacitances is measured and each capacitance is related to the permittivity distribution through a Fredholm equation for the electric potentials of the involved electrodes. As an example, the capacitance between electrodes 1 and 2 can be calculated by (2.9) as:

$$\delta c_{12} = \frac{1}{V} \int \delta\varepsilon \nabla u_1 \cdot \nabla u_2 \quad da$$

where $\delta\varepsilon$ is the change in permittivity and the kernel of the Fredholm equation, $\nabla u_1 \cdot \nabla u_2$, is the inner product of the electric fields of electrodes 1 and 2 when a potential of V is applied to either of them. The equation has not yet been discretized, so u_i and $\delta\varepsilon$ are continuous functions on the reconstruction domain. To treat the inverse problem numerically, the Fredholm equations (one equation for each electrode pair) are discretized and combined into the expression in (4.1).

The tomogram is the vector, $\boldsymbol{g}$, that satisfies the linear relationship from (2.14):

$$\tilde{\boldsymbol{c}} = S\boldsymbol{g},$$

where $\tilde{\boldsymbol{c}}$ and $\boldsymbol{g}$ are the normalized capacitance vector and the gray-level vector defined

in (2.13) and $\boldsymbol{S}$ is the sensitivity matrix.

The values in $\boldsymbol{g}$ are coefficients for the base functions on which the tomogram is represented. The 'g' stands for gray-level since the base functions are normally pixels and the values then correspond to the value of the permittivity at a certain location - the location of the pixel. The pixel basis will also be adopted here.

If the number of base functions for $\boldsymbol{g}$ is M and the number of capacitance measurements is N, then $\boldsymbol{S}$ is an M by N matrix. The number of base functions for $\boldsymbol{g}$ is usually much larger than the number of available independent capacitances, so the sensitivity matrix performs a mapping from a higher- to a lower dimensional space, which makes the sensitivity matrix far from square.

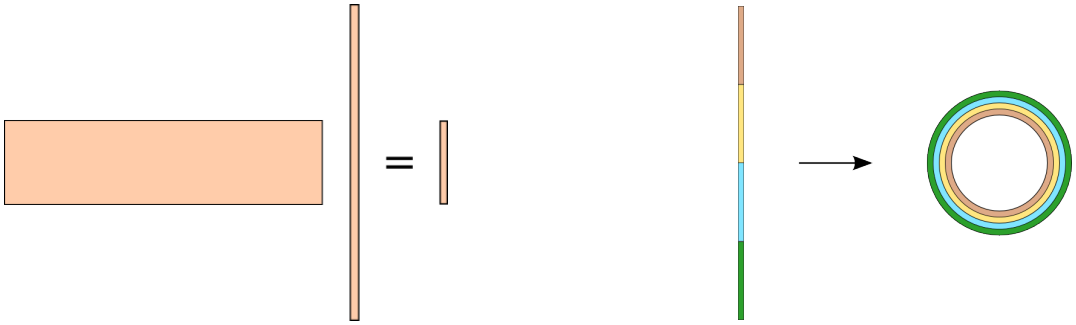

Figure 4.1: The drawing on the left illustrates the shapes of the vectors and the matrix involved in (2.14). $\boldsymbol{S}$ has a row for each electrode-pair and a column for each pixel. The drawing on the right illustrates the spatial position of the elements in the gray-level vector $\boldsymbol{g}$. If the tangential direction is divided into K elements, the first K values (symbolized by the first colored patch) of $\boldsymbol{g}$ correspond to pixels in the inner part of the reconstruction domain. The next K elements (symbolized by the second colored patch) lie in an annulus adjacent to and outside of the first set, and so forth.

The (discrete) inverse problem of calculating a tomogram from a given set of capacitances thus entails solving a heavily under-determined set of equations.

Since the sensitivity matrix is not square, it is easiest to think of a 'solution' to the inverse problem in a least squares sense. Even if an exact solution to the inverse problem existed, it would not necessarily be a desirable solution. The measurements on which the solution is founded are noisy and an exact solution (or at least a solution with an extremely small residual) will then have to include reconstructed noise, which typically leads to solutions with a very large (2-)norm. To avoid reconstruction of the noise, some form of regularization is used.

There are several established techniques available to handle such a task, but no well-established way to predict which technique is best suited for a specific inverse problem,

so a few different approaches and the results are presented here. Besides a short description, it is shown how the method was applied to this specific problem. In the case of Landweber reconstruction, a new adaption of the method is also presented. After a presentation of the reconstruction methods, a comparison of the methods, based on a small set of numerical phantoms, is presented.

4.1 Linear Back Projection

Linear back-projection (LBP) is a simple technique which is widely used for reconstruction of tomograms for ECT. Since it involves just a single matrix multiplication, LBP is a very fast reconstruction technique. The simplicity and speed are the main reasons for its wide adoption.

The principle of linear backprojection is to achieve a closed form solution to the inverse problem by constructing a pseudo-inverse for the Jacobian.

$$g = \text{pseudoinv}[S]\tilde{c}$$

Again; where $\tilde{c}$ and g are the normalized capacitance vector and the gray-level vector as defined in (2.13) and S is the sensitivity matrix.

The construction of the pseudo-inverse has been based both in theory and in trial and error approaches. A well known choice for a pseudo-inverse, the Moore-Penrose pseudo-inverse, tends to produce undesirable results. Instead, crude approximations like $S^{-1} \approx S^T$ are widely used. One of the reasons this gives acceptable results is because of various forms of normalization of the equations. In the forward problem, each capacitance is calculated as the value of the permittivity distributions projection onto the corresponding row in the sensitivity matrix (the sensitivity field for that capacitance pair). With LBP, the permittivity distribution is then formed as a weighted sum of each row of the sensitivity matrix. Each row in the Jacobian thus becomes a base vector for the reconstruction, and the capacitances are used as coefficients.

Normalization in LBP

The rows of the Jacobian are not orthogonal. Trying to reconstruct g directly as a weighted sum of the rows of S

$$g_{j,\,\text{direct}} = S^T\tilde{c} = \sum_i S_{ij}^T \tilde{c}_i$$

is thus a very crude approximation. The set of measurements which were used to normalize the permittivity and capacitances are used to provide a better approximation.

The pseudo inverse must map the capacitance vector to the correct permittivity vector for $\tilde{\boldsymbol{c}} = \tilde{\boldsymbol{c}}_{low}$ and $\tilde{\boldsymbol{c}} = \tilde{\boldsymbol{c}}_{high}$:

$$\begin{aligned} \tilde{\boldsymbol{\varepsilon}}_{low} &= \mathbf{0}_M \\ &= \boldsymbol{S}^{\dagger}_{LBP}\mathbf{0}_N \end{aligned} \qquad \begin{aligned} \tilde{\boldsymbol{\varepsilon}}_{high} &= \mathbf{1}_M \\ &= \boldsymbol{S}^{\dagger}_{LBP}\mathbf{1}_N \\ &= \sum_i \boldsymbol{S}^{\dagger}_{ij,LBP} \end{aligned}$$

where $\mathbf{0}_K$ (or $\mathbf{1}_K$) is a vector with K elements which are all equal to zero (or one). The equation to the left is trivial, but the equation on the right states a condition for the pseudo-inverse we are looking for to fulfill. Generally a pseudoinverse can be constructed as

$$\boldsymbol{S}^{\dagger} = (\boldsymbol{A}_1 \boldsymbol{S} \boldsymbol{A}_2)^T$$

where the matrices A_i are not yet specified. Two simple suggestions for the pseudoinverse would then be to either left- or right-multiply with a diagonal matrix.

$$\begin{aligned} \boldsymbol{S}^{\dagger}_r &= (\boldsymbol{D}_r^{-1}\boldsymbol{S})^T \\ \boldsymbol{S}^{\dagger}_c &= (\boldsymbol{S}\boldsymbol{D}_c^{-1})^T \end{aligned}$$

where the elements of the diagonal matrices are utilized for normalization of either the rows or columns of the pseudo-inverse.

$$[\boldsymbol{D}_r]_{ij} = \begin{cases} 0 & i \neq j \\ \sum_{i'} S_{i'j} & i = j \end{cases}$$

$$[\boldsymbol{D}_c]_{ij} = \begin{cases} 0 & i \neq j \\ \sum_{j'} S_{ij'} & i = j \end{cases}$$

With the demand that the solution to the inverse problem, when the gray-level vector has a value of 1 everywhere, is a normalized capacitance vector with ones everywhere, these two different forms of normalization lead to the following definition of

the pseudo-inverse for $\boldsymbol{S}$

$$\boldsymbol{S}_r^\dagger \mathbf{1}_M = \begin{bmatrix} \dfrac{S_{11} + S_{21} + \dots}{\sum\limits_{i'} S_{i'1}} \\ \dfrac{S_{11} + S_{21} + \dots}{\sum\limits_{i'} S_{i'2}} \\ \vdots \end{bmatrix} = \mathbf{1}_N$$

$$\boldsymbol{S}_c^\dagger \mathbf{1}_M = \begin{bmatrix} \dfrac{S_{11}}{\sum\limits_{j'} S_{1j'}} + \dfrac{S_{21}}{\sum\limits_{j'} S_{2j'}} + \dots \\ \dfrac{S_{12}}{\sum\limits_{j'} S_{1j'}} + \dfrac{S_{22}}{\sum\limits_{j'} S_{2j'}} + \dots \\ \vdots \end{bmatrix} \neq \mathbf{1}_N$$

Row-wise normalization thus ensures that the inverse problem leads to the correct solution.

$$[\boldsymbol{S}_{\boldsymbol{LBP}}^\dagger]_{ij} = \frac{S_{ji}}{\sum\limits_j S_{ji}}$$

To put it in a less formalized form; the pseudo-inverse is formed by first normalizing each column (each pixel, in most cases) in $\boldsymbol{S}$ and then transposing it. This causes the shape of each column in the pseudo-inverse to become slightly 'warped' copies of the basis vectors on which the permittivity is projected in the forward problem.

Since the LBP tomogram, $\boldsymbol{g}$, can be calculated in a single matrix multiplication (provided that $\boldsymbol{S}_{LBP}^\dagger$ has already been constructed), it is a numerically very fast technique. The images must be considered to be of low quality, but global features of the permittivity distribution are reproduced. The normalization presented above leads to some problems with an inside-out geometry though.

At certain locations within the reconstruction domain, the sum in the denominator of the normalization factor, $\dfrac{1}{\sum\limits_j S_{ij}}$, vanishes, causing the normalization to become unbounded. This problem causes artifacts to appear in the reconstructed image at a specific radius.

It can be used for inside-out tomography, but the accompanying artifacts makes it unsuitable for anything else than qualitative representations of the real permittivity distribution.

4.2 Tikhonov

Tikhonov reconstruction is another fast method which produces tomograms via a single matrix multiplication. Tikhonov regularization provides a solution that minimizes a certain metric, defined by

$$L = ||\boldsymbol{S}\boldsymbol{g} - \boldsymbol{c}||^2 + ||\boldsymbol{\Gamma}\boldsymbol{g}||^2$$

where $||\boldsymbol{S}\boldsymbol{g} - \boldsymbol{c}||$ is the Euclidean norm of the residual of the solution $\boldsymbol{g}$. The second term is the regularization term. The operator $\boldsymbol{\Gamma}$ can be any operator. Typically that operator is chosen to be the identity matrix (multiplied by a scaling factor). In that case, the Tikhonov solution is a compromise between minimizing the residual and the norm of the solution. Other regularization choices could be to let $\boldsymbol{\Gamma}$ be the Laplacian on $\boldsymbol{g}$, which would make the Tikhonov solution become a compromise between minimizing the residual and the curvature.

By looking for a permittivity distribution which minimizes the metric, we will find a direct matrix solution. At a minimum for L, the gradient with respect to $\boldsymbol{g}$ vanishes:

$$\begin{aligned}\boldsymbol{\nabla} L &= \boldsymbol{\nabla}(\boldsymbol{g}^T\boldsymbol{S}^T\boldsymbol{S}\boldsymbol{g} + \boldsymbol{c}^T\boldsymbol{c} - 2\boldsymbol{g}^T\boldsymbol{S}^T\boldsymbol{c} + \boldsymbol{g}^T\boldsymbol{\Gamma}^T\boldsymbol{\Gamma}\boldsymbol{g}) \\ &= 2\boldsymbol{S}^T\boldsymbol{S}\boldsymbol{g} - 2\boldsymbol{S}^T\boldsymbol{c} + 2\boldsymbol{\Gamma}^T\boldsymbol{\Gamma}\boldsymbol{g}\end{aligned}$$

Solving for $\boldsymbol{\nabla} L = 0$ produces a matrix equation for the permittivity distribution

$$\begin{aligned}\boldsymbol{g} &= (\boldsymbol{S}^T\boldsymbol{S} + \boldsymbol{\Gamma}^T\boldsymbol{\Gamma})^{-1}\boldsymbol{S}^T\boldsymbol{c} \\ &= \boldsymbol{M}\boldsymbol{c}\end{aligned}$$

The matrix $\boldsymbol{M}$ needs to obey the same normalization constraints as the LBP pseudoinverse, so it is normalized in the same manner.

$$[\boldsymbol{S}^{\dagger}_{Tikh}]_{pi} = \frac{M_{pi}}{\sum_i M_{pi}}, \qquad \boldsymbol{M} = (\boldsymbol{S}^T\boldsymbol{S} + \boldsymbol{\Gamma}^T\boldsymbol{\Gamma})^{-1}\boldsymbol{S}^T$$

Equipped with the pseudo-inverse supplied by the Tikhonov regularization above, it is possible to generate a tomogram of the permittivity distribution. Simply choosing the identity matrix as a regularization function, yields results that are very similar to the LBP solution.

To adjust the weight given to the importance of minimizing the solution-norm (in the case of using the identity matrix as a regularization choice), a regularization parameter, α, is introduced.

$$\boldsymbol{M} = (\boldsymbol{S}^T\boldsymbol{S} + \alpha I)^{-1}\boldsymbol{S}^T$$

There is no 'correct' value for α, but extreme values will lead to solutions that are either over smoothed or with large oscillations caused by reconstructed noise, for very large or small alpha, respectively.

The artifacts of LBP reconstruction are also present in Tikhonov reconstruction since they are caused by the normalization.

4.3 Landweber

Landweber regularization is an iterative technique which follows a very simple algorithm to find a vector $\boldsymbol{x}$ which satisfies the forward problem $\boldsymbol{Ax} = \boldsymbol{y}$

$$\boldsymbol{x}_{[k]} = \mathcal{P}\left[\boldsymbol{x}_{[k-1]} + \omega \boldsymbol{A}^T(\boldsymbol{y} - \boldsymbol{A}\boldsymbol{x}_{[k-1]})\right]$$

where $\mathcal{P}$ is an operator which enforces some constraints/conditions onto the solution. $\mathcal{P}$ can be the identity operator (no conditions are applied), but a common choice is a non-negativity constraint (which is easy to incorporate as long as the solution is expressed in a pixel basis).

In the case of Landweber the variables in the inverse problem are not normalized. Instead, the variables are the permittivity- and capacitance change from a single reference set; $\boldsymbol{\varepsilon}_{low}$ and $\boldsymbol{c}_{low}$.

$$\boldsymbol{\Delta\varepsilon}_{[k]} = \mathcal{P}\left[\boldsymbol{\Delta\varepsilon}_{[k-1]} + \omega \boldsymbol{S}^T(\boldsymbol{\Delta c} - \boldsymbol{S}\boldsymbol{\Delta\varepsilon}_{[k-1]})\right]$$

The starting vector for the reconstruction is important. A good start guess will lead to faster convergence, but since the algorithm only promises to find some minimum, it is also possible that the best solution is never found if the initial guess is not good enough. This seems to be the case with Landweber for inside-out ECT, so it was necessary to use the LBP solution as an initial guess.

$$\boldsymbol{\Delta\varepsilon}_{[0]} = \boldsymbol{g}_{LBP}(\boldsymbol{c}_{high} - \boldsymbol{c}_{low})$$

Unfortunately, the artifact of the LBP reconstruction, is very stable under the Landweber iterations, so it is present even after the Landweber reconstruction has converged.

Smoothed Landweber

This lead to the construction of an operator, $\mathcal{P}$, which would counter the unwanted high frequency components of the LBP-artifact. With a smoothing operator, the high activity which the LBP solution concentrated in the area of the artifact is slowly moved

to adjacent pixels. The Landweber algorithm does not re-introduce the artifact after it is removed, which seems to support the act of actively removing it.

The smoothing operator is periodic in the θ-direction and bounded in the radial direction. For a discretized permittivity with $M \times N$ pixels (N pixels in the periodic direction), the operator performs the following mapping:

$$g_{i,\,\text{smooth}} = \begin{cases} \frac{1}{7}(4g_1 + g_2 + g_N + g_{N+1}) & i = 1 \\ \frac{1}{7}(g_{i-1} + 4g_i + g_{i+1} + g_{i+N}) & 1 < i < N \\ \frac{1}{7}(g_1 + g_{N-1} + 4g_N + g_{2N}) & i = N \\ \frac{1}{8}(g_{i-N} + g_{i-N+1} + g_{i-1} + 4g_i + g_{i+N}) & N < i \leq M - N + 1 \wedge \mod_N i = 0 \\ \frac{1}{8}(g_{i-N} + 4g_i + g_{i+1} + g_{i+N-1} + g_{i+N}) & N < i \leq M - N + 1 \wedge \mod_N i = 1 \\ \frac{1}{7}(g_{M-2N+1} + 4g_{M-N+1} + g_{M-2N+2} + g_M) & i = M - N + 1 \\ \frac{1}{7}(g_{i-N} + g_{i-1} + 4g_i + g_{i+1}) & M - N + 1 < i < M \\ \frac{1}{7}(g_{M-N} + g_{M-N+1} + g_{M-1} + 4g_M) & i = M \\ \frac{1}{8}(g_{i-N} + g_{i-1} + 4g_i + g_{i+1} + g_{i+N}) & \text{otherwise} \end{cases}$$

To avoid the smoothing operator dominating the Landweber iteration, it is applied during only a sub-set of the iterations. With active smoothing for 10% of the iterations, the smoothed Landweber algorithm is:

$\boldsymbol{\Delta\varepsilon}_{[0]} = \boldsymbol{g}_{LBP}(c_{high} - c_{low})$
for $k = 1$ to K
  $\boldsymbol{\Delta\varepsilon}_{[k]} = \boldsymbol{\Delta\varepsilon}_{[k-1]} + \omega \boldsymbol{S}^T(\boldsymbol{\Delta c} - \boldsymbol{S}\boldsymbol{\Delta\varepsilon}_{[k-1]})$
  if $\mod(k, L) = \frac{9}{10}L$
    $\boldsymbol{\Delta\varepsilon}_{[0]} = \Phi\boldsymbol{\Delta\varepsilon}_{[0]}$
  end
end

A comparison of traditional and smoothed Landweber regularization is shown in figure 4.2. Smoothed Landweber removes the ring-shaped artifact, from the LBP tomogram, very well and the quality of the image is better than with regular Landweber and much better than the direct methods.

4.4 Conjugate gradients

The conjugate gradients approach is a projection method. A solution to the inverse problem is constructed on a subspace which is spanned by a special set of vectors. The

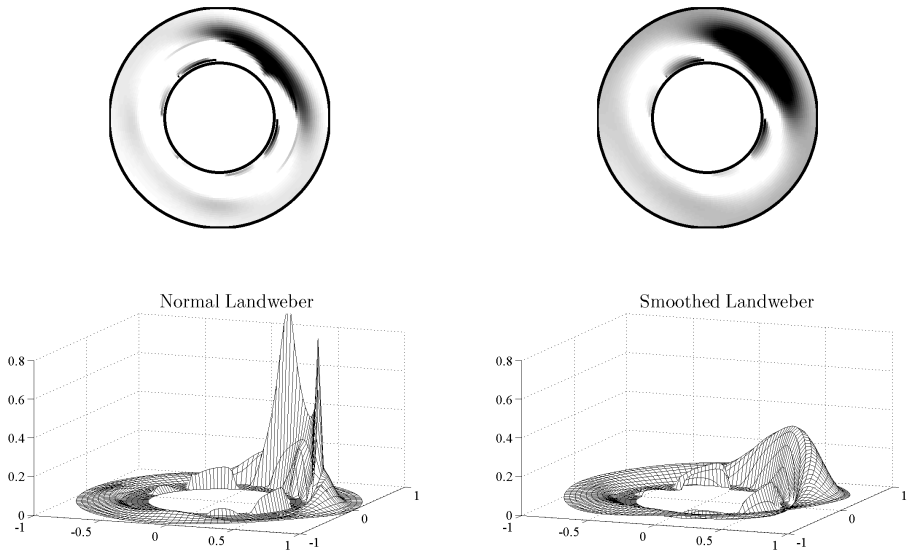

Figure 4.2: The figure shows a surface plot of the result of Landweber reconstruction. The original permittivity distribution is shown in figure 4.4. The artifact from the LBP tomogram is clearly visible as a sharp ridge in the Landweber tomogram. The smoothed Landweber algorithm clearly removes the artifact thus improves the resulting tomogram.

space is called the Krylov subspace and is defined as

$$\mathcal{K}_k = \text{span}\left((\boldsymbol{S}^T\boldsymbol{S})^0\boldsymbol{S}^T\Delta\boldsymbol{c}, \quad (\boldsymbol{S}^T\boldsymbol{S})^1\boldsymbol{S}^T\Delta\boldsymbol{c}, \quad (\boldsymbol{S}^T\boldsymbol{S})^2\boldsymbol{S}^T\Delta\boldsymbol{c}, \ldots, \quad (\boldsymbol{S}^T\boldsymbol{S})^{k-1}\boldsymbol{S}^T\Delta\boldsymbol{c}\right) \quad (4.1)$$

where $\Delta\boldsymbol{c} = \boldsymbol{c} - \Delta\boldsymbol{c}_{low}$ is the capacitance change. The Krylov subspace is thus defined by the inverse problem, so for two different capacitance vectors, the reconstruction will be performed in two different subspaces. It turns out that the Krylov subspace is very well suited as a basis for the reconstruction and that it has regularizing properties.

The basis for the reconstruction is obtained by ortho-normalizing the set of vectors used to span the subspace. The first basis vector is

$$\boldsymbol{w}_1 = \boldsymbol{S}^T\Delta\boldsymbol{c}$$

and the rest of the basis is constructed by Gram-Schmidt ortho-normalization with the rest of the vectors ($(\boldsymbol{S}^T\boldsymbol{S})^i\boldsymbol{S}^T\Delta\boldsymbol{c}$).

The span of the first k vectors in the Krylov subspace is similar to the span of the k first vectors in the singular value decomposition for the problem. The conjugate gradients solution then turns out to be similar to a filtered SVD solution, but the great advantage of CGLS is that the entire SVD solution does not need to be calculated. The subspace is constructed iteratively, one basis-vector at a time. This has great advantages for

large scale problems, so to preserve that advantage it is necessary to use Gram-Schmidt orthonormalization instead of e.g. a Householder transformation.

For ECT, the algorithm for CGLS becomes

$\boldsymbol{g}_0 = \boldsymbol{0}$
$\Delta\boldsymbol{c} = \boldsymbol{c} - \boldsymbol{c}_{low}$
$\boldsymbol{r}_0 = \Delta\boldsymbol{c} - \boldsymbol{S}\boldsymbol{g}_0$
$\boldsymbol{d}_0 = \boldsymbol{S}^T\boldsymbol{r}_0$
for $k = 1$ to K
$\quad \alpha_k = \dfrac{\|\boldsymbol{S}^T\boldsymbol{r}_{k-1}\|_2^2}{\|\boldsymbol{S}\boldsymbol{d}_{k-1}\|_2^2}$
$\quad \boldsymbol{g}_k = \boldsymbol{g}_{k-1} + \alpha_k\boldsymbol{d}_{k-1}$
$\quad \boldsymbol{r}_k = \boldsymbol{r}_{k-1} - \alpha_k\boldsymbol{S}\boldsymbol{d}_{k-1}$
$\quad \beta_k = \dfrac{\|\boldsymbol{S}^T\boldsymbol{r}_k\|_2^2}{\|\boldsymbol{S}^T\boldsymbol{r}_{k-1}\|_2^2}$
$\quad \boldsymbol{d}_k = \boldsymbol{S}^T\boldsymbol{r}_k + \beta_k\boldsymbol{d}_{k-1}$
end

The conjugate gradients algorithm is very fast for an iterative technique, since the result converges[1] after very few (typically 5-6) iterations.

Since the conjugate gradients solution is initialized at origo, it does not have problems with the artifact which was produced with the LBP solution.

4.5 Test on numerical phantoms

A set of numerical phantoms, $\boldsymbol{\varepsilon}_i^c$ (where 'c' denotes that this is numerically 'computed' values), were created to test the reconstruction methods. Each of the three test distributions tested a property of the reconstruction. One distribution was the layered type of flow which is very typical for low Reynolds numbers. Another distributions have some small areas with sharp edges, which test the effective resolution of the reconstruction methods. The third distribution is ring-shaped, with the high permittivity placed close to the electrodes. This was to test whether the low-permittivity area behind the ring could be reproduced.

Each test-distribution, $\boldsymbol{\varepsilon}_i^c$, was used as input to the forward problem, producing a capacitance-change vector, $\Delta\boldsymbol{c}_i^c$, to use as input for the reconstruction methods. As previously described, each reconstruction method uses a specific normalization method,

[1]The conjugate gradients approach exhibits semi-convergence, which means that the result will converge toward a 'good' solution for a while and then diverge in another direction.

based on a set of calibration measurements. The calibration sets were also produced numerically.

The permittivity distributions, both the calibration- and test-distributions, were created as distributions of ones and zeros. This means that the permittivity distribution and the gray-level vectors are the same.

$$\begin{aligned} \boldsymbol{g}^c_{low} &= \boldsymbol{\varepsilon}^c_{low} & \qquad \boldsymbol{g}^c_{high} &= \boldsymbol{\varepsilon}^c_{high} \\ &= \mathbf{0} & &= \mathbf{1} \end{aligned}$$

Capacitance vectors were then produced

$$\Delta \boldsymbol{c}^c_{low} = \boldsymbol{S}\boldsymbol{\varepsilon}^c_{low} = \mathbf{0} \qquad \Delta \boldsymbol{c}^c_{high} = \boldsymbol{S}\boldsymbol{\varepsilon}^c_{high}$$

and used to obtain the normalized capacitance vectors;

$$\tilde{\boldsymbol{c}}^c_{ij} = \frac{\boldsymbol{S}\boldsymbol{\varepsilon}^c_{\boldsymbol{i}}}{\boldsymbol{c}^c_{j,high}},$$

where $\tilde{\boldsymbol{c}}^c_{ij}$ means the j'th normalized capacitance for the i'th test distribution and $\tilde{\boldsymbol{c}}^c_{j,high}$ means the j'th high-calibration capacitance.

Since using the model to produce the capacitances is only an approximation, the results only provide a rough estimate of the quality of the reconstruction methods. A better test is to use real data, but with real data it is much more difficult to create arbitrary phantom-distributions.

The results are displayed in figure 4.4. The numerical results indicate that, of the direct methods, linear back-projection is the best choice. For the slower methods it seems that smoothed Landweber and CGLS are the best suited. CGLS is much faster than smoothed Landweber which would make it the most likely candidate for any real-time applications.

Figure 4.3 shows the relative speed of some of the methods. It might seem surprising that using a smoothing filter in Landweber does not make it slower, but the smoothing filter is only applied a small percentage of the time and involves just a single matrix multiplication, so the cost is negligible.

It is no surprise that linear backprojection is the fastest method. The conjugate gradients method is an order of magnitude slower than LBP, but it seems likely that it would be possible to use CGL for live imaging which involves producing around 10 frames per second.

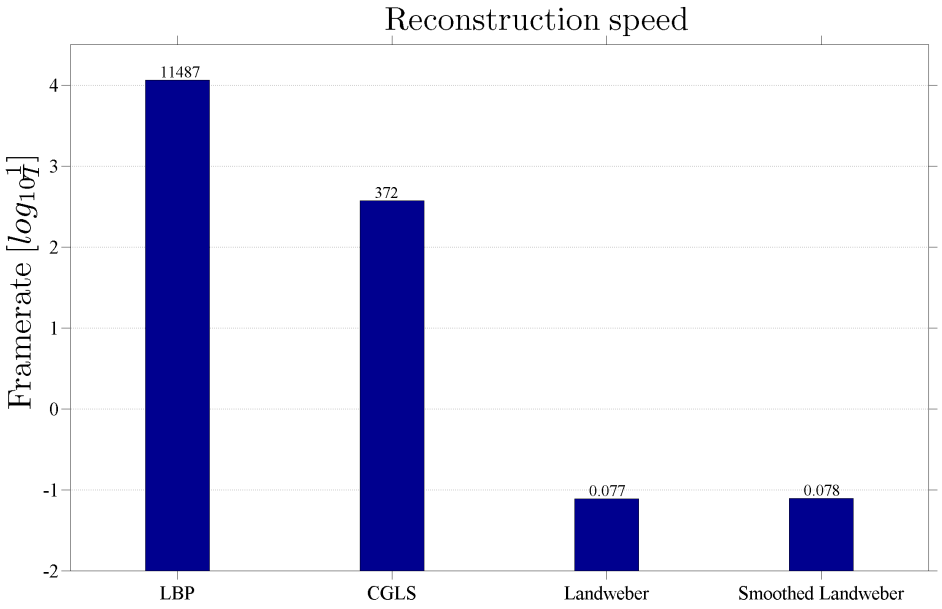

Figure 4.3: The bar plot shows the relative speeds of four reconstruction methods. Linear backprojection (LBP) involves a single matrix multiplication which is very fast. The conjugate gradients approach (CGLS) needs just a few iterations to produce a tomogram. Even though each CGLS iteration performs more matrix multiplications than Landweber, it produces a tomogram in much less time since Landweber needs to run many more iteration. The reconstruction was performed in MATLAB on a desktop PC.

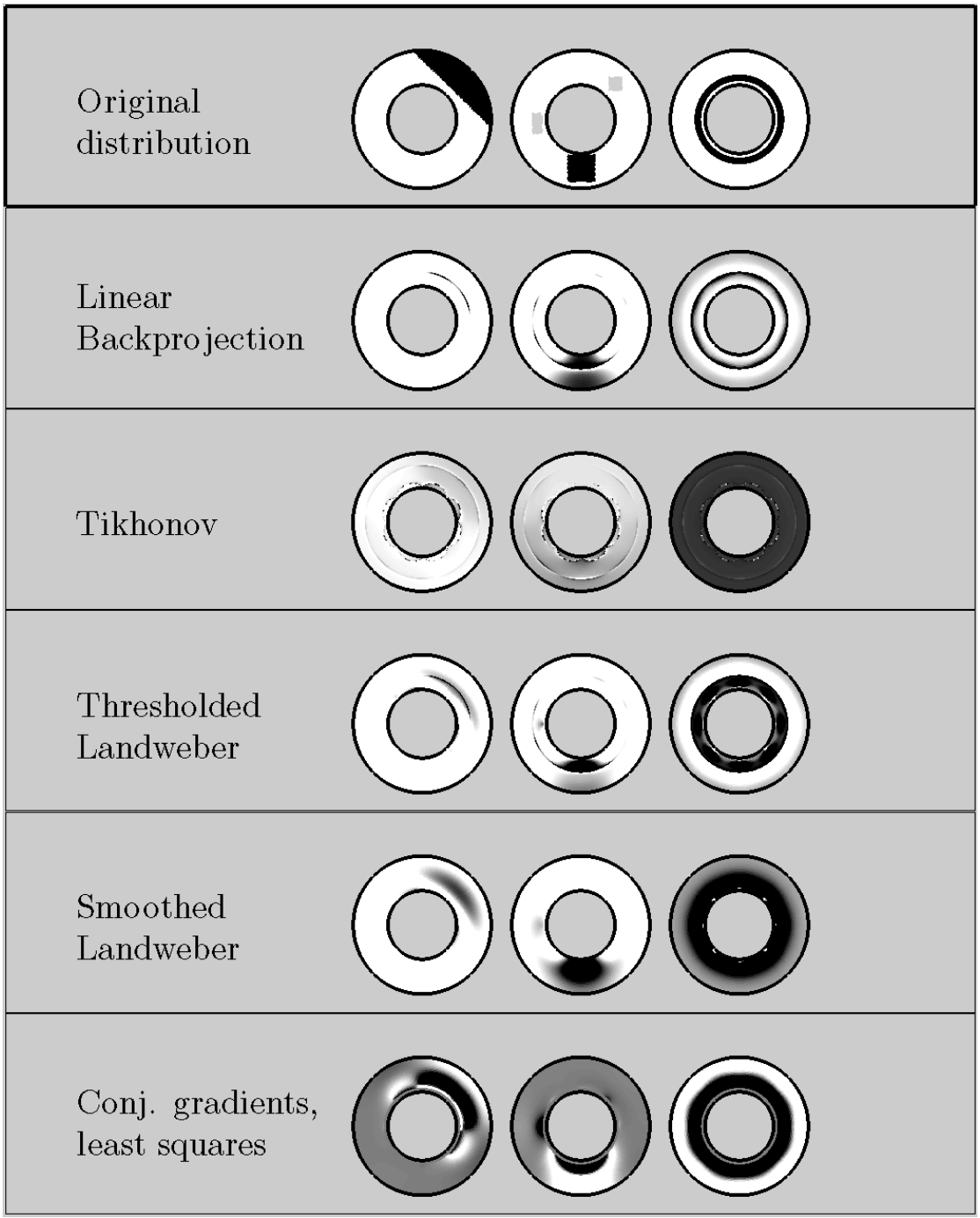

Figure 4.4: The figure shows the results of reconstruction based on the numerical phantoms with each of the five methods. The iterative methods (Landweber and conjugate gradients) show the best results, but linear backprojection is very close to the thresholded Landweber result. Linear backprojection is much faster than the iterative methods since it involves just a single matrix multiplication. It is clear why it is such a popular reconstruction method for ECT, even if it is possible to achieve more accurate tomograms with more advanced methods.

4.6 Effective spatial resolution

A question which is often asked by the interpreter of the tomogram is; what is the resolution? Such a question is in some respects meaningless since the resolution (in a traditional sense) of the tomogram is arbitrary. The number of base functions (pixels) for the permittivity can be set to any number, within reason.

The pixel-resolution of the tomogram is thus not the most vital parameter. Another, more meaningful, way to define the resolution is to ask how large a part of the reconstruction domain needs to be filled with high permittivity material, for the resulting capacitance change to be measurable. The change in capacitance is defined by (2.14) and corresponds to

$$\tilde{c}_i = \sum_k g_k S_{ik} \tag{4.2}$$

Now, let the permittivity change that caused the capacitance, $\tilde{c}_i$, have a non-zero value only on a disk-shaped sub-domain of the reconstruction domain, Ω. The set of all such disk-shaped changes will be called Ω_D:

$$\Omega_D = \{w_i \in B_2 : w_i \subset \Omega\}, \tag{4.3}$$

where B_2 is the set off all disks (2-balls). The disks, w_i, have a a center $\boldsymbol{x}_i$ and area A_i.

The permittivity change is then

$$g_k = \begin{cases} 1 & \boldsymbol{x_k} \in \omega_i \\ 0 & \text{otherwise} \end{cases}, \tag{4.4}$$

where $\boldsymbol{x_k}$ is the position of the k'th pixel. The capacitance change then reduces to a sum over the indexes k that correspond to a pixel inside ω_i:

$$\tilde{c}_i = \sum_{k:\boldsymbol{x_k} \in \omega} g_k S_{ik}. \tag{4.5}$$

For the change, $\tilde{c}_i$, to be measurable, at least one of the i measured capacitances needs to change by an amount larger than the capacitance resolution of the charge-transfer circuits, ρ_c.

$$\rho_c \leq \left| \sum_{k:\boldsymbol{x_k} \in \omega_i} g_k S_{ik} \right| \tag{4.6}$$

The resolution depends on the position of ω_i; if it is located close to the electrodes, where the sensitivity is generally higher, the necessary size of ω_i is smaller than if the location is farther away from the electrodes.

The spatial resolution could be defined as the area of ω_i that ensures a measurable change, regardless of the position. This corresponds to finding the sub-set of Ω_D which contains disks that cause a change of exactly the same magnitude as the capacitance resolution and then finding the area of the largest of the disks in that sub-set.

$$\rho_A = \sup\{A_i | \omega_i \in \Omega_D \wedge \rho_c = \left| \sum_{k:\boldsymbol{x_k} \in \omega} g_k S_{ik} \right| \} \tag{4.7}$$

This expression could potentially be difficult to evaluate, but since we are looking for a minimum it is reasonable to expect that ω_i will be placed in the areas with small sensitivity. Fortunately, the variations in S in these areas are slow, so ρ_A can be approximated by investigation of a histogram of S.

As was done for the pseudo-inverse, the elements of the sensitivity matrix will now be normalized

$$[\tilde{\boldsymbol{S}}]_{ij} = \alpha_i [\boldsymbol{S}]_{ij} \tag{4.8}$$

such that

$$\Delta \boldsymbol{c}_i^b = \tilde{\boldsymbol{S}}_{ij} \boldsymbol{\varepsilon}_j \tag{4.9}$$

where $\Delta \boldsymbol{c}_i^b$ is the value of the bit-wise capacitance change (compared to the low-calibration bit-value) for electrode-pair i. Using the bit-values is convenient because it makes it easy to estimate the resolution directly from raw-data files.

The histogram in figure 4.5 shows that a large part of the reconstruction domain has the same low value for $\tilde{\mathbf{S}}_{ij}$.

The effective resolution of the tomogram ρ_A, will then be estimated from the typical amplitude of $\tilde{\mathbf{S}}_{ij}$. The noise on the capacitance measurement circuits which were employed spreads over approximately 5 bits, so (4.9) reduces to

$$5 = \sum_j a_j 10 \Delta \varepsilon_j \tag{4.10}$$

$$= 10 \sum_j a_j \Delta \varepsilon_j \tag{4.11}$$

$$= 10 \Delta \varepsilon \rho_A \tag{4.12}$$

where a_j is the area of the j'th pixel, $\Delta\varepsilon$ is the permittivity change between the two calibration distributions and ρ_A is the area, relative to the total area. The effective resolution of the inside-out sensor is then

$$A_{res} = \frac{5}{10 \Delta \varepsilon} \approx 1\% \tag{4.13}$$

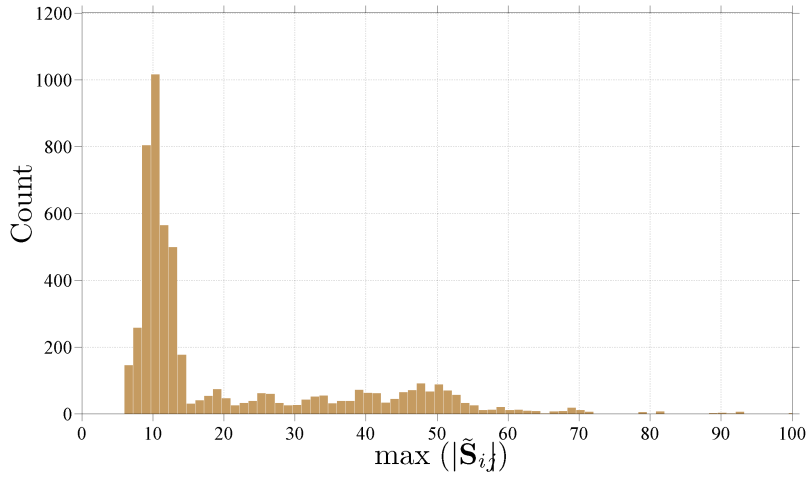

Figure 4.5: The plot shows that the reconstruction domain contains mostly pixels with a maximum sensitivity of approximately $\frac{10bit}{A}$, where A is the area of the entire domain.

The meaning of 'resolution' is now based on detectable changes in capacitance measurements. A detectable change in capacitance will not necessarily produce a noticeable change in the tomogram since the tomogram depends on the exact shape of the sensitivity matrix in the associated area and on the choice of reconstruction method. A more fitting term might be the effective spatial sensitivity, since the capacitance change is measurable, but not necessarily reproduced in the tomogram.

The exact value for the effective spatial resolution of 1% of the total area is a very rough estimate, but the derived expression is valuable since it shows how the effective spatial resolution depends on many factors. A high resolution leads to higher spatial resolution, but the medium also affects it, i.e. a sensor in oil/air will have a lower effective spatial resolution than a sensor in water/air. The geometry also affects the effective spatial resolution since a higher maximum sensitivity in each area of the annulus will lead to an easier measurable response to the perturbation.

Chapter 5

Measuring Capacitance by Charge Transfer

Image reconstruction for ECT is difficult and also very interesting, from a mathematical viewpoint, but the seemingly mundane task of obtaining the capacitance data is also challenging. For any practical ECT-sensor geometries, i.e. electrode lengths and diameters in the cm-size, the order of magnitude of the capacitances and capacitance-changes are in the sub-pF range.

Several capacitance measuring methods are employed for ECT. Some of them were discussed briefly in section 2.1. The AC-based and the charge-transfer technique were both considered for this project. The AC-based technique is superior to the CT method in many aspects, the resolution is 1-2 orders of magnitude higher, but it is also more complex. The simplicity of the CT method is important from a circuit/sensor-design perspective, since the size of the electronics is an important parameter for the inside-out geometry.

The charge transfer (CT) technique [3, 19, 38] is simple to implement in hardware and can be used to measure capacitance changes in the fF range. The fundamental concept of CT is to apply a square wave to one side of a capacitor and to keep the other side at a constant potential. The measurement side of the circuit is kept at a constant potential by an operational amplifier (op-amp). The output of the op-amp is an indication of the size of the unknown capacitance. Figure 5.1 shows a schematic of the measuring side of a CT circuit. The only modification, to a standard setup is that the '+'-input node of the op-amp is connected to a 2.5V potential instead of ground. The CT circuit works in the same way, but the power supply for the circuit is more simple, since the same potentials can be used to create the square wave signal and power the op-amp.

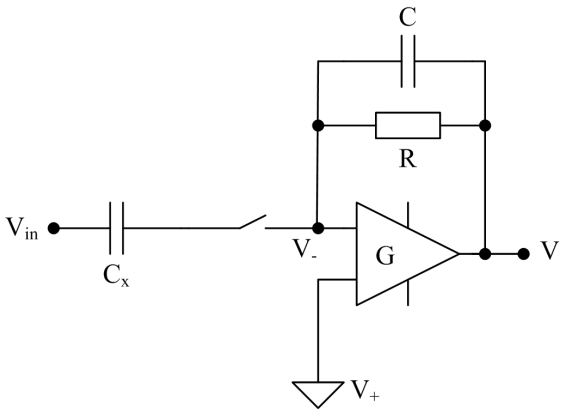

Figure 5.1: The circuit measures the magnitude of the unknown capacitance C_x. A square wave excitation, V_{in}, is applied to one side of the capacitance and the output voltage is a function of the unknown capacitance; $V = f(C_x)$.

A mathematical model of the circuit is constructed by an application of Kirchoff's current law to the '-'-input of the op-amp (the node with potential V_-) in figure 5.1. No current runs into the op-amp, so the equation for the current contains three terms; on for the current through the resistor and one for the current through each of the capacitors.

$$0 = C_x S \frac{\partial}{\partial t}(V_{in} - V_-) + C\frac{\partial}{\partial t}(V - V_-) + \frac{1}{R}(V - V_-) \tag{5.1}$$

where C_x is the unknown capacitance, S is the state of the switch, V_{in} is the input voltage (the square wave), V_- is the potential at the negative input node of the op-amp, C is the value of the capacitance in the CT circuit, R is the value of the resistor and V is the output voltage. The output voltage is given by the gain of the operational amplifier, G.

$$V = G(V_+ - V_-) \tag{5.2}$$

where V_+ is the potential which is applied to the positive input of the op-amp. The output voltage of the circuit is then described by the following differential equation:

$$0 = C_x s(t)\frac{\partial}{\partial t}(V_{in} + \frac{1}{G}V) + C\frac{\partial}{\partial t}(V + \frac{1}{G}V) + \frac{1}{R}(V - V_+ + \frac{1}{G}V) \tag{5.3}$$

Isolating V on the right hand side gives:

$$\frac{1}{R}V_+ - C_x s(t)\frac{\partial}{\partial t}V_{in} = (\frac{C_x s(t)}{G} + C(\frac{1+G}{G}))\frac{\partial}{\partial t}V + \frac{1+G}{GR}V \tag{5.4}$$

It is helpful to define

$$\tau_s = s(t)C_x R + RC(1+G), \tag{5.5}$$

to simplify the notation. This time-constant depends only slightly on the state of the switch, since the gain of the op-amp is very large compared to the magnitude of the other terms. The governing equation is a well known linear differential equation for V with exponential functions as solutions to the homogeneous case.

$$\frac{G}{\tau_s}V_+ - \frac{RC_xGs(t)}{\tau_s}\frac{\partial}{\partial t}V_{in} = \frac{\partial}{\partial t}V + \frac{1+G}{\tau_s}V \tag{5.6}$$

The two terms which make the equation non-homogeneous are a constant term and a time-varying term which is proportional to the time-derivative of the input voltage, V_{in}. For most of the time V_{in} is constant, which leaves only the constant term for the non-homogeneous part of the equation.

Regardless of the state of the switch, the solution for V can be shown to follow an exponential decay, for most of the time. The output voltage, V, decays towards the reference voltage of the operational amplifier, with a time-constant which depends on the state of the switch. Without the charge-injection term, the governing differential

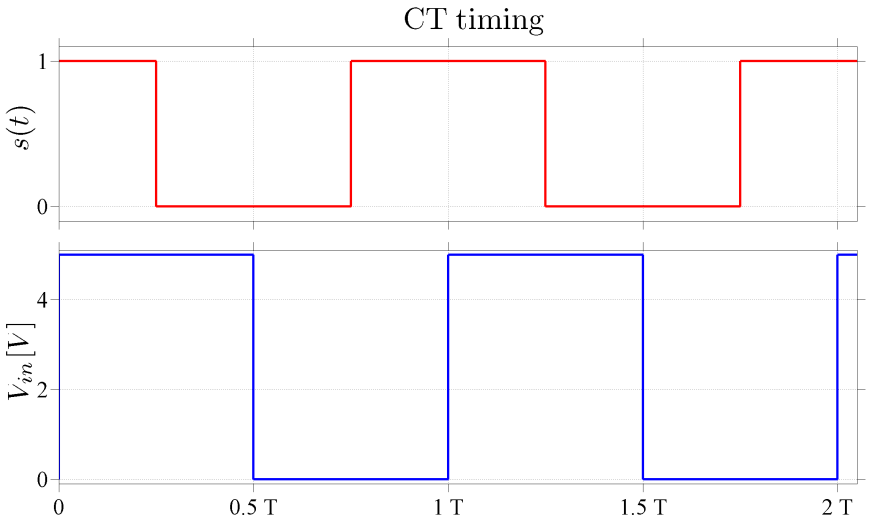

Figure 5.2: The figure shows the relative timing of the square wave and the switch. The op-amp is connected to the electrode for half of a period, so charge is only transfered once every period. The amplitude of the square wave is 5V.

equation is

$$\frac{G}{\tau_0}V_+ = \frac{\partial}{\partial t}V + \frac{1+G}{\tau_0}V \tag{5.7}$$

The solution to the homogeneous equation is en exponential decay.

$$V_{hom} = ke^{-\frac{1+G}{\tau_0}t} \tag{5.8}$$

Dividing the entire equation by the homogeneous solution leads to a convenient expression for the right hand side.

$$\frac{G}{\tau_0}V_+ e^{\frac{1+G}{\tau_0}t} = e^{\frac{1+G}{\tau_0}t}\frac{\partial}{\partial t}V + e^{\frac{1+G}{\tau_0}t}\frac{1+G}{\tau_0}V \tag{5.9}$$

$$= \frac{\partial}{\partial t}e^{\frac{1+G}{\tau_0}t}V \tag{5.10}$$

The solution can now be found by integration of both sides.

$$\frac{GV_+}{\tau_s}\int_{\frac{T}{4}}^{t} e^{\frac{1+G}{\tau_s}t'} \quad dt' = \int_{\frac{T}{4}}^{t}\frac{\partial}{\partial t'}e^{\frac{1+G}{\tau_s}t'}V \quad dt' \tag{5.11}$$

$$\frac{GV_+}{\tau_s}\left[\frac{\tau_0}{1+G}e^{\frac{1+G}{\tau_s}t'}\right]_{\frac{T}{4}}^{t} = \left[e^{\frac{1+G}{\tau_s}t'}V\right]_{\frac{T}{4}}^{t} \tag{5.12}$$

$$\frac{GV_+}{1+G}\left(e^{\frac{1+G}{\tau_s}t} - e^{\frac{1+G}{\tau_s}\frac{T}{4}}\right) = \left(e^{\frac{1+G}{\tau_s}t}V - e^{\frac{1+G}{\tau_s}\frac{T}{4}}V_0\right) \tag{5.13}$$

$$V = V_+\frac{G}{1+G} + e^{\frac{1+G}{\tau_s}(\frac{T}{4}-t)}\left(V_0 - V_+\frac{G}{1+G}\right) \tag{5.14}$$

When either the input voltage is constant or the switch open, the output voltage thus decays toward the reference value of the operational amplifier. The time constant of the decay depends on the state of the switch.

$$\frac{1+G}{\tau_s} = \begin{cases} \frac{1}{RC} & s(t) = 0 \quad \text{(open)} \\ \frac{1+G}{C_x R + RC(1+G)} & s(t) = 1 \quad \text{(closed)} \end{cases} \tag{5.15}$$

When the switch is closed and the input voltage has a non-zero derivative, charge is injected into the circuit, or into the electrode, depending on the sign of the derivative, which causes a change in the output voltage. In that case, all terms in the governing differential equation must be included.

$$e^{\frac{1+G}{\tau_1}t}\frac{\partial}{\partial t}V + e^{\frac{1+G}{\tau_1}t}\frac{1+G}{\tau_1}V = e^{\frac{1+G}{\tau_1}t}\frac{G}{\tau_1}V_+ - e^{\frac{1+G}{\tau_1}t}\frac{RGC_x}{\tau_1}\frac{\partial}{\partial t}H \tag{5.16}$$

Once more, the homogeneous solution is used to simplify the right hand side and the solution is found by integration. Since the change in input-voltage is abrupt, the time interval for the integration is very small. To obtain a relatively simple solution, we will let the time interval go towards zero, but it would also be possible to evaluate the integrals over a finite interval if a more realistic excitation function was used. The integrals will be evaluated on a time interval $[t_-, t_+]$ which is placed symmetrically around the time where $s(t) = 1$ and the square wave changes value. On figure 5.2 this

is at $t \in [T, 2T, ...]$.

$$\int_{t_-}^{t_+} \frac{\partial}{\partial t'} e^{\frac{1+G}{\tau_1}t'} V \quad dt' = \int_{t_-}^{t_+} e^{\frac{1+G}{\tau_1}t'} \left(\frac{G}{\tau_1} V_+ - \frac{RGC_x}{\tau_1} \frac{\partial}{\partial t'} H \right) \quad dt' \tag{5.17}$$

$$\left[e^{\frac{1+G}{\tau_1}t'} V \right]_{t_-}^{t_+} = \left[\frac{\tau_1}{1+G} e^{\frac{1+G}{\tau_1}t'} \frac{G}{\tau_1} V_+ \right]_{t_-}^{t_+} - \int_{t_-}^{t_+} \frac{RGC_x}{\tau_1} e^{\frac{1+G}{\tau_1}t'} \frac{\partial}{\partial t'} H \quad dt'$$

$$\Delta V = -\frac{RGC_x}{\tau_1} \int_{t_-}^{t_+} e^{\frac{1+G}{\tau_1}t'} \frac{\partial}{\partial t'} H \quad dt'$$

$$= -\frac{RGC_x}{\tau_1} \left(\left[e^{\frac{1+G}{\tau_1}t'} H \right]_{t_-}^{t_+} - \int_{t_-}^{t_+} \frac{1+G}{\tau_1} e^{\frac{1+G}{\tau_1}t'} H \quad dt' \right)$$

$$= - \pm \frac{RGC_x}{\tau_1} |H| + \frac{RGC_x}{\tau_1} \int_0^{t_+} \frac{1+G}{\tau_1} e^{\frac{1+G}{\tau_1}t'} \quad dt'$$

$$\Delta V = \mp \frac{RGC_x}{\tau_s} |H| \tag{5.18}$$

The change in voltage, ΔV, can be either negative or positive, depending on the sign of the derivative of the input voltage. On figure 5.2 the sign is positive and the opposite effect would be achieved by reversing the action of the switch. The output voltage decays exponentially for most of the time, but is abruptly changed by ΔV every time the switch is open and the input voltage changes. A semi-steady state is reached when the constant charge that is pumped into the circuit at each switch,

$$V_{top} - V_{bottom} = \Delta V \tag{5.19}$$

is equal to the charge that is lost through exponential decay.

$$V_{top}(1 - e^{-\frac{1}{RC}T}) = \Delta V$$

$$V_{top} = \frac{\Delta V}{1 - e^{-\frac{1}{RC}T}} \tag{5.20}$$

In the derivation above, the decay rate has been approximated as constant since, as mentioned previously, the decay rates are nearly equal for $s = 0$ and $s = 1$. The mean of oscillating output signal after reaching the semi-steady state is

$$\bar{V} = \frac{1}{T} \int_0^T V_{top} e^{-\frac{1}{RC}t'} \quad dt'$$

$$= \frac{V_{top}}{T} \left[RC e^{\frac{1}{RC}t'} \right]_0^T$$

$$= \frac{V_{top}}{T} RC (1 - e^{\frac{1}{RC}T})$$

$$= fRC\Delta V$$

$$= fRC_x \Delta V |H| \tag{5.21}$$

In a practical application, tow of the circuits shown in figure 5.1 would be connected to each electrode. The switches of the two circuits would then be out of phase with π such

the charge transfered to each of the circuits in each time period are of equal magnitude and with opposite signs. The two outputs are then subtracted in a third op-amp, which also amplifies and offsets the signal. The total mean output of the CT channels is

$$\bar{V}_{CT} = 4.4 f R C_x |H| + 100mV \tag{5.22}$$

A numerical model of a CT circuit can be constructed in a piecewise manner, one period at a time, by letting the voltage change by ΔV periodically and then let the output voltage decay for the remaining time. Such a model has been compared to a model in PSpice[1] in figure 5.3. Comparing the models, shows that the predicted equilibrium values are accurate and that the oscillations are close to the more detailed model. There

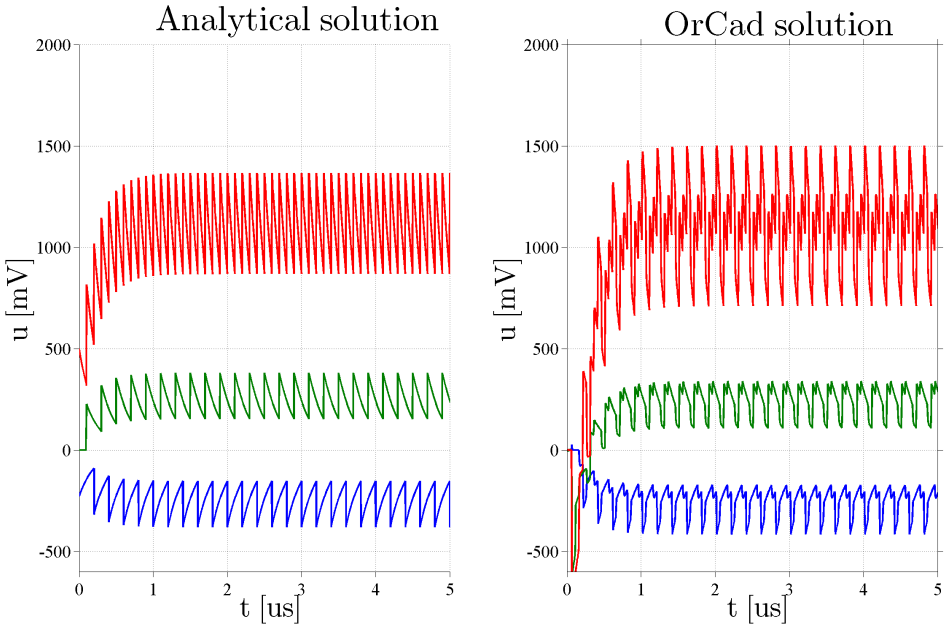

Figure 5.3: The figure shows two simulations of a CT circuit. The solution on the left shows the analytical solution which has been given in equations (5.14) and (5.18). The output from both parts of the CT circuit are plotted and the difference of the signals is plotted in red. The plot on the right side shows data from a simulation in PSpice. The small jumps in the voltage are caused by the internal capacitance of the switch. This effect is not included in the analytical model.

are some extra 'kinks' in the PSpice model which are not reproduced in the analytical model. These are caused by internal capacitances in the switches, which inject charge in the circuit when the switch is operated. The internal capacitance also affects the exponential decay which can be seen to have noticeably different decay rates for $s = 0$ and $s = 1$.

[1] PSpice is a circuit simulator. It was used from OrCad, which is a program for circuit design, but it is also possible to interface with it from MATLAB.

To measure the mean output, after the two op-amp signals are combined, a (low-pass) Butterworth filter is added to the circuit. This ensures that the output comes close to being DC voltage with the value stated in (5.22). The gain of the filter is

$$|A| = \frac{1}{\sqrt{1 + 4\omega^4 R^4 C^4}} \tag{5.23}$$

If a cut-off frequency of f_{cut} is desired, the value of RC needs to be

$$\frac{1}{\sqrt{1 + 4\omega^4 R^4 C^4}} = 10^{\bar{}\frac{}{3}20} \Rightarrow \tag{5.24}$$

$$RC = 4.55 \cdot 10^{-}4 \tag{5.25}$$

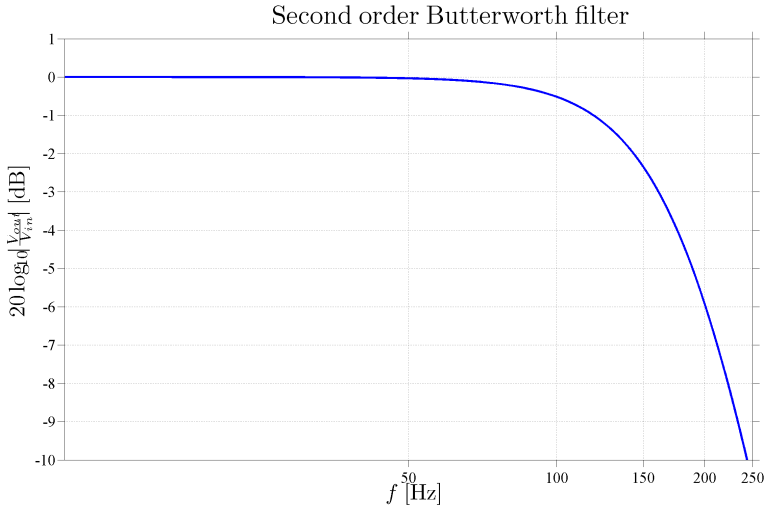

Figure 5.4: The figure shows the output characteristic of the low-pass filter at the output of the current transfer circuit.

The cut-off frequency of the high-pass filter is set well below the frequency of the input which is twice the frequency of the square-wave signal. To prevent non-ideal effects from the op-amp, the value of the components are also set such that the capacitors are at least in the nF range and the resistors are in the kΩ range. The output characteristic of the filter used in this project is shown in figure 5.4. The -6dB frequency of the filter is approximately 200Hz.

After the filter, the output signal is measured and converted to a digital value. The maximum resolution of the circuit is given by the analog to digital conversion. With a ten bit resolution over a range of 3.3 volts, the capacitance resolution is

$$\Delta c = \frac{3.3V}{4.4fR|H|}\frac{1}{1024b}$$

with a resistor of $10k\Omega$ and a frequency of 1.25MHz the resolution is

$$\Delta c = \frac{3.3V}{4.4fR|H|}\frac{1}{1024b} \tag{5.26}$$

$$\approx 12fF/b$$

It should be noted that even though the range and resolution of the sensor does not depend on the value of the capacitor in the circuit, the same is not true for the amplitude of the oscillation before the filter. The capacitance should be chosen such that the amplitude of the oscillations (see (5.20)) are limited.

More specific design details for the sensor-circuits are described in section 6.1 and test results are presented in section 7.1.

Chapter 6

Designs

This chapter presents the hardware and software that was produced to implement the theory described in chapters 5 and 4 and the test-facilities that were constructed to produce the results presented in chapter 7.

Two different hardware implementations of a CT circuit were used. They will be referred to as CT layouts 1 and 2. CT layout 1 was used in the construction of two different ECT sensors, sensor A and sensor B, and CT layout 2 was used in a third sensor, sensor C, which was used for the field test. Both CT layouts and the design of sensor A and C are presented here. CT layout 1 will be described in general terms as it is based on designs which are well documented by several sources. Layout 2 is described in more detail since.

Sensor	**Circuits**	**Power supply**	**COM**	**Downhole**
Sensor A	CT layout 1	Lab	RS-232 to laptop	No
Sensor B	CT layout 1	Tractor	RS-232 to tractor	No
Sensor C	CT layout 2	Tractor	SNAP[1] to tractor	Yes

Table 6.1: The table provides an overview of the features of the three inside-out sensor systems which were constructed.

Table 6.1 gives an overview of the differences between the three sensors. Sensors B and C were both designed to be mounted on a tractor, but only sensor C has a housing which can handle downhole pressures. Sensor A was used only for tests in the test-tank.

[1] The subnetwork access protocol (SNAP) is used for the internal communications bus of the tractor.

6.1 Circuit design

The charge transfer technique described in chapter 5 was implemented on printed circuit boards. In both CT layouts 1 and 2, microcontrollers were used to operate the CT circuits.

CT layout 1

CT layout 1 was based on the designs described by Huang, Xie, Thorn, Snowden and Beck [22] and the one described by Yang [3]. The print contains 8 CT channels. The description given here will provide an overview of the operating principle of the 8 channel test print. The main components in the system are 8 CT channels, 1 microcontroller and a shift register. Each electrode is associated with one CT channel on the board and the state of each channel is controlled by the microcontroller. A CT channel can either send an excitation signal, measure or be passive.

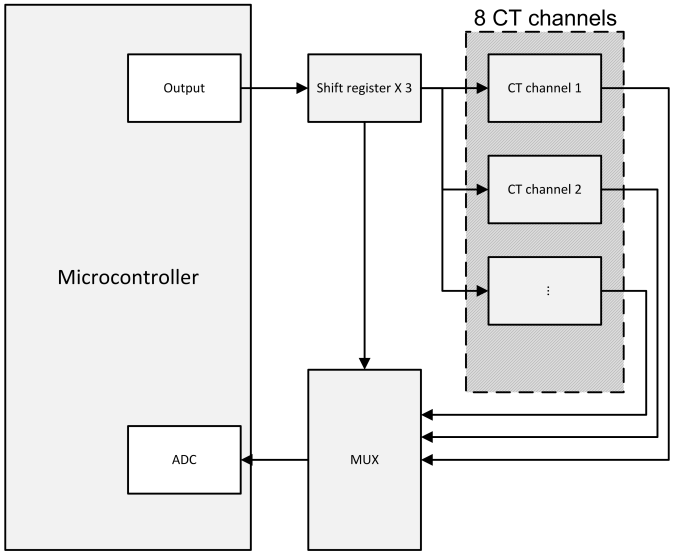

Figure 6.1: The figure shows the test print. The microcontroller sets the state of all the CT channels as well as the state of the multiplexer (MUX) through the three shift registers. After a settling period, a number of measurements are taken by the analog to digital converter in the microcontroller.

Figure 6.1 shows the principal layout of the testprints. The channels are controlled by a microcontroller from three 8-bit shift registers. Each channel is connected to two of the shift register outputs. If the two bits are set to [1 0] the CT channel sends an excitation signal, if they are set to [0 1] the CT channel measures and [0 0] ensures that the channel is grounded.

When an electrode is set as the excitation electrode, a square-wave signal is applied

to it. The 2.56MHz square wave is generated indirectly by the microcontroller via switches which are connected to the 0V and 5V supplies.

The outputs of the eight channels are connected to an 8-channel multiplexer which in turn is also controlled by the microcontroller through the shift registers. The output of the multiplexer is connected to the analog to digital converter on the microcontroller and the multiplexer is then set up to put the output signal of the currently measuring CT channel through to the 10-bit ADC.

The range of the ADC is from 0V to 5V which results in a resolution of 4.9mV. The ADC takes samples at 15MHz and is set up to sample 32 times with 25μs between each sample. After the system switches to a new channel it is allowed 1ms to settle and the 32 measurements are then performed. A total time of

$$T = 1\text{ms} + 32 \cdot 25\mu\text{s} = 1.8\text{ms}$$

is thus required for the measurement of a single capacitance. With this setup the maximum frame rate of the system is then

$$f = \frac{1}{28 \cdot 1.8\text{ms}} = 19.8\text{Hz}$$

which is enough to provide 'live' imaging. The capacitance data are transmitted to a laptop from the microcontroller via a small RS-232 module (on an external print).

CT layout 1 measures 100mm by 132mm. This is too large to fit inside any of the standard housings used for tractor modules.

The electrodes are connected to the CT channels via 50Ω BNC cables which is convenient for a lab setup, since many different sensor-heads (a simple design is described in section 6.2) can be used with the same electronics. The long cables do contribute to the uncertainty of the measurements though, so this design is mainly intended for testing purposes.

CT layout 2

Experience with CT layout 1 lead to the design CT layout 2. The main design goal was to alter the layout in such a way that the CT system, circuit-boards and electrodes, could fit inside a standard housing. Another goal was to place the CT channels as close to the electrodes as possible.

It was decided to make a set of many smaller circuit-boards, such that each CT channel was placed on its own separate board and could be placed directly behind an electrode (and behind the inner screen). The 8 CT boards were designed so they could be mounted on a cylinder with an outer diameter of 34mm.

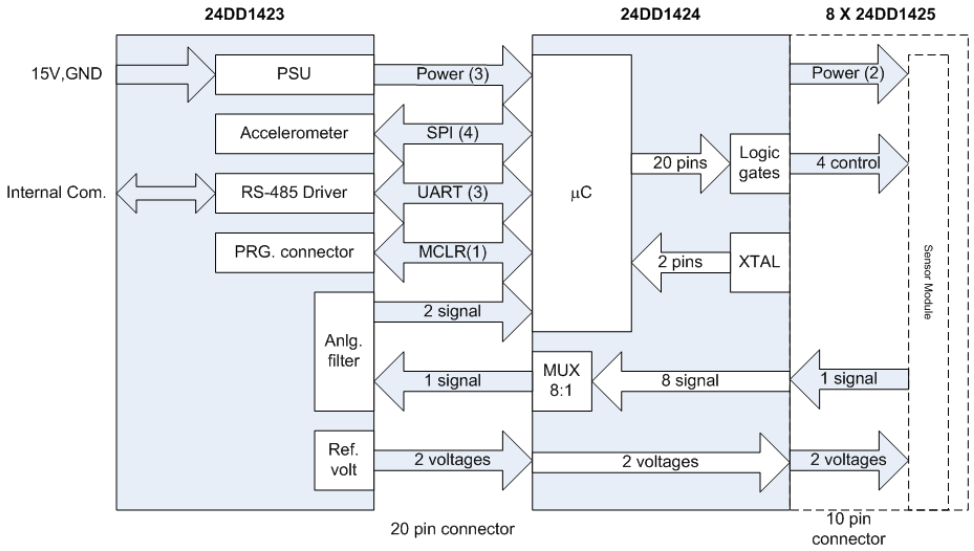

Figure 6.2: The figure shows a schematic of the interconnections of the three boards of CT layout 2. The eight CT channels and the multiplexer (MUX) are controlled by the microcontroller as in the test layout.

The central components of the electronics were placed on 2 other prints. One board to contain the power supplies and one board to contain the multiplexer and microcontroller. The board with the power supplies also contains an RS-485 driver for communication and an accelerometer which is used to orient the tomogram with respect to gravity. The x-, y- and z-values are read by the microcontroller along with the capacitance measurements. The structure and format of the data sent over the internal BUS is documented in table A.1.

As on the first layout, the microcontroller is the central component in the system. As soon as the voltage rises to the proper level, the program on the microcontroller initiates execution. The algorithm simply cycles through all the unique electrode combinations. For each combination one electrode is chosen as the active electrode and one as the measurement electrode. A square wave excitation is sent by the active electrode and the output of the CT-circuit on the measurement electrode is passed through the multiplexer to a second Butterworth filter, before entering the analog to digital converter.

After finishing a frame of 28 measurements, the data is made available in the output buffer by the microcontroller through the RS-485 controller on print 24DD1423. The algorithm which is executed by the microcontroller is illustrated in figure 6.4.

The CT circuits were only slightly altered from the test layout. The reference voltage of the CT circuit op-amps was moved from 0V to 2.5V and the cutoff frequency of the Butterworth filters were lowered significantly. See figure 6.3 for details.

An additional op-amp was added to the ADC input so an amplification of unity or 16

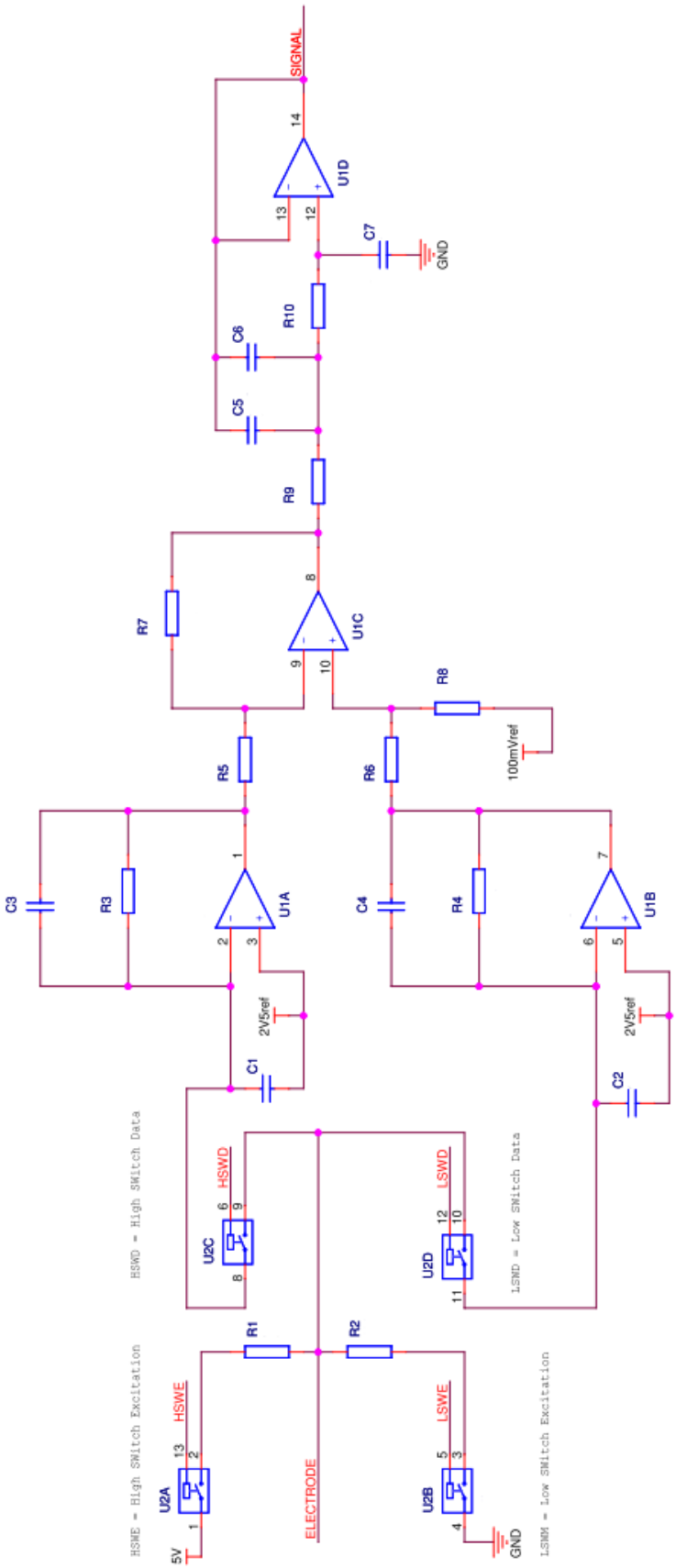

Figure 6.3: The figure shows the layout of a single CT channel for CT layout 2. The op-amp setup shown in figure 5.1 is used with U1A and U1B. The output of the two channels are subtracted from each-other as described in chapter 5 in U1C. U1D is set up as a Butterworth filter. The output put through another identical Butterworth filter before conversion to a digital value. Notice that the reference voltage for the CT op-amps (pins 3 and 5 on U1) is set to 2.5V.

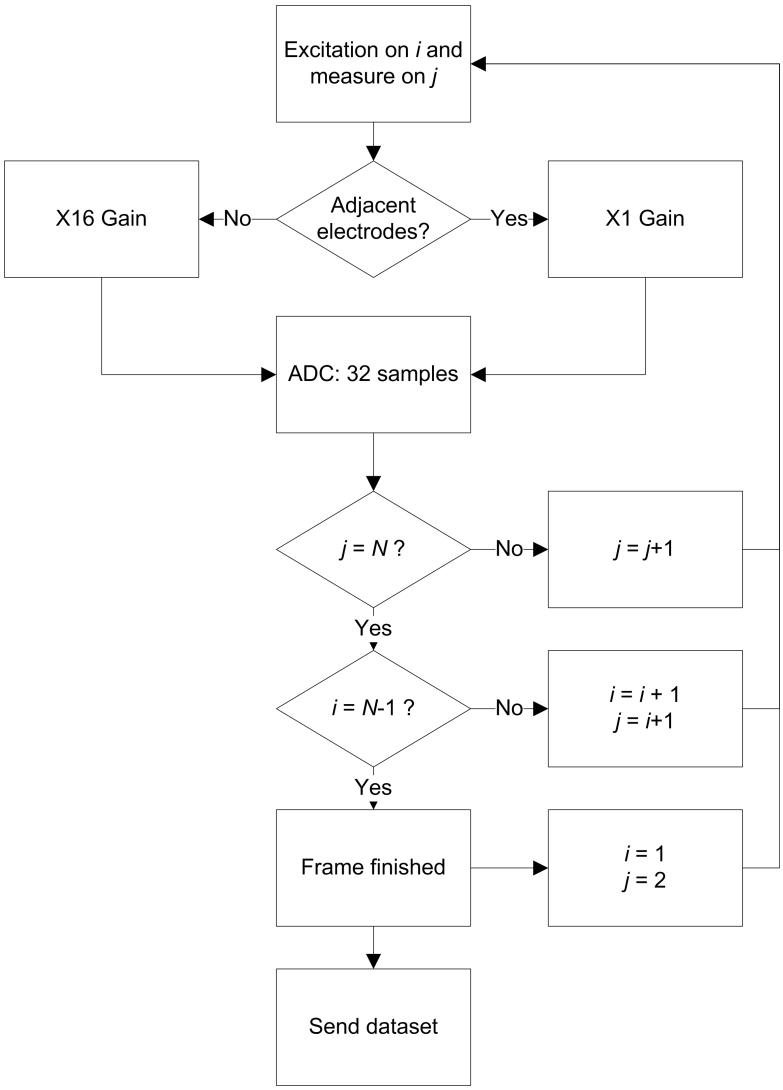

Figure 6.4: The figure illustrates the program which runs on the microcontroller. An electrode pair is chosen and activated. Depending on the distance between the electrodes, an amplification factor of 1 or 16 is chosen. The ADC then performs 32 samples, before the next electrode pair is chosen. The number of electrodes for the system is $N = 8$. After a set of 28 measurements is finished, the data are sent to the output buffer and a new cycle is initiated.

can be selected. This enables the smallest capacitances to be measured with greater resolution and thus leads to better effective resolution for the reconstructed tomogram.

6.2 Sensors

Section 6 described the two CT layouts and the three sensors which employed those layouts (see table 6.1): sensors A, B and C.

Mockup sensor-head

This section outlines the design of a simple mockup sensor-head. The advantage of the mockup is that it is quickly and cheaply constructed and that the electronics are easily accessible during operation.

The mockup sensor-head is built from three tubes with different diameters. A middle tube made from poly-ether-ether-ketone (PEEK) is used to mount the electrodes and screens. The outer screen made from PVC is used to isolate the electrodes from the flow. An inner tube of aluminum is used as an inner screen. All three tubes are shown in figure 6.5. The diameter of the thinnest part of the aluminum tube was 30mm. This is not indicated on the drawing.

The three tubes are placed inside each other and BNC cables are drawn from the electrodes on the middle tube through the inside of the aluminum tube to the electronics (see figure 6.7).

The wiring for the sensor-head is shown in figure 6.6. Resistors of 1MΩ are mounted between each electrode and the screen, to avoid static charge building up. The BNC cables are then connected to the electrode and the screens. The holes for the wiring can be seen in figure 6.7.

Grounded screens are placed on each side of the electrodes and 1.5m BNC cables are used to connect each electrode to a terminal on the CT board. The electrodes are made from conductive aluminum tape. Both screens and electrodes have a width of 5cm.

The mockup sensor-head is constructed by first soldering all connections on tube B, then sliding tube C along the BNC cables until it is placed inside tube B. Finally the two tubes and wires are slid inside of tube A so that the electrodes are protected by the outer, non-conductive, tube and can be connected to an ECT print through the BNC cables.

Sensor B

The mockup sensor was used to verify that CT layout 1 was working satisfactorily. The combination of sensor-head and electronics which was used for this proof-of-concept

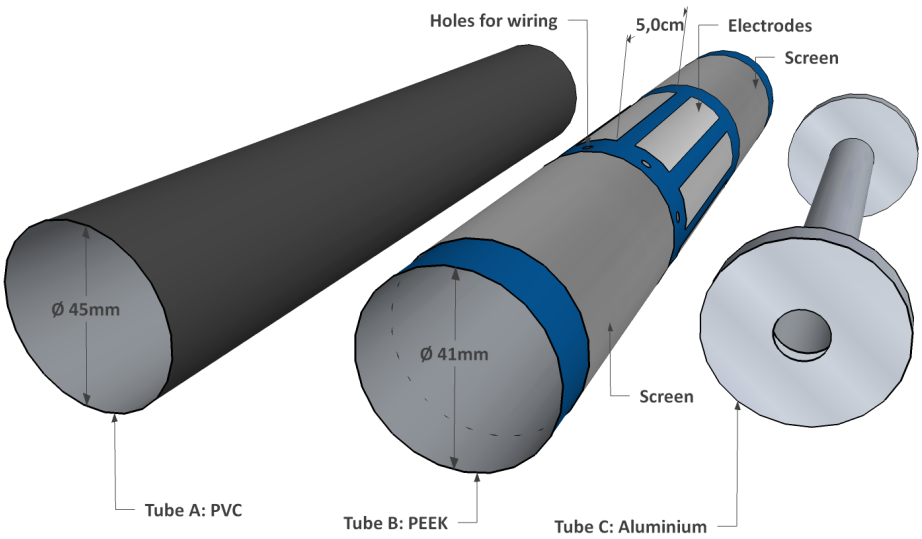

Figure 6.5: The image shows the parts of the mockup sensor-head. The electrodes and screens are cut from the conductive tape and mounted on the outside of tube B. The spacing between the electrodes has been exaggerated on the drawing; the actual distance between the electrodes is 1mm.

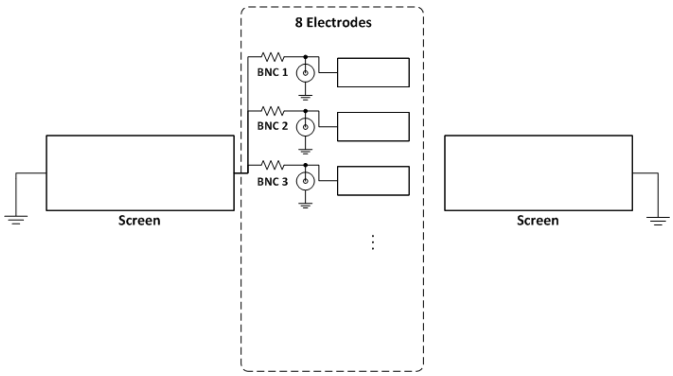

Figure 6.6: The image shows the wiring inside the test sensor. Each electrode is connected to a BNC cable through a hole in the smallest tube. Each electrode is connected to one of the screens through a 1MΩ resistor to avoid buildup of static charge. Figure 6.7 shows the holes in the tubes which the wires are drawn through.

was called sensor A.

A test run was subsequently scheduled in the test loop (see section 6.3). Some changes needed to be made to the sensor in order for it to be mounted on and be powered by a tractor. This sensor is called sensor B.

A housing was produced for CT layout 1. Since the CT board is too large to fit inside any regular tractor-housings, a piece of PVC tubing was used instead. A standard con-

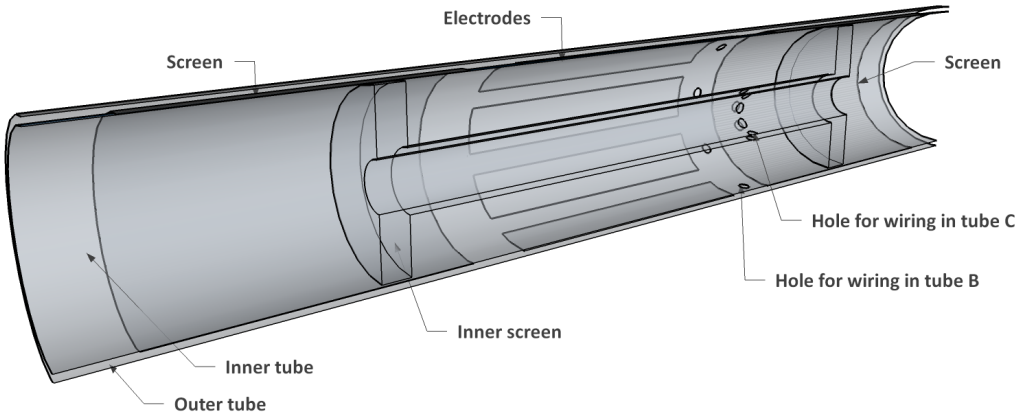

Figure 6.7: The image shows the inside of the sensor after it has been put together from the three parts shown in figure 6.5. The holes for the wiring are visible. After the BNC cables are drawn through the holes, they run inside the inner screen (tube C).

nector[2] was used to mount the sensor on the tractor and provide power and wireline-COM.

Sensor B is shown on figure 6.8. The smallest tube in the image contains a mockup sensor-head and the larger part of the sensor contains the prototype electronics.

The results of the test run in the loop is shown in section 6.3.

Sensor C

To enable the sensor of operating in downhole conditions, a sensor using CT layout 2 was produced. Sensor C was produced in a standard tractor housing. The outer diameter of the non-conductive electrode-cover was 54mm. The electrodes where placed with an outer diameter of 48.8mm and the outer diameter of the inner screen is 43mm. A picture of the sensor is shown in figure 6.9. A patent application [39] covering the design was filed in October 2009.

The electronics layout has already been described in section 6.1. The channels on the prototype print are connected to the electrodes via brass bolts that run through the sensor. This enables the electronics to be placed almost directly behind the electrodes and thus the distance from electrode to CT channel to be very small.

[2]The connector is called a tandem connector.

Figure 6.8: The image shows sensor B. The housing is part PVC tube and part aluminum connectors.

Figure 6.9: The image shows sensor C. The electrode-cover is made from fiberglass on the version shown here.

The electrode-cover was designed to be made of zirconium oxide, in which case the sensor can operate in pressures of 350Bar. An electrode-cover made from fiberglass was used for the calibration and tests which are reported in section 7.

Sensor C weighs just 4kg and has a total length of 0.5m.

6.3 Test facilities

Test tank

As an initial test platform for the flow-sensors, a simple test tank was constructed. The setup consists of an aluminum frame to support a 160cm×50cm×50cm (400L) aquarium.

The tank can be filled with oil and water. The oil used is rapeseed oil which has a relative permittivity[40] of approximately

$$\varepsilon_{oil} = 2.5$$

The test tank contains a piece of grounded metal casing which is grounded to the power supply of the CT board. The head of the sensor is centralized inside the casing and the BNC cables connect it to the sensing electronics outside the test tank.

The casing, with the sensor inside, can be raised and lowered in the tank and the phase distribution can thus be adjusted as desired.

Test Loop

The test loop is a 200m section of casing at Welltec in Allerød, Denmark. There are five parallel loops, with different diameters.

The casing with the largest diameter, 225mm, is the one which has been used for all tests with the ECT sensors. The layout of the loop is shown in figure 6.12, which shows a view from above and from the side. The test loop has a sharp bend after around 100m. It should also be noted that the middle section is lower than the ends. This enables the loop to be filled with water. Figure 6.11 shows an image of the testloop.

The loop has been equipped with an inlet for water close to the lowest part. An inlet for air has also been added as well as an outlet at the lowest section of the loop.

Calibration for test in the loop could be performed in the test tank, using a piece of Ø225mm casing, but it could also be performed directly in the loop. The sensor was

Figure 6.10: The test tank at Welltec. The broomstick is used to raise/lower the casing with centralized sensor in the tank.

Figure 6.11: The test loop at Welltec. The casing size shown here is Ø225mm; the one used for the tests. The picture is taken approximately at the point (150, 70), on the upper plot in figure 6.12, in the negative y-direction.

then positioned in a part of the loop which was filled with air (somewhere near the beginning of the loop) and a sufficiently large set of capacitance frames where recorded

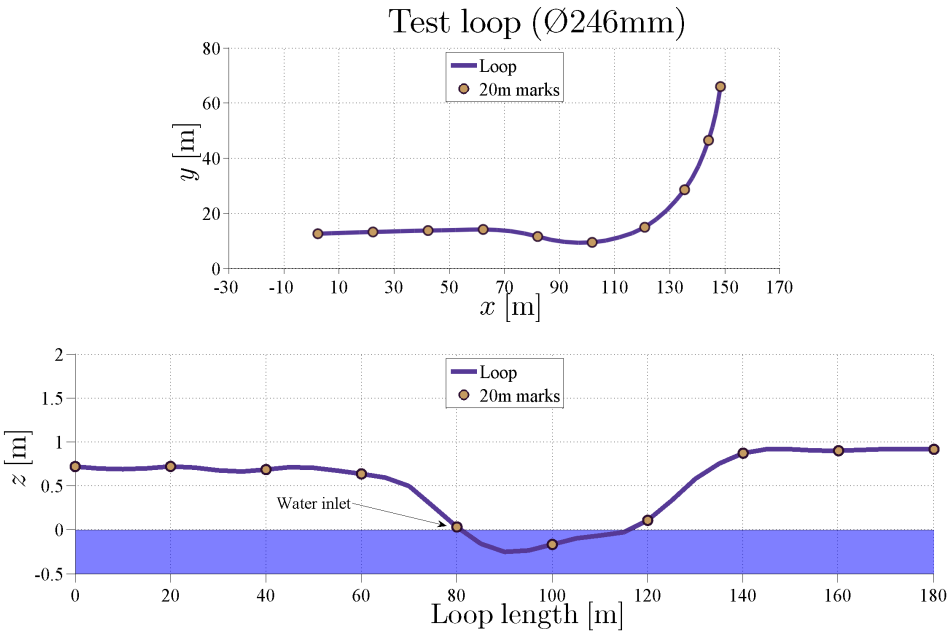

Figure 6.12: The figure shows a graph of the layout of the test-loop. The upper plot is a top-down view which shows the bend on the loop. The lower plot is a plot of the height of the loop as a function of loop-length. The 20-marks can be used to compare positions on the two plots.

before powering up the tractor and positioning the sensor in the lower part of the loop where the second part of the calibration set was recorded.

6.4 Calibration setup

The quality of the tomograms produced by ECT is very dependent on the accuracy of the calibration. Consequently, the construction of a calibration setup is an integral part of an ECT system. The calibration of sensors A and B could be performed inside the test tank. Sensor C was intended to run in a real test-well and it was thus necessary to perform a pre-run calibration.

The schematic for the intended test-well, was obtained and then used to determine the tube diameter to use in the calibration. The well contained mostly sections of pipe with one of 3 inner diameters. Aluminum pipe of 96mm, 116mm and 126mm diameters was acquired for the purpose.

A calibration feature was added to the MATLAB interface to simplify the procedure. The GUI is described in chapter B. Typically calibration was performed in each phase for approximately two minutes which provides over 1000 data points for the calibration.

Figure 6.13: The calibration setup. Foam centralizers are used to make sure that the sensor is located in the middle of the tube. After obtaining the air-calibration, the tube with sensor is lowered into the bucket which is filled with water, thus obtaining the water-calibration.

Calibration results are presented and discussed in section 7.2.

A graphical user interface specifically for calibration was written in MATLAB. A screenshot of the interface is shown in figure 6.14. The purpose of the GUI is to easily be able to create a calibration file from a data set. The plots in the interface make it easy to

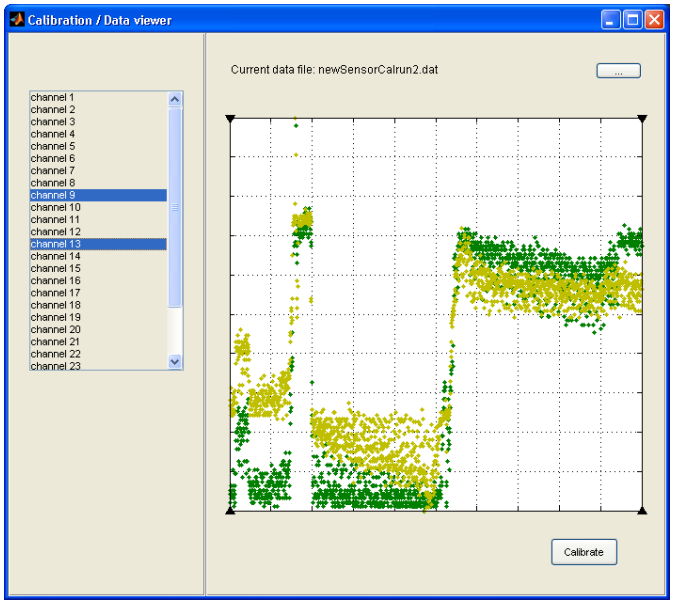

Figure 6.14: The image shows a screenshot of the calibration interface with a dataset loaded. The graph on the right shows the chosen channels of the loaded data. The transition from water to air is clearly visible in the data. By dragging the four markers in the corners with the mouse, the calibration intervals are selected.

select a time-interval to use for creation of the calibration-file. The calculated value of

the calibration vectors is the simple mean inside the chosen interval.

$$[\boldsymbol{c_h}]_i = \frac{\sum_{j=m_h}^{n_h} c_{ij}}{n_h - m_h + 1}$$
$$[\boldsymbol{c_l}]_i = \frac{\sum_{j=m_l}^{n_l} c_{ij}}{n_l - m_l + 1}$$

where $([\boldsymbol{c_h}]_i, [\boldsymbol{c_l}]_i)$ is the (high,low) calibration set for electrode-pair i, c_{ij} is the j'th measurement of the capacitance between electrode-pair i and the interval $[m_x n_x]$ is chosen for the high or low calibration.

The interface makes it possible to plot as many channels as desired. In figure 6.14 two channels are chosen. Sometimes the change from high to low is not as abrupt as on the figure, so it is advised to inspect several channels to make sure that the capacitance value of all channels have converged to a stable value.

Chapter 7

Results

Several tests of the ECT systems were performed. This first part of this chapter is a documentation of the tests of CT layout 2. The last parts show the results of some system tests of the prototype sensor.

7.1 Test of CT layout 2

CT layout 2 was tested in three separate stages. The first stage of the tests of the CT circuits was performed by comparing the output to the mathematical model of the circuits in (5.22). The two next stages were the most critical tests. They included an investigation of the capacitance resolution of the CT circuits and a heat test where the electronics were operated for several hours in a high temperature environment.

To set the electronics up for these tests, ceramic capacitors were mounted between 4 pairs of electrodes in such a way that all CT channels could be tested as both sender and receiver. Capacitances of 1.1pF were mounted between every other adjacent pair of electrode-channels as described in table 7.1.

Electrode pair	Capacitance value
1-2	1.1pF
3-4	1.1pF
5-6	1.1pF
7-8	1.1pF

Table 7.1: The table shows the positions of the capacitances which were mounted for the test of the CT circuits. Each electrode was connected to one side of a capacitance of 1.1pF.

`pwmdiv d`	Set the divisor for the frequency of the driving square wave signal. $f_{sq} = \frac{10MHz}{d}, \quad d \in [4, 8, ..., 20]$.
`measure i j`	Send the square wave signal on electrode `i` and send the output from circuit `j` through the multiplexer.
`adc n a`	Obtain `n` samples from the ADC with an amplification of `a`. The only allowed amplifications are 1 and 16.

Table 7.2: The table shows the commands which could be issued to the microcontroller via the serial interface. The small set of commands was sufficient for the operation of the CT circuits during testing.

```
CMD> measure 5 6
Setup up channel 5 -> 6

CMD> adc 1 128
Mean = 509, Min = 492, Max = 526
Voltage = 0.4104
Excitation frequency = 1.25
```

Figure 7.1: A screen-shot of the command prompt during a test of CT layout 2. The output to `stdout` after an `adc` command shows the mean value of the measurements, both as a bit-value and as a voltage. The maximum and minimum value in that set of samples, as well as the square wave frequency, is shown.

Furthermore, the micro-controller (see the circuit diagram in figure 6.2) was programmed such that the state of the circuits could be controlled via a serial interface from a PC. Three commands were available. One command to set the frequency, one to select the active and the measuring electrode and one to activate the ADC. The syntax for the commands are listed in table 7.2 along with a short description.

The highest possible excitation frequency was 2.5MHz with a divisor of 4 and with increasing divisors the possible excitation frequencies were 1.25MHz(default), 833kHz, 625kHz and 500kHz. The output buffer is 16-bit although the resolution of the ADC was only set to 10 bit so it would be possible to improve the ADC resolution without affecting the frame rate.

An example of a small test session is shown in figure 7.1. The circuits are being set up to send on channel 5 and receive on channel 6. The ADC is then set up to record 128 samples at unity gain. The output of the `adc` command shows the mean bit-value of

the 128 samples and the value of the highest and lowest sample. The min and max bit can be used as a pseudo-standard deviation. For a measurement of the actual standard deviation, it is necessary to perform a series of single sample measurements and then find the standard deviation of the series.

Testing the CT channels

As an initial test of the CT circuits, the serial interface was used to investigate the frequency dependence of the CT circuits and to test whether the measured value of the capacitance corresponded to the nominal value of the mounted capacitors.

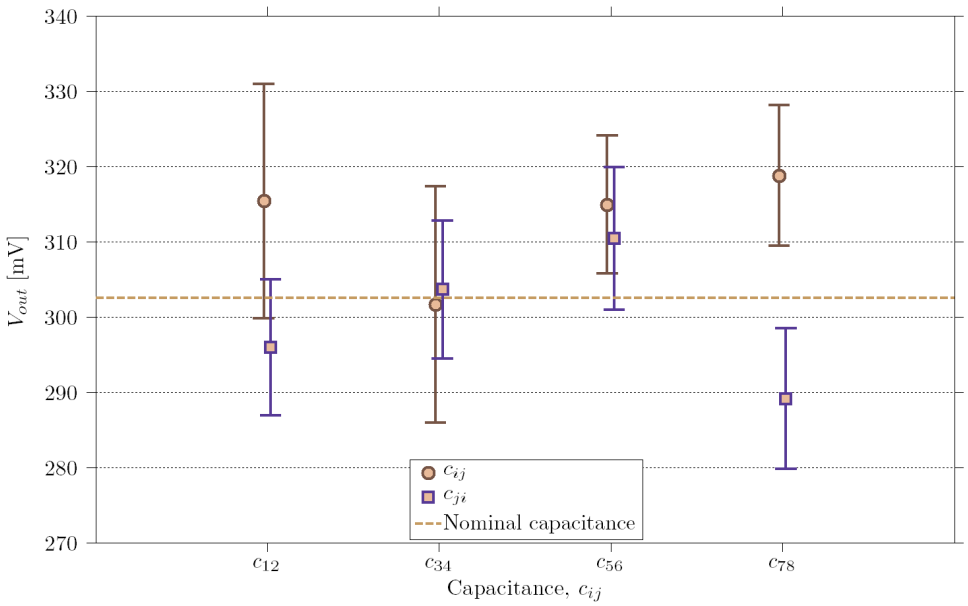

Figure 7.2: The plot shows a set of test measurements. Each of the four capacitances were measured by either of the CT circuit connected to its legs. For example; c_{12} was measured 2048 times with circuit 1 and then 2048 times with circuit 2. The dashed line indicates the output voltage corresponding to a capacitance value of 1.1pF.

As is shown in figure 6.2, there are two connections from the second stage of the Butterworth filter to the ADC. One connection is through a unity gain buffer and the other is through a times 16 gain buffer. The range of the ADC is from 0V to 3.3V, so for the high gain buffer the output saturates at frequencies above 852kHz (when the size of the capacitance is 1.1pF). With a resistance of 10kΩ, two 2.2pF capacitors in series between the electrodes and an excitation voltage amplitude of 5V, the output is expected to obey

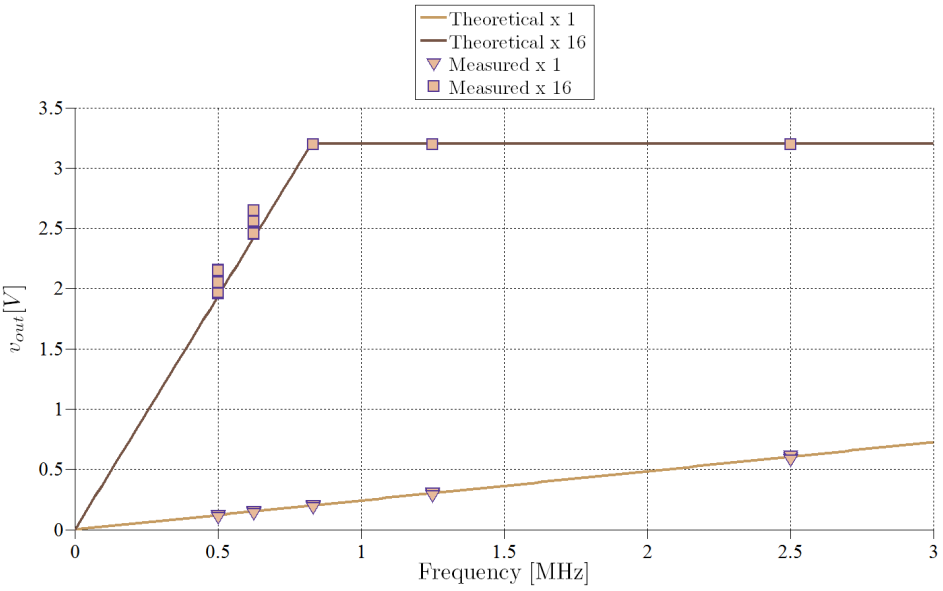

Figure 7.3: The plot shows the results of some test measurement. The full lines show the relationship between frequency and output voltage predicted by (7.1). The ADC works in the range from 0V to 3.3V, so the x16 measurements saturates at frequencies above 852kHz.

the following relationship (see (5.22)):

$$\begin{aligned} V_{out} &= 4.4 \cdot 1.1pF \cdot 5V \cdot 10k\Omega \cdot f \cdot G \\ &= 242\frac{mV}{MHz} \cdot f \cdot G \end{aligned} \tag{7.1}$$

where f is the excitation frequency and G is the gain which can be either 16 or unity.

Figure 7.2 shows the output voltage of the CT circuits with an excitation frequency of 1.25MHz, at unity gain. Without adjusting for any offsets of the the different channels, the measured capacitances lie within 10% of the nominal value, which is within the tolerance of the mounted capacitances. Each capacitance is measured twice and except for channels 7 and 8, the measurements by the channel-pairs lie within the standard deviation of a single channel, but since the measurement is based on the mean of 2048 measurements, there is clearly an offset between the channels. The offset will be compensated by the sets of calibration measurements, so it does not pose a problem.

A test of the frequency dependency of the CT circuits is shown in figure 7.3. Each capacitor was measured four times; once by each of the channels connected to it at unity gain and once more by each channel at the high gain. Each measurement was based on 128 ADC samples. The high gain channel saturates above 833kHz, as expected, and the measurements follow the theoretically predicted values closely. The tests show that the CT circuits behave as expected.

In the final version of the microcontrollers code, CT layout 2 operates with a constant frequency of 1.25MHz. The two different gains were used to better resolve the small capacitance changes, which are expected on the non-adjacent electrode pairs. Adjacent electrode pairs were thus be sampled through the unity gain buffer and all other electrode pairs were sampled through the high gain buffer.

Heat test

The sensor has to be able to operate in downhole conditions, which means that both high temperature and high pressure must be tolerated. The field test was to be conducted on BP's Andrew field, which reaches temperatures of 112° C, so the electronics were tested in an oven. The temperature in the oven was measured with a Pico technologies type K thermocouple on a TC-08 USB temperature data logger. The TC-08 was interfaced directly from MATLAB through the .dll files for the logger. An inspection of table A.1, which shows the structure of the data packets sent by CT layout 2, will reveal that the 2 last bytes contain a temperature value. This is the temperature of the microcontroller and not the ambient temperature, so it could not be used for the purpose of this test.

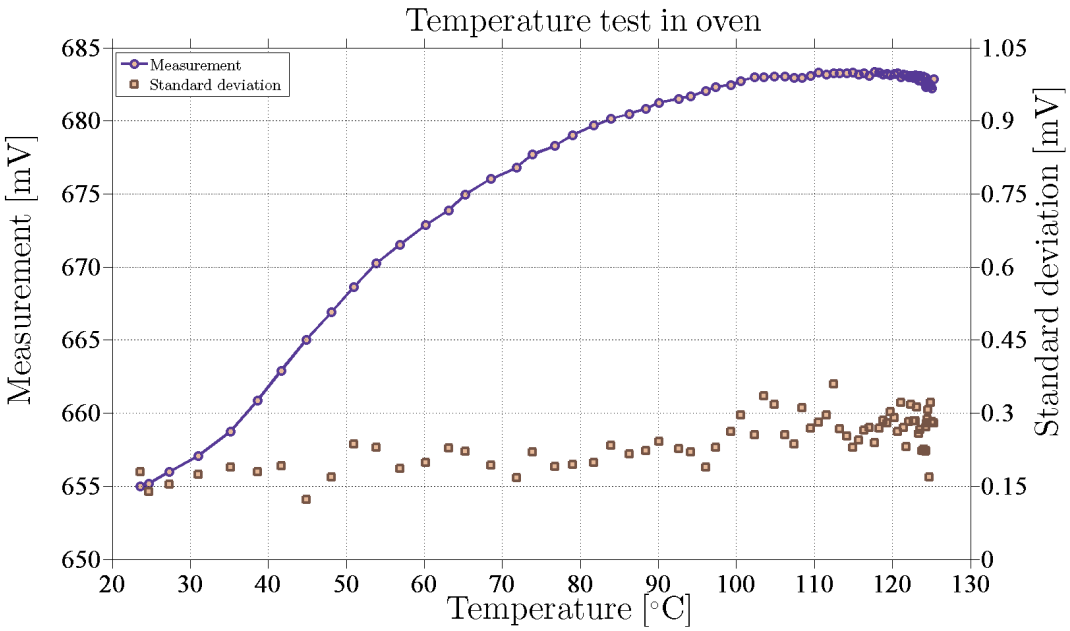

Figure 7.4: The figure shows the voltage measured by print number 2 as a function of temperature. The capacitance between print 2 and 4 was 2.2pF. The error bars show indicate 2 standard deviations at that temperature. The standard deviation is plotted according to the *y*-axis on the right.

The main purpose of the test was to prove that the circuits would not break down and a secondary goal was to investigate the effect of the temperature on the output of the

circuits.

The electronics where kept in the oven for 4 hours after the temperature reached 124°C. The output voltage changed slowly as the temperature rose, but the circuits were stable at the high temperature. It was also possible to restart the microcontroller, by cycling the power supply, at a temperature of 125°C. A high temperature environment is thus not a problem for the microcontroller or any other of the electronic components.

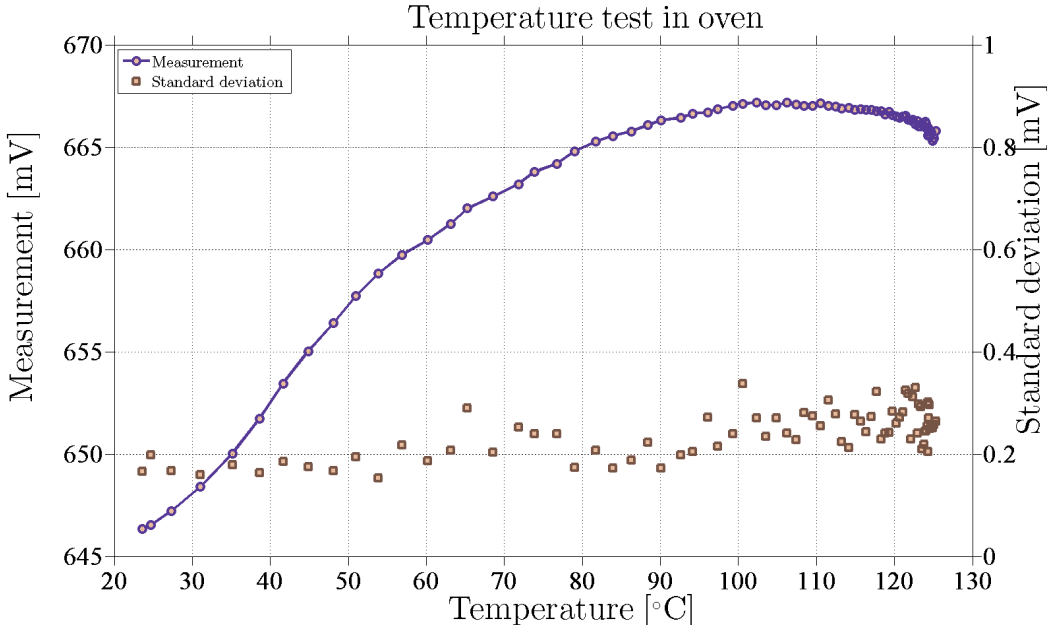

Figure 7.5: The figure shows the voltage measured by print number 4 as a function of temperature. The capacitance between print 2 and 4 was 2.2pF. The error bars show indicate 2 standard deviations at that temperature. The standard deviation is plotted according to the *y*-axis on the right.

The temperature affects both the mean and standard deviation of the measurements. The passive components in the electronics are affected and the timing of the square wave can also be affected. All this leads to changes in both the measured capacitance and the value of the actual capacitance between the electrodes. Temperature drift in the passive components are, to some extent, neutralized by the CT setup since the size of the stray capacitance in the two parts of the CT circuits will tend to change with similar magnitude. The capacitances which were mounted between the electrodes, were placed inside the oven with the electronics, so the nominal value of the capacitance between the electrodes was definitely changing as well.

The capacitance range between the two calibration capacitances has different magnitudes for the different channels (see section 7.2). The severity of the effect of temperature drift depends on the magnitude of the drift compared to the calibration range. For the electrode pairs which are placed furthest apart, the drift is comparable in magni-

tude to the calibration range, but it is uncertain if this would be the case if the measured capacitance was the real capacitance between two opposite electrodes and not the output caused by mounting a capacitor between two electrodes.

It is possible that the measurements could be compensated for the temperature drift. Each sensor would then need to be calibrated and a temperature sensor would need to be added to the design. This was not implemented in any of the three sensors though.

Capacitance resolution

In chapter 4 it was shown that the effective resolution of the tomogram depends on the capacitance resolution, so the resolution of the capacitance measurements is critical to the performance of the system. The resolution of the analog to digital conversion ($\frac{3.3V}{1024bit} = 3.2mV/b$ or 12fF/b) sets a lower bound for the resolution of a single sample, but if the amplitude of the noise is larger than the ADC resolution, an estimate of the mean of the distribution can be made with finer resolution than that of the ADC. An investigation of the signal to noise ratio of the measurements was carried out by performing a series of single sample measurements via the serial interface.

Figure 7.6 shows the distribution of 2048 samples performed on the eight different CT channels. The excitation frequency is 1.25MHz and the nominal value of the measured capacitance is 1.1pF. Most of the channels have a standard deviation close to 4.6mV and 2 channels have a standard deviation of a little less than 8mV. The bulk of the samples thus lie within an interval of $\pm$15mV of the mean value. For the least noisy channels, 99% of measurements will lie in that interval and for the 2 slightly noisier channels 95% will lie within 15mV of the mean. The capacitance-resolution, ρ_c, is now defined by that confidence interval.

$$\rho_c = \frac{2 \cdot 15mV}{4.4 \cdot 10k\Omega \cdot 1.25MHz \cdot 5V\sqrt{N}} = \frac{109fF}{\sqrt{N}}$$

where N is the number of samples and Δc is the resolution of the mean value of the samples. The resolution is thus definitely sub-pF which was a design goal for the circuits. If 128 ADC samples are used as the basis of each capacitance measurement, as in the following section, the capacitance-resolution is 10fF.

The speed of the ECT system is inversely proportional to the number of samples used for each measurement. Based on the desired frame rate of the system, the settling time of the circuits and the sampling rate of the ADC, the highest possible number of

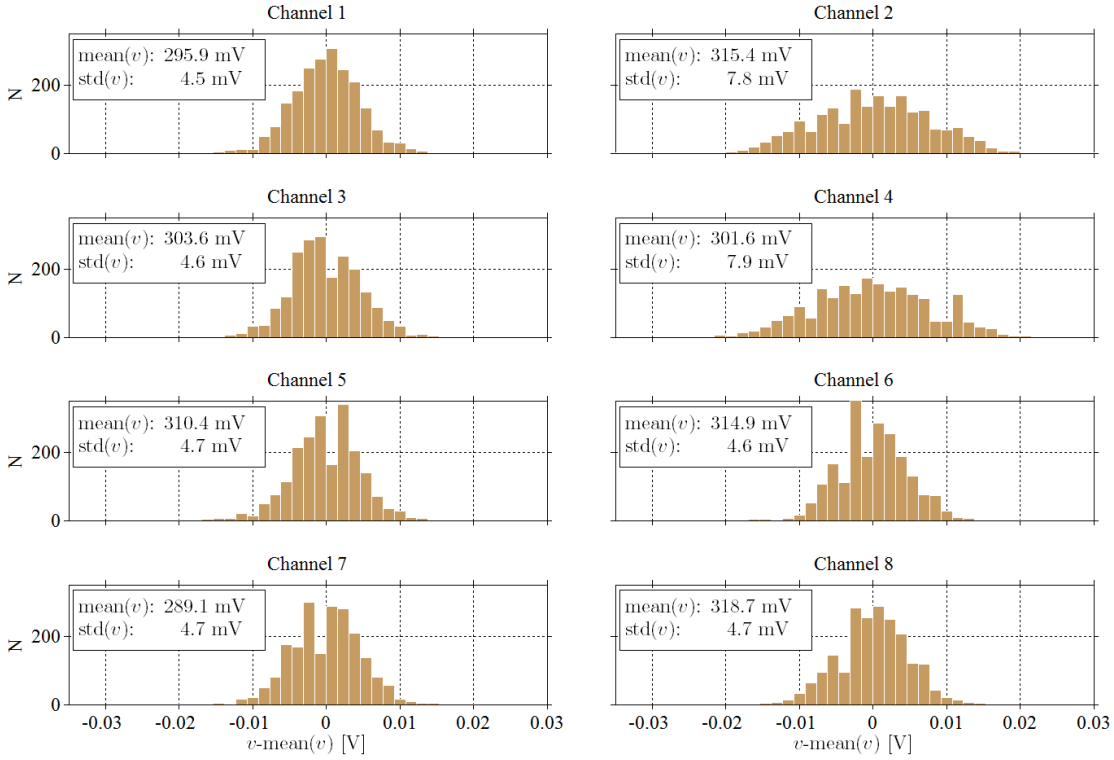

Figure 7.6: The histograms show the results of a series of test measurements. Each of the eight channels were tested as receiver. The estimate of the standard deviation of the channels is based on a set of 2048 samples. The histograms show the variation of the samples around the mean of the set. The mean values and standard deviations are shown in the text-boxes on each plot. The frequency was 1.25MHz and the nominal value of the measured capacitance was 1.1pF.

samples to take for every measurement can be calculated to:

$$N_s = (\frac{1}{28 f_F} - T_w) f_s \tag{7.2}$$

$$N_s = (3600\mu s - 1100\mu s) 238kHz = 618 \tag{7.3}$$

where, N_s is the number of samples, f_F is the desired frame rate, T_w is the settling time for the circuits and f_s is the sample rate of the ADC. The settling time is based on the analytical model of the circuit which predicts the settling time to be approximately 1ms.

The ADC is integrated in the microcontroller and uses Direct Memory Access (DMA) to transfer data to the memory of the microcontroller. The DMA can only access a sub-portion of RAM, which limits the number of samples which are available for each measurement to approximately 500. The number of samples was thus set to 500 which gives a capacitance-resolution of 4.9fF.

7.2 Calibration of sensor C

Proper calibration is a crucial factor in the production of tomograms of an acceptable quality. The calibration setup shown in section 6.4 was used to produce three sets of calibration capacitances for sensor C. Aluminum tubes with diameters of 96mm, 116mm and 126mm were used for the calibration with.

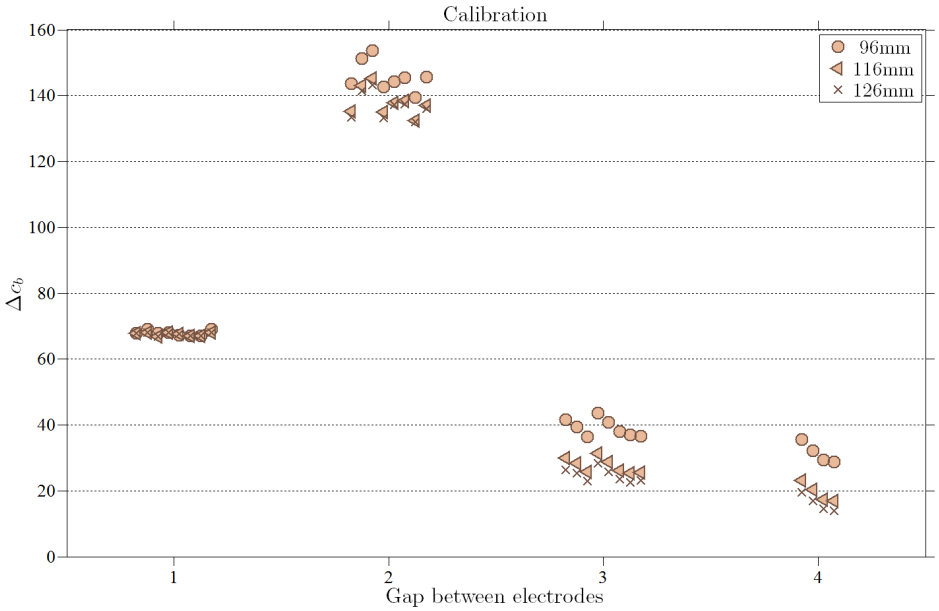

Figure 7.7: The figure shows a set of calibration measurements for sensor C. The markers show the change in the output bit-value between the high- and low capacitance sets. The bit-value for the capacitance change for adjacent electrodes (a gap of 1) is smaller than for electrodes with a gap of two, because it is measured through the unity gain buffer

Figure 7.7 shows the difference between the high- and low values for a set of capacitances for the third copy of sensor C. The values behave as expected. For each capacitance, the value increases as the diameter decreases. The output is passed through the unity gain buffer for adjacent electrodes and through the high gain buffer otherwise. It seems that the dynamic range of the ADC could be better utilized, maybe by the addition of the ability to change the offset for each channel in software, as described by Yang and York [41].

The quality of the calibration depends on the number of measurements on which it is based, since the estimate of the mean of course improves with the number of samples, but the position of the sensor inside the calibration-tube is much more important. The current calibration setup (see 6.4) works well for testing purposes, but something more precise than the foam-centralizer should be constructed for a more standardized

calibration setup.

7.3 Sensor A in test tank

Sensor A was tested in the test tank which was half filled with water. The sensor was centralized inside an aluminum tube which could be raised and lowered in the tank to move the air/water interface inside the reconstruction domain.

Tomograms produced by linear back-projection are presented in figure 7.8. The previously mentioned artifacts are present, but it is still possible to discern the distribution of water and air in the tomogram.

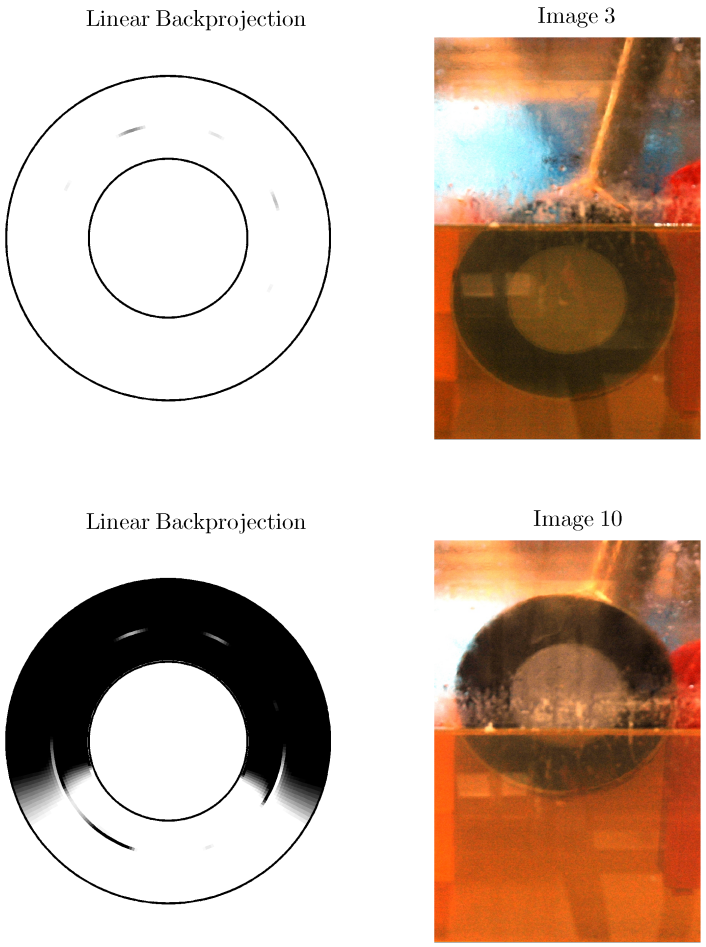

Figure 7.8: The figure shows a measurements in the test tank. The tomogram is on the left and the corresponding 'flow' is on the right. The tomograms were produced by linear backprojection. The circular artifact, caused by normalization of the pseudo-inverse, is clearly visible.

Figure 7.9 shows tomograms produced by smoothed Landweber with the LBP tomo-

grams as initial guess. The circular artifact is effectively removed by the smoothing and the horizontal interface between air and water is much better reproduced than with LBP.

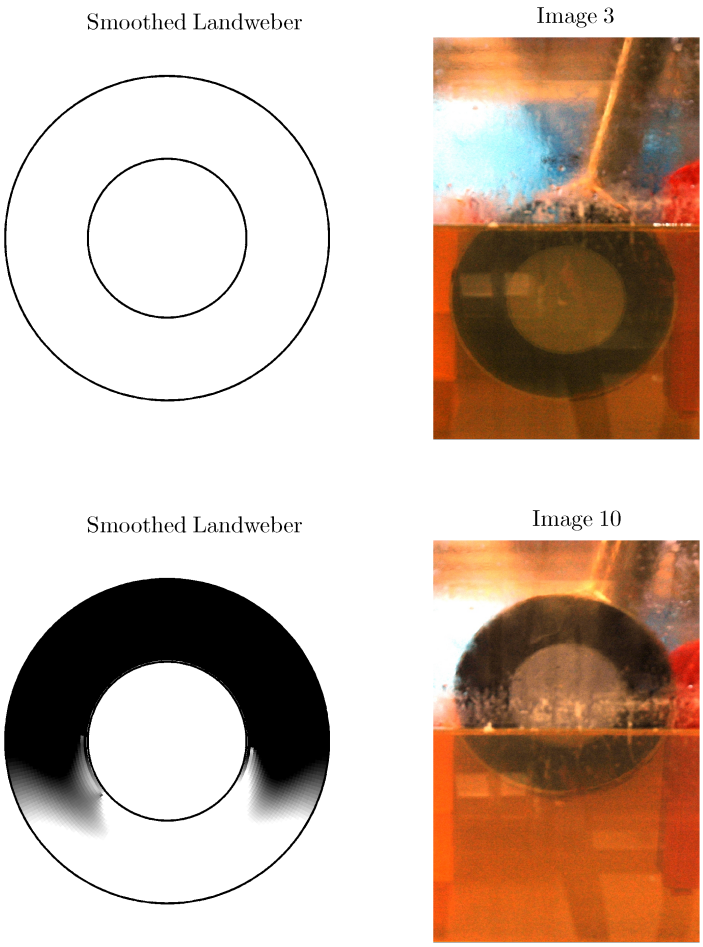

Figure 7.9: The figure shows a measurements in the test tank. The tomogram is on the left and the corresponding 'flow' is on the right. The tomograms were produced by smoothed Landweber.

Figure 7.10 shows a plot of the estimated watercut. The watercut has been estimated in three different ways. The 17 images were used to calculate an estimate of the watercut in the reconstruction domain and this is indicated by the 17 crosses on the plots. The calculation of watercut was based on measuring the water-level inside the annulus and then calculating the watercut numerically by

$$w_I = \frac{1}{A} \sum_{k:h_k<h_I} a_k \tag{7.4}$$

where A is the area of the annulus, $k : h_k < h_I$ is the indices k that correspond to a pixel lying below the waterline of the image, $h_k < h_I$, a_k is the area of the k'th pixel and w_I is the image based estimate of the watercut.

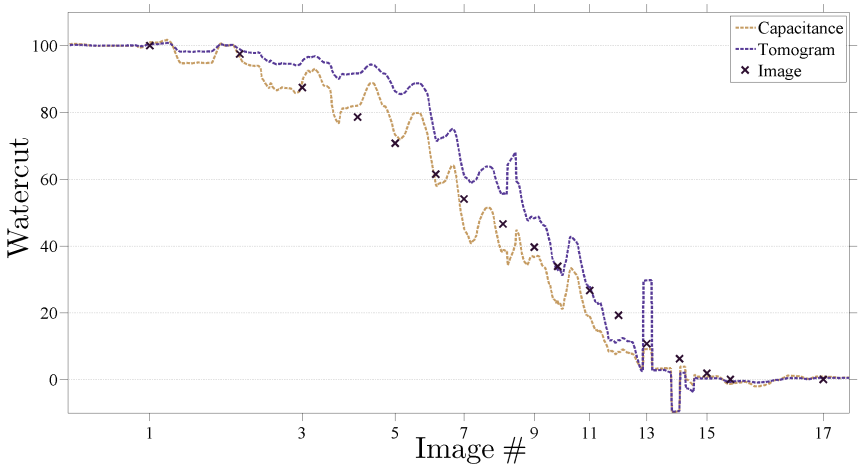

Figure 7.10: The figure shows the estimated watercut during the test. The watercut was estimated from the capacitance and the LBP tomogram for all frames and from the photo on 17 frames. The time when each of the 17 photos were taken are indicated on the x-axis.

The watercut was also estimated by a very rough method. Each capacitance has a value of 0 (1) for the low (high) calibration. An estimate of the watercut could then be the average of all the normalized capacitances. Monitoring the 1-norm of the capacitance vector thus might provide an indication of the watercut, w_c.

$$w_c = \frac{||\tilde{\boldsymbol{c}}||_1}{28} = \frac{1}{28}\sum_j \tilde{c}_j \tag{7.5}$$

where w_c is the capacitance based estimate of the watercut. This method works rather well for the data which are reported here, as well as in the article in section 8.4 and also in the results in appendix C, which are all from the same test. The results from the test loop, which are presented in section 7.4 also uses this method, but with less success. The reason for this is discussed later.

Finally the LBP tomogram was used to estimate the watercut.

$$w_t = \frac{\sum_k g_k a_k}{A} \tag{7.6}$$

where A is the area inside the annulus and g_k and a_k is the gray-level and area of the k'th pixel. The two watercut estimates are actually closely related. They are both weighted sums of the normalized capacitance vector, where all weights have the same value for w_c and the weights are largest for electrode-pairs that lie close to each other for w_t.

Both of the watercut estimates follow the estimation from the 17 images relatively well and especially the results from image 3 are noteworthy. The photo clearly shows that there is air inside the reconstruction domain but this barely registers on either of the

tomograms. The graph in figure 7.10 does indicate that the watercut is somewhere near 90-95% though which seems reasonable. The air in the reconstruction domain is thus measurable, but not reproduced on the tomograms. As was briefly discussed after the derivation of the resolution, measurable changes in capacitance do not necessarily produce noticable changes in the tomogram.

7.4 Sensor B in test loop

Sensor B was used in a system test performed in the test loop. A diagram of the test loop can be found in section 6.3. The cable which powers the tractor, is connected to a winch which is used to wind the cable out and pull the tractor out of the well. The winch is able to, relatively precisely, control the speed of the tractor when driving forwards by holding back on the cable. The winch also has a depth readout, which is accurate within approximately 1m and can be queried for data over a serial (RS-232) interface.

Data from the prototype sensor was sent over the wireline via a prototype of the COM module and used for live tomography on a PC. The depth reading from the winch was logged along with the capacitance data.

The sensitivity matrix was calculated with COMSOL based on the sensor geometry and the inner diameter of the test well. The calibration file was made based on data from the test tank.

Figure 7.11 shows the output from a few of the channels during the run. The upper plot shows channel 1, which is the normalized capacitance between electrode 1 and 2. The times where the sensor was in water or air are clearly identifiable from the single channel log. The bottom plot shows the normalized capacitance value for all the 8 channels that correspond to adjacent electrode-pairs. The eight electrode pairs change from a high to a low output at slightly different times because they are placed at different locations on the circumference of the sensor. Some of the normalized capacitances are negative between positions B and C. Normalized capacitances are forced to have a value of 0 (1) for the low (high) permittivity calibration distribution, but the value of $\tilde{\boldsymbol{c}}_i$ is not confined to the interval [0 1]. The sensitivity can have both positive and negative areas, which is what causes the problems with inside-out LBP normalization, and this is what causes the normalized capacitances to become negative. The water lies in areas which, for the negative normalized capacitances, are areas with mainly negative sensitivity.

It was attempted to run the tractor at a constant speed by holding back on the cable from the winch. The output is plotted as a function of time (sample number), but since the speed was constant, it corresponds to a position. It is thus a reasonable, but rough, approximation that the watercut at the position of the sensor is at 50% exactly halfway between when the first electrode-pair starts to change (position A on the plot) and when the last electrode-pair stops to change (position E on the plot). The watercut of

the frames in the chosen interval $[i_0, i_0 + \Delta i]$ is then estimated to be

$$w_F(i) = \frac{i - i_0}{\Delta i} 100\%$$

where i is the index of the frame, i_0 is the first index in the interval and Δi is the width of the interval.

Based on the approximation, the watercut is thus estimated to be 0% at position A, 25% at position B and so forth. The tomograms which were produced by the sensor at the five chosen positions are shown in figure 7.12 for positions A, B, C, D and E.

Three different reconstruction methods were applied to the capacitance data. Linear backprojection was used for the live imaging and the LBP tomograms are also reproduced here along with the results from smoothed Landweber and CGLS.

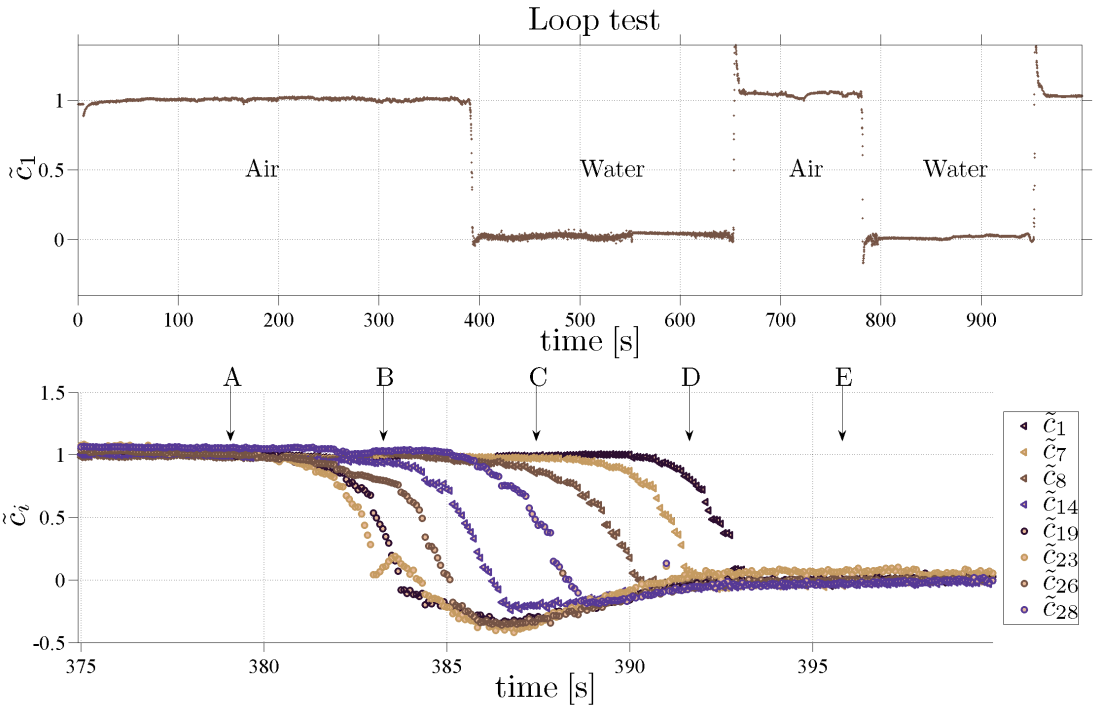

Figure 7.11: The two plots show raw capacitance data from a run with the prototype sensor in the test loop. The upper plot shows the normalized value of the capacitance between electrode 1 and 2. The sensor was driven through the section with water 2 times which is clearly visible on the plot. The lower plot shows a more detailed view of the first time the sensor is lowered into the water (compare indices with the upper plot). The plotted capacitances are the 8 capacitances between adjacent electrodes. Tomograms for positions A, B, C, D and E are shown in figure 7.12.

Initially, the calibration file was based on data from the test tank, but it turned out that better results were obtained by using the recorded data from the test loop for the

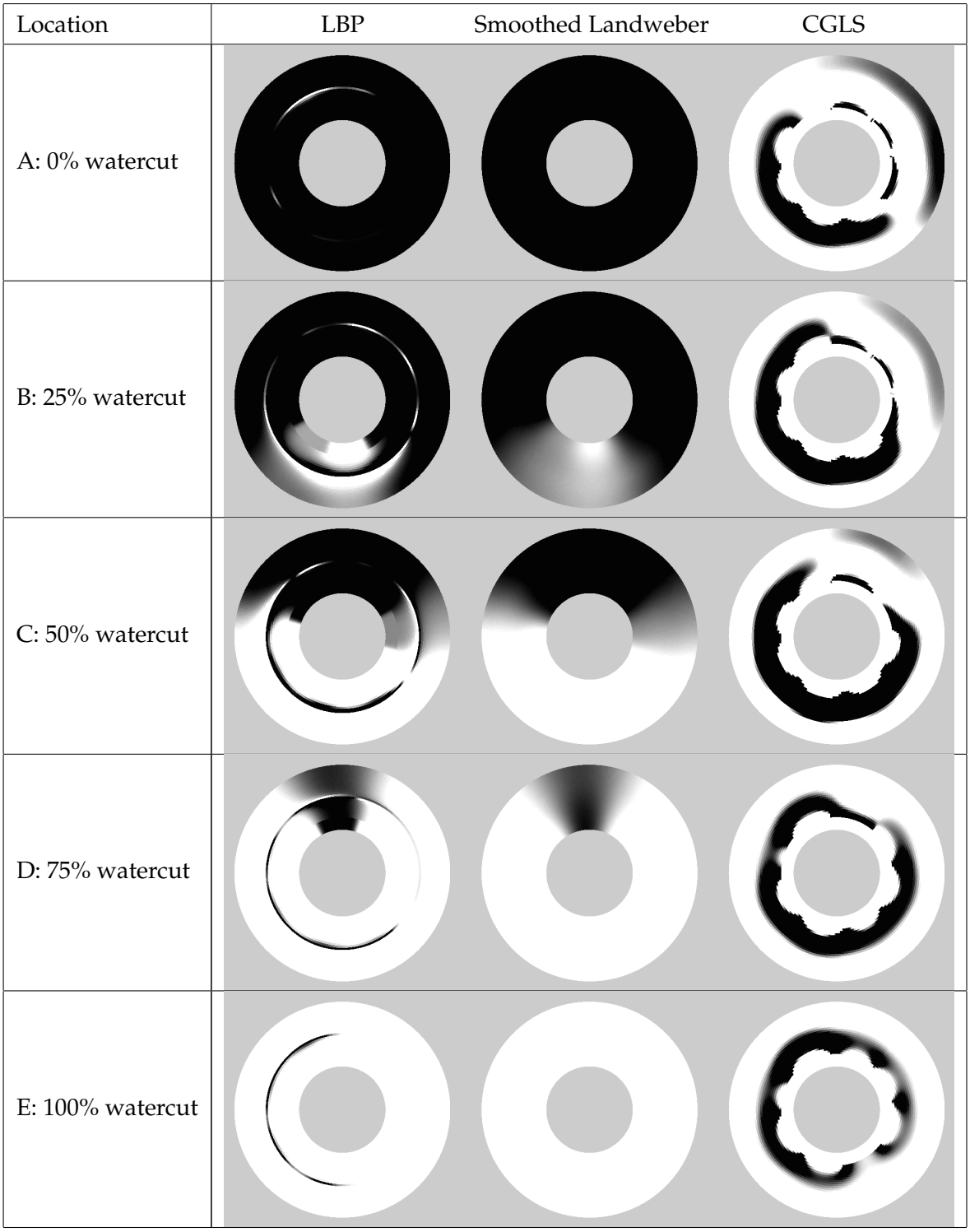

Figure 7.12: The plots show three tomograms at each of the positions from the plot in figure 7.11. The estimated watercut at each position is displayed to the right of the plots. The tomograms produced by linear backprojection are relatively accurate, but the artifact is very noticeable. The smoothed Landweber tomograms are based on the LBP tomogram as starting image. The artifact is removed by the smoothing operator and the quality of the produced tomograms is high. The CGLS algorithm is unable to produce tomograms which resemble the real distribution.

calibration. Calibration data was then obtained by letting the tractor remain static for longer periods in the water- and air filled sections.

During the live test, the backprojected images provided a clear indication of the watercut, despite the artifacts in the tomograms. The CGLS algorithm performed poorly on the experimental data, which is probably caused by a noise-level which is higher than in the numerical tests.

The smoothed Landweber algorithm performs very well on the data from the test. The watercut from the smoothed Landweber tomograms lie very close to the estimated values and the artifacts from the LBP tomogram have been removed. The reconstructed tomograms seem to recreate the permittivity distribution accurately and based on the tomograms it is possible to provide an estimate of the watercut, W:

$$\begin{aligned} w_t &= 1 - \frac{1}{\pi(r_c^2 - r_s^2)} \sum_i g_i r_i \Delta r \Delta\theta \\ &= 1 - \frac{2}{(r_c + r_s)(P - N_\theta)} \sum_i g_i r_i \end{aligned} \tag{7.7}$$

where r_c is the inner radius of the casing, r_s is the outer radius of the sensor, g_i and r_i is the gray-level and radial position of the i'th pixel, Δr and $\Delta\theta$ is the spacing between pixels in polar coordinates, P is the total number of pixels and N_θ is the number of pixels in the θ-direction. It would be reasonable to use thresholding on the tomogram, since it is a priori knowledge that the permittivity can only have one of two values, but the watercut was calculated directly from the raw normalized tomogram.

The watercut was also estimated by the direct method of (7.5).

$$w_c = \frac{||\tilde{\boldsymbol{c}}||_1}{28} = \frac{1}{28} \sum_j \tilde{c}_j \tag{7.8}$$

Figure 7.13 shows the calculated watercuts during the chosen transition from air to water. The watercut has been calculated from both the LBP tomogram, the smoothed Landweber tomogram and the capacitance vector.

There are a few outliers on the plot, but otherwise the estimated watercut seem to be rather accurate. The estimate from the capacitance vector fails to accurately indicate the watercut after the sensor is completely submerged though. The reason for this is that noise level on the least sensitive channels was high during the run.

If one investigates w_t for the linear backprojection, it turns out that the watercut from LBP and the direct capacitance estimate are very similar, so why does the capacitance method perform so much worse?

$$w_{t,LBP} = \frac{\boldsymbol{g}_k^T \boldsymbol{da}_k}{\boldsymbol{da_k}^T \boldsymbol{da}_k} \tag{7.9}$$

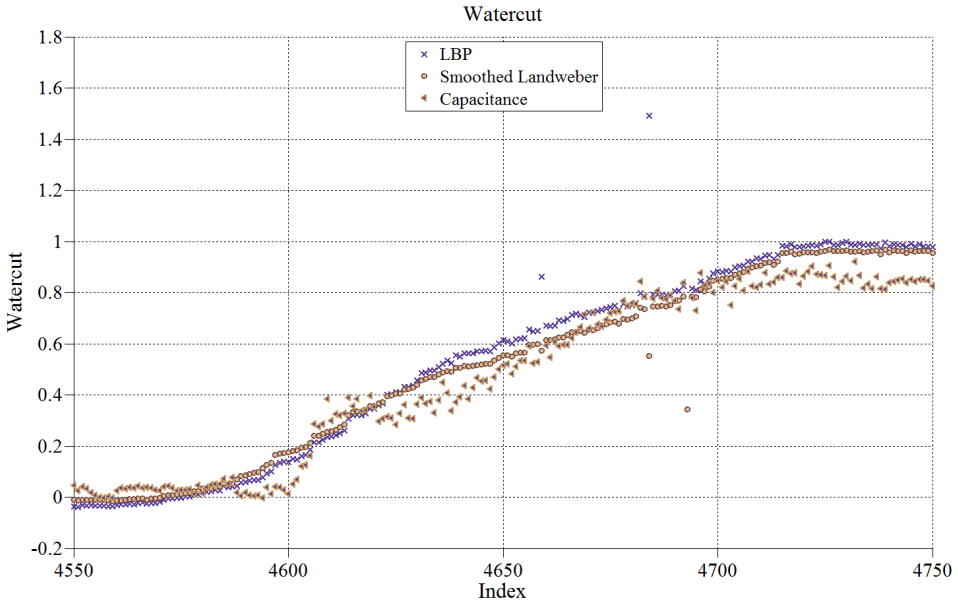

Figure 7.13: The figure shows the calculated watercut during the transition from air to water which is indicated in figure 7.11. Both the estimate from the LBP tomogram and the smoothed Landweber tomogram seem to provide accurate results, but the direct result from the capacitance vector is very inaccurate.

where $\boldsymbol{da}_k$ is a vector containing the areas of each pixel and the denominator of course evaluates to the area of the reconstruction domain, A. The gray-level vector is

$$\boldsymbol{g}_k = \boldsymbol{S}_{ki}^{\dagger}\tilde{\boldsymbol{c}}_i,$$

which is substituted into the expression for the watercut:

$$w_{t,LBP} = \frac{1}{A}\tilde{\boldsymbol{c}}_i^T(\boldsymbol{S}_{ki}^{\dagger})^T\boldsymbol{da}_k \tag{7.10}$$

$$= \frac{1}{A}\tilde{\boldsymbol{c}}^T\boldsymbol{v}_i \tag{7.11}$$

$$= \sum_i \tilde{c}_i w_i \tag{7.12}$$

The watercut estimate from the LBP tomogram is simply a weighted sum of the normalized capacitances. The reason it performs better than the direct normalized capacitance estimate is that the weights for the sensitive capacitances are higher and the estimate is thus less sensitive to the higher noise level.

The weights w_i are plotted in figure 7.14 which shows that the weight drops by approximately one order of magnitude for every time the distance between the electrodes is increased.

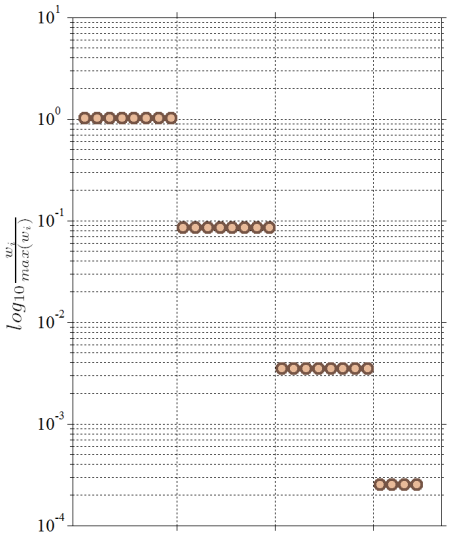

Figure 7.14: The figure shows the weights w_i from (7.12). The weights have been sorted such that the 8 first points correspond to the adjacent electrode-pairs and so forth.

The results of of the loop test are promising and demonstrate that sensor B is able to produce live tomograms and measure the watercut quite accurately in a simple layered flow. The comparison of the measured versus the actual watercut is based on some crude estimates though, so they can only be used as a qualitative indication of the effectiveness of the sensor. Reference measurements of the watercut with e.g. images from a camera inside the well would be beneficial to the test. The tomograms mainly come out as functions of the angle though and further work on the reconstruction technique seems to be necessary.

The well-fluid was tap water which was mixed with the rust and dirt inside the well. An important issue to investigate is the sensitivity of calibration measurements to differences between the well fluid and the fluid used for calibration. Certainly, it is not always possible to perform in-well calibration since that depends on finding locations in the well with purely high and low permittivity flow.

In preparation for a field test, sensor C was tested in the same way, but the results were merely used as a system test and rough calibration before the field test, so only the calibration results have been included here (see section 7.2).

Chapter 8

Conclusion

Electrical capacitance tomography was chosen as a well-logging solution among a list of several candidates. The principal reason that ECT was chosen, is the simplicity of the electronics. A simple and robust hardware design ensures that the sensor is able to endure the operating conditions inside an oil-well.

A new sensor geometry was proposed. The reconstruction domain for this inside-out geometry is an annulus. The cylinder inside the annulus is occupied by the sensor. The electrodes are thus placed inside of the reconstruction domain and the outer boundary (the casing of the well) is grounded. This design allows an inside-out sensor to move inside the outer cylinder and to supply tomograms of the flow between the sensor and the outer screen, at any position.

8.1 Reconstruction

An analytical expression for the sensitivity matrices of both the inside-out and the conventional geometry was derived. The analytical solution provides the means to calculate the sensitivity field quickly, independent of the spatial resolution, as a series expansion.

Numerical calculations of the sensitivity matrices for the inside-out geometry were performed by the finite elements method using COMSOL and in MATLAB using a custom-made finite difference algorithm.

Several reconstruction methods were investigated. Linear backprojection proved to be applicable for an inside-out geometry, as it is for the conventional geometry, but there are some issues with the inside-out geometry, which have a negative effect on the quality of the tomograms. The problem originates in the normalization employed when the

inverse problem is solved by linear backprojection. This causes linear backprojection to be less desirable for an inside-out geometry than for a regular geometry where the normalization does not cause these problems.

A customized version of Landweber optimization, smoothed Landweber, was developed and demonstrated to be able to remove resilient high-frequency components from the initial tomogram. In the case of inside-out ECT, this is desirable since a high frequency ring-shaped artifact is present in the LBP tomogram, which is used as a starting point for the Landweber iterations. Smoothed Landweber is an adaption of generalized Landweber, where a chosen operator is applied to the iterative solution after each iteration. In the case of smoothed Landweber, a smoothing operator is applied for a pre-defined subset of the iterations.

A frame rate of approximately 10Hz was achieved in tests of the inside-out system. Tomograms were produced by linear backprojection. Live tomography was not attempted with smoothed Landweber. Instead it was applied to pre-recorded data. The frame rate is limited mainly by the communication protocol and the reconstruction algorithm.

It is proposed to attempt live imaging with smoothed Landweber by implementing the algorithm in a micro-controller, DSP or FPGA. Since the developed software will also be used for off-line data visualization, it is also an option to use a reconstruction method which is too slow to use for live imaging. It would be acceptable to use even several hours on the rendering of off-line data.

Further investigation of inside-out reconstruction will be an important part of future work on the system. It is possible that improved performance for Landweber could be achieved by using the former tomogram (from the previously recorded capacitance vector) as an initial guess for the algorithm. Also, the Landweber algorithm which was implemented uses a fixed step length. It is very probable that an adaptive technique would provide much faster convergence.

The resolution of tomograms was discussed and a suggestion for a definition of the effective resolution of an ECT sensor was developed. It was shown that an approximate value, for the system which was developed in this project, is approximately 1% of the total area inside the reconstruction domain. The expression for the effective resolution could be a valuable design aid in finding a balance between sensor shape and circuit design.

8.2 Capacitance measurements

Three different inside-out sensors were constructed. Sensors A and B were based on the same electronic circuits (CT layout 1) and an improved circuit layout (CT layout 2) was produced for sensor C.

Version 2 of the CT layout was tested and the resolution of the capacitance measurements were shown to be 10fF (at 128 measurements) which was within the specifications.

Reconstruction would benefit from having a larger number of independent capacitance measurements as basis for the tomograms. This would be achieved by raising the number of electrodes in the sensor. The consequence of mounting more electrodes is that the inter-electrode capacitances and capacitance-changes grow smaller[1]. In order to raise the number of electrodes, it is thus necessary to improve the capacitance-resolution.

Alternatives to the CT technique[24–26, 41] have been shown to improve the resolution of the capacitance measurement. These techniques require more advanced and bulky hardware though. Since the circuits need to operate at a large range of temperatures, these other capacitance-to-voltage circuits need to be tested in high temperatures.

8.3 Tests

It has been shown that CT layout 2 is able to operate in well conditions. The temperature drift is substantial enough for the error to be larger than the standard deviation of a single ADC-sample. For the least sensitive channels, the deviation is close to 50% of the calibration interval and the temperature drift will thus noticably affect the resulting tomogram, if the calibration file was made at surface conditions.

Calibration results for sensor C were presented. It is shown that the capacitances depend on the well diameter as expected; the capacitance rises as the diameter grows smaller. Procedures for the calibration of sensors for a specific casing diameter were developed and also included in the software-interface (MATLAB) to the sensor.

Several reconstruction methods were used on data from the test-loop at Welltec and it was shown that smoothed Landweber was able to produce tomograms, which were very representative of the actual layered flow inside the test-loop. The location of water in the loop was clearly identifiable. Based on an assumption of constant velocity of the tractor, the water-cut, as the sensor traversed the air/water interface, was also very

[1] Unless the electrodes are made longer, which is undesirable.

close to the expected value.

It is proposed to construct a small flow loop as a testing facility. The casing of the flow loop would ideally be transparent such that images of the flow could easily be obtained from outside the loop. The entire casing or possibly just a section of it would need to be electrically conductive such that it could be grounded, which could be achieved by a conductive mesh. It should be possible to adjust the inclination of the part of the flow loop containing the sensor. By adjusting the inclination of the flow loop and the flow rate of water, oil and air it should be possible to create different kinds of flow, such as slow laminar flow, annular flow and slug flow.

Film buildup

It has been suggested to test the vulnerability of the sensor to the build-up of hydrocarbon-film on the non-conductive annulus that isolates the electrodes from the well. A well-known issue with capacitance based sensors is that the output is dominated by the permittivity in the near-field and that they are thus vulnerable to such film-buildup.

The tests in the test-loop gave no indications that this is the case for the inside-out sensor, but this needs to be tested much more extensively. It is possible that a special coating of the non-conductive sleeve would decrease the tendency for film to build up close to the electrodes, especially since the liquid in the well flows transversely to the surface of the sensor and thus provide a transverse shear on any film which has built up on the sensor.

Toolstring position

Sensor C has been designed to be placed at the very bottom of a toolstring, but there are applications where that is not desirable.

After an attempt to open or close valves inside the well, it would be very helpful to be able to confirm that the valve has been manipulated into the desired state. In some cases this could be achieved by observing the tomogram produced by ECT, since one of the consequences of the operation would be a large and very noticeable change in the flow regime.

To include the ECT sensor in such operations, it would need to be placed further up the toolstring. This, in turn, would require the sensor to have wires running through it (feed-throughs), so the tools that are placed further down the string are connected to power sources and to communications. The feed-through connections would most

probably cause a higher level of noise in the capacitance measurements, which would affect the capacitance resolution of the sensor. The effect of having feed-throughs inside the ECT sensor will need to be investigated, but otherwise there would not need to be any major changes made to the tool.

8.4 Further development

Based on the current features and performance of sensor C, some job scenarios have been suggested. Sensor C should be used in scenarios where the location of inflow or outflow spots in the well need to be identified. Examples of such jobs include leak detection and detection of cracks with high water inflow in limestone formations. It is possible that it should be investigated whether the inspection of raw data (capacitances) makes it possible to spot flow changes that are not clearly represented on the tomogram. A measurable change in capacitance will not necessarily show up on the tomogram, so to detect very small changes in the permittivity distribution it might be better to inspect the capacitance values directly.

An advantage of the proposed design is that the entire sensor is contained within a standard housing. The absence of mechanical parts which protrude into the flow means that the flow is disturbed less than with already existing systems and that the sensor is less vulnerable. I could be considered though to have electrodes mounted on spring bows, which can press them against the well casing. This would be very advantageous in the reconstruction.

M.R.Rzasa has reported results where ECT tomograms and tomograms produced by optical methods are combined[42]. Since a prototype of an optical sensor is being developed in another project, it would be to attempt combining the data from these two systems.

Measuring well flow rates is of great interest to oil field operators. The tomograms which are provided by the current version of the sensor are valuable in themselves, but if the capabilities of the sensor were expanded to include measurement of flow rates, the value of the logging data would be significantly increased.

To measure flow rates in the well, it is necessary to augment the measurements with a velocity measurement. Discussions of possible solutions to this points in the direction of an ultrasonic Doppler velocimetry. It has also been suggested to add another set of electrodes, such that two tomograms, obtained at two different positions, can be correlated [16, 17].

The most simple way to test velocity measurement by ultrasonic Doppler velocimetry, would be to measure the Doppler response along a single line, placed through the middle of the well. Flow rates for the entire cross-section would then be calculated based on e.g. a fit of the measured velocities to an analytic expression for the velocity distribution inside a cylinder. Ultrasonic speckle velocimetry, which was one of the top-scoring suggestions in the initial method-selection, could also be attempted, which would make it possible to measure the velocity over an entire cross-section and thus not depend upon assumptions/models of the velocity distribution.

Publications

IST paper

The following conference paper[43] describes the construction of a simple 6 channel (conventional geometry) ECT system which uses charge transfer circuits to measure capacitance and LabVIEW[44] to control the circuits.

The paper was submitted to the IEEE International Workshop on Imaging Systems and Techniques on Crete in 2008.

A Compact Electrical Capacitance Tomography System

J. Kjærsgaard-Rasmussen
Department of Mechanical Engineering,
Technical University of Denmark,
Copenhagen, Denmark
Email: jimmy.kjaersgaard@gmail.com

W. Q. Yang
School of Electrical and Electronic Engineering,
The University of Manchester,
Sackville Street, Manchester M60 1QD, UK

***Abstract*—Most existing electrical capacitance tomography (ECT) systems are designed using a 19" Eurocase and they are relatively expensive. To reduce the size and cost, a compact ECT system has been developed. It is based on a charge/discharge capacitance measuring circuit and a USB data acquisition (DAQ) unit from NI. It has 6 measurement channels and is housed in a box measuring 158×80×96 mm. The system hardware is operated by a laptop via a USB port.**

The software is written in LabVIEW and the image reconstruction software in MATLAB. This paper presents the hardware design for the compact ECT system, the calibration procedure, and the image reconstruction from capacitance measurements. The performance of the system has been evaluated and the measurement results are presented. It is concluded that the compact ECT system is capable of providing small capacitance measurements and generating tomograms. The signal-to-noise ratio (SNR) of the measurement system is acceptable and can be improved further.

Keywords: Capacitance measurement, Data acquisition, LabVIEW, MATLAB, Tomography

I. Introduction

ECT has been applied in various situations where it is desirable to measure the permittivity distribution in a cross section, e.g. to image a multi-phase or multi-component flow. The existing ECT systems are designed using one of three types of measurement circuits/instruments: (1) the charge/discharge circuit, (2) the AC circuit with high frequency sine-wave excitation and phase-sensitive demodulation and (3) impedance analyser. With the first two circuits, the hardware of almost all systems is housed in a 19" Eurocase. An impedance-analyser-based system is even larger. Existing ECT systems are thus large in size. Also, they are expensive. Therefore, some researchers are limited to carrying out ECT-research by software simulation.

The intention of the work reported in this paper is to develop a low-cost, compact ECT system.

II. System design

The hardware of the system consists of the capacitance measurement circuits, hardware interfaces between measurement circuits and a calibration switch. The software consists of control software for the DAQ and a program for image reconstruction. Every software part is put together in a graphical interface.

A. Charge Transfer Circuit

A charge/discharge circuit has been used to measure the small inter-electrode capacitance of an ECT sensor. A thorough description of the charge transfer technique was given in [2]. By applying a square-wave excitation signal to one side of a capacitor, charge is transferred back and forth between two electrodes.

When the voltage steps from low to high, the charge flows one way and when the voltage steps down again, the charge flows back. By only measuring every second step, the measured current will flow in the same direction every time. The charge transfer current of e.g. the positive voltage step is converted to a voltage through the op-amp.

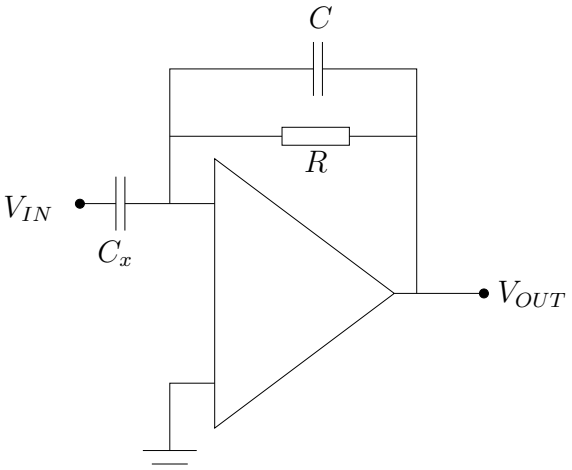

Fig. 1. The figure shows a diagram of a circuit that can measure the value of a capacitance. V_{IN} is a square wave of frequency f and with amplitude V_c. The amplitude of the output voltage is linearly dependent on the capacitance C_x.

The op-amp configuration is shown in Fig. 1. A charge transfer circuit gives an output that is linearly dependent on the unknown capacitance. That is

$$C_x = \frac{V_{out} - V_{injection}}{fRV_c}, \tag{1}$$

where C_x is the unknown capacitance, V_{out} is the measured voltage, $V_{injection}$ is the voltage caused by charge injection,

f is the frequency of the square wave, R is the value of a feedback resistor used with the op-amp and V_c is the amplitude of the square wave.

With a differential configuration, two op-amps are connected to each electrode. One op-amp converts the charge current and the other converts the discharge current. The difference between the two outputs is amplified. This signal is subsequently filtered by a second order, low pass, Butterworth filter. The output from the filter is converted to a 12 bit digital value in the DAQ unit.

The low-cost compact ECT system hardware contains six channels of charge/discharge measuring circuits, which are placed on a single printed circuit board (PCB), 119×75 mm, with all surface-mounted components. The channels are labeled from A to F. The PCB is shown in Fig. 2. The same kind of op-amp is used for the charge transfer circuits and for the filters. We used AD8672 op-amps and 74HC4066 switches. The 6 channels were operated in parallel to, at a later stage of development, achieve a desired data acquisition rate.

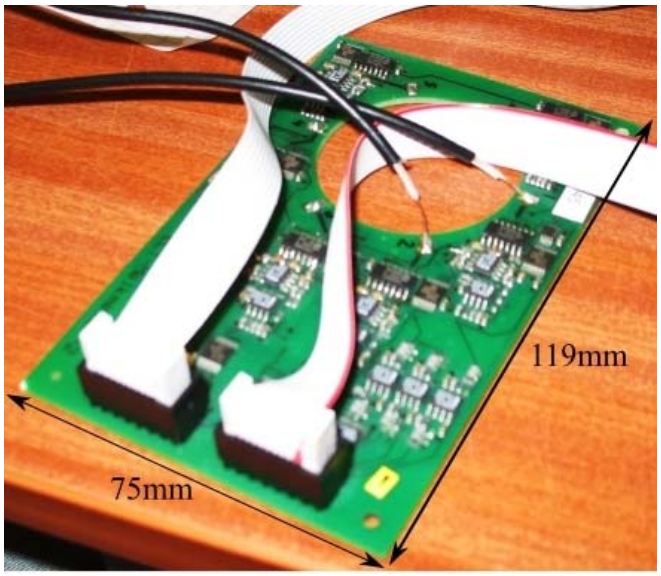

Fig. 2. A picture of the PCB. The ribbon cable on the right is the power supply and the other cable is for data transfer. Two electrodes are connected to the board via BNC cables. The hole in the PCB is made so the board can be mounted around a tube.

B. Other System Hardware

An external oscillator, 12 MHz IQXO, is used to generate the square-wave used in the charge transfer circuits. The signal from the crystal is split into four 3 MHz signals by two D flip-flops. The n'th signal is phase-shifted with $\frac{(n-1)\pi}{2}$ with respect to the original signal. The four square waves open and close the switches on each side of the measured capacitance and thus control the charge/discharge processes.

The PCB is controlled by a PC, via an NI USB-6008 DAQ unit, using LabVIEW. The DAQ has a resolution of 12 bit between ±10 V. A schematic overview of the hardware components is shown in Fig. 3.

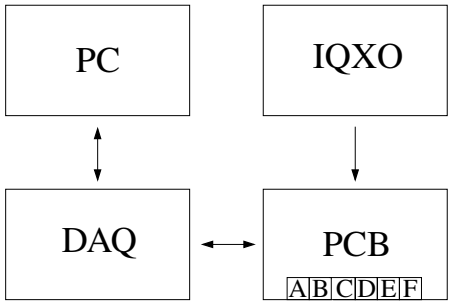

Fig. 3. The figure shows a diagram of the system. The DAQ is controlled by the PC. The PCB receives a clock signal from a 12MHz IQXO crystal and is controlled by the DAQ. The PCB has six channels, A-F. Each channel can connect to an electrode in an ECT sensor.

The LabVIEW program has a MATLAB node, which calculates and plots the resulting image.

C. Calibration

Initially, the PCB design allows calibration for charge injection [3] of the switches to be performed on only one channel. The value from channel A would then be used to calibrate all channels. The problem with this is that charge injection on different channels does not have the same value. Therefore, it was necessary to modify the PCB to allow calibration for charge injection on each individual channel. This was done by adding a switch that can set the amplitude of the square-wave, either to V_c or 0 V. By this arrangement, all the channels can be calibrated.

Setting V_c to zero in 1 gives the following:

$$V_c = 0 \quad \Rightarrow \quad V_{out} = V_{injection}. \tag{2}$$

So, by flipping the calibration switch and measuring the output of the 6 channels, the charge injection of all 15 measurements in a capacitance set is known. The calibration data can then be used to compensate each channel for its actual injection current.

It is common practice to normalise the capacitance measurements. To implement normalisation, two sets of capacitances must be measured. One set is measured with a higher homogenous permittivity distribution inside an ECT sensor and the other set is measured with a lower permittivity distribution (usually air). During operation, a set of measured capacitances can then be normalised by

$$\tilde{c} = \frac{c_m - c_-}{c_+ - c_-}, \tag{3}$$

where c_- is the set of capacitances measured with a lower permittivity distribution, c_+ is the set of capacitances measured with a higher permittivity distribution and c_m is the measured set of capacitances that needs to be normalised. With normalisation, it is assumed that the relationship between capacitance and permittivity in the defined range is linear although this is not absolutely true. Since the normalisation procedure calibrates for any linear deviation, the ability to calibrate for charge injection alone is actually unnecessary if only normalised capacitance is used.

D. Software

Software has been developed and the program was written in LabVIEW. In this part, only the important functionalities are discussed. Basically, all the Virtual Instrument (VI) does is to operate the PCB through the DAQ and then to write the measured data to the harddisk. A few different modes are incorporated, e.g. calibration can be done by pressing a virtual button on the VI interface. The most prominent part of the interface is for real-time image reconstruction. This will be discussed next.

The data flow for the creation of a single tomogram is shown in Fig. 4. First, two electrodes are selected for a measurement. The measurement is then made and the data saved. This is repeated for all electrode combinations and finally a tomogram is created. The communication with the DAQ through LabVIEW is the bottleneck in the loop. The construction of a single tomogram is completed in approximately 1 s.

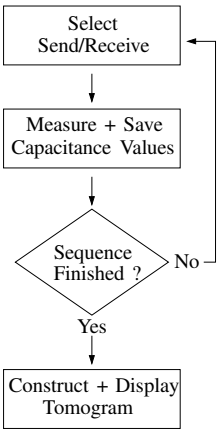

Fig. 4. The figure shows a flow-diagram of the major parts of the software. After setting one electrode to send and another to receive, the multiplexer is set to connect the receiving channel to the output of the PCB. The program then measures the output voltage via the USB DAQ. This is repeated for all unique electrode combinations and the value of every output voltage is saved in a vector in LabVIEW. With a full capacitance vector, a MATLAB script is executed. The script uses the capacitance vector and the sensitivity matrix to generate a tomogram. The tomogram is made by linear back projection.

E. Image Reconstruction

Image reconstruction for ECT is presented in [1] and [4]. It is a severely under-determined problem. With a relatively small number of measurements (15 measurements in our case), an image with say 4096 pixel values (a 64×64 bit image) may be constructed. This is possible because an extra set of information (equations) is added to the problem. By simulations, a matrix, S, that has the following property

$$c = S\epsilon, \tag{4}$$

can be constructed. The column vector c contains the 15 capacitance values. The sensitivity matrix S contains information about the spatial sensitivity of the sensor. In the sensitivity matrix, one datum, at one particular point in space, describes the change in capacitance caused by a localised change in permittivity. An entire map then describes which sections in space cause changes in which capacitance. The ϵ matrix is the permittivity distribution. In our case, the elements of ϵ represent pixels of an image.

The S matrix can be interpreted as a response to small perturbations in ϵ. Imagine ϵ to be uniform and then add a perturbation. In this case the perturbation, $\delta\epsilon$, is a Kronecker delta function.

$$\begin{aligned} c + \delta c &= S(\epsilon + \delta\epsilon) \\ \delta c &= S\delta\epsilon \end{aligned} \tag{5}$$

If the Kronecker delta function is centered at the i'th pixel, the i'th column of S is equal to the changes in capacitance. In this manner it is possible to construct S, column by column, by simulating capacitance changes.

The next problem is the inverse of the above. The capacitance set is measured and the permittivity distribution must be deduced. Since S is far from being a square matrix, it is impossible to find the inverse and an approximation must be made.

The simplest image reconstruction algorithm is linear back-projection (LBP). It is a surprisingly effective technique that solves the inverse problem in the following way.

$$\epsilon = \frac{S^T}{S^T S} c \tag{6}$$

The image constructed by LBP is blurred and only qualitatively represents the actual permittivity distribution. Typically, the provided tomogram is the starting point for a more advanced reconstruction technique.

Sensitivity maps for this 6-electrode ECT sensor have been generated based on simulation of the electric field between electrode pairs. The electric fields were calculated using COMSOL.

III. Prototype and Results

A. Constructed Hardware

For test purposes, a 6-electrode ECT sensor has been constructed. The sensor frame is a plastic tube. It is 44 cm long and 34.5 mm in outer diameter. On one half of the tube, as shown in Fig. 5(b), the 6 electrodes are mounted directly on the outside of the tube. The electrodes are made from adhesive copper foil. Each electrode is 50 mm long and 36 mm wide with a 1.5 mm gap between two adjacent electrodes. The electrodes are shielded by copper sheet all around the tube, above and below the electrodes in the axial direction. On the outside they are shielded by a copper screen. To avoid accumulation of a static charge, each electrode is connected to ground through a 1 MΩ resistor. The sensor is half filled with plastic beads.

During calibration the sensor is held vertically to produce a homogenous higher permittivity distribution inside the electrodes and likewise a homogenous lower permittivity distribution. Since the electrodes are placed at one end of the sensor, the section inside the electrodes will either be fully occupied by air or plastic beads.

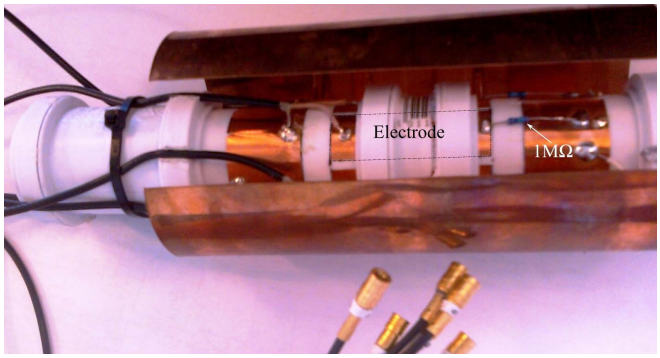

(a) The inside of the copper screen. Six electrodes are placed around the tube and grounded screens are placed on both sides of the electrodes. The screen of the PCB cables are connected to the ground screens on one side. Both screens are connected to the outer copper screen.

(b) The screen of each cable is connected to the outer copper screen. The inner conductor of the cables is connected to one of the six electrodes. The electrodes are mounted on the outside of the plastic tube, inside the copper screen. The three black strips are just to fasten the screen to the tube.

Fig. 5. The pictures show the inside and outside of the ECT sensor.

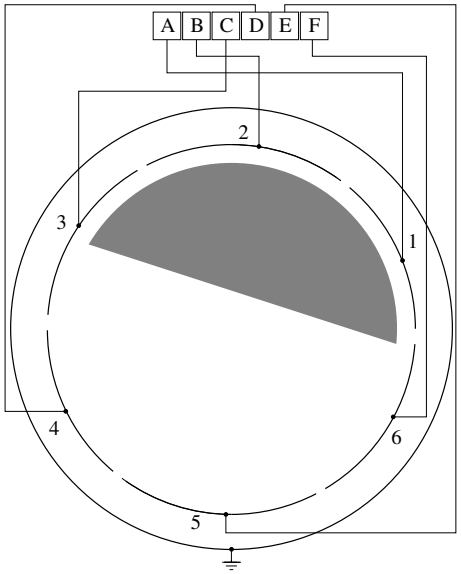

Fig. 6. The diagram shows the channels on the PCB and the sensor with a representation of a permittivity distribution inside. The channels on the PCB are labeled from A to F. The electrodes are numbered from 1 to 6 and are surrounded by a grounded screen.

TABLE I

THE TABLE SHOWS THE CONNECTION BETWEEN ELECTRODE PAIRS (MEASUREMENT NUMBER) AND THE ACTUAL ELECTRODES INVOLVED IN THE MEASUREMENT. IF THE ELECTRODES INVOLVED ARE $i - j$, THEN ELECTRODE i WILL BE THE ACTIVE ELECTRODE AND ELECTRODE j WILL BE THE MEASURING ELECTRODE ON WHICH THE CHARGE TRANSFER IS MEASURED.

Pair	Electrodes	Pair	Electrodes
1	1-2	9	2-6
2	1-3	10	3-4
3	1-4	11	3-5
4	1-5	12	3-6
5	1-6	13	4-5
6	2-3	14	4-6
7	2-4	15	5-6
8	2-5		

B. Tomograms and Calibration

A few tests were performed. First calibration for charge injection was performed. As previously mentioned, the calibration for charge injection is not really necessary, but it is useful to see if the original layout with only one channel is able to measure the charge injection. It turned out that the value of the charge injection on each channel is very constant, but it is different from one channel to another.

Fig. 8 shows a full capacitance set with the test sensor. If the test sensor had been perfectly constructed with identical electrodes placed in circular symmetry, each datum would be one of three different values. There were 15 different values though: 6 high values, 6 medium values and three low values. It is evident that the construction is not perfect. While the capacitances show more than three different values, they do present three different levels, where the lower level values are measurements 3, 8 and 12.

The relationship between the measuring sequence and the electrodes that were used in the measurement is shown in table I. Capacitance number 6 is measured with electrode 2 as the emitter and then measuring on electrode 3.

The channels on the PCB were investigated further by measuring only the six high capacitances, but with the six different channels for each capacitance. That gives 36 different measurements. The measurements are shown in Fig. 7. For each pair of neighbor electrodes (neighbor electrodes have the highest capacitance), a set of 6 measurements are plotted.

Fig. 7 shows systematic deviation in the capacitance value measured with each channel on the board. With the 6 channels, A-F, the 6 electrode combinations that give the highest capacitance values were measured. From the results, it can be seen that firstly, the capacitance between the 6 pairs of neighbour electrodes have rather different values. It seems that electrode 4 has been placed closer to electrode 5 than to electrode 3. Secondly, there is a systematic deviation in the way a channel measures a capacitance. Each electrode pair has been measured by all 6 channels. The results are plotted in the same order for each pair, and with the same colour. Channels A, E and F tend to measure higher values than the other three.

Fig. 8 shows 15 capacitance measurements taken when the sensor was filled completely by plastic beads. The 6 higher capacitance measurements should ideally have the same value. The difference comes both from the electrodes not being placed perfectly symmetrically and from the difference in gain of the measurement channels.

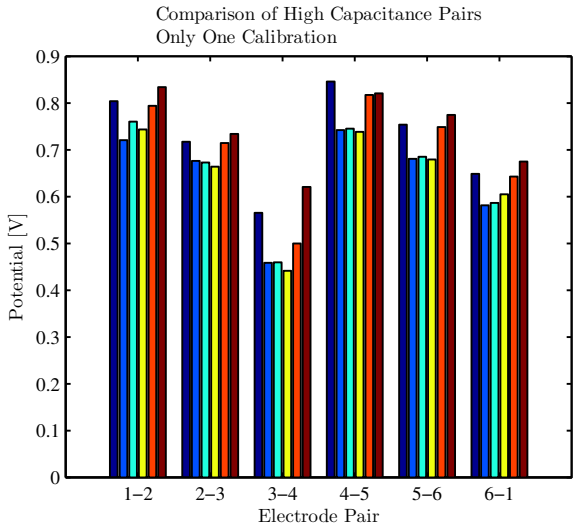

Fig. 7. The plot shows measurements of the six highest capacitance values. Each capacitance was measured with each channel on the PCB. For each electrode-pair, $i-j$, the six measurements are shown in the same order with different colors. The first bar is channel A, the second is B and so forth.

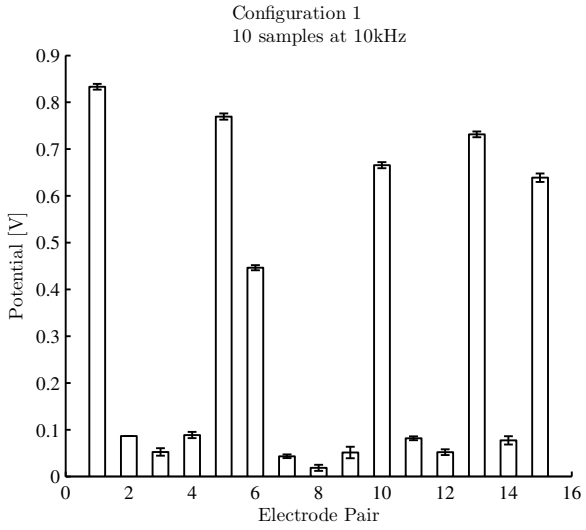

Fig. 8. The plot shows a capacitance set from the calibration in high permittivity. Actually the values plotted are voltages, not capacitances. The values are meaned over ten samples taken at 10 kHz. The standard deviation is not dependent on the capacitance value so the signal to noise ratio (SNR) is lowest for small capacitances. The standard deviation, the errorbars indicate ± 5 standard deviations, is approximately 1.5 mV. The SNR for the small capacitances is 20 dB.

An image was generated from 15 normalised capacitances measured at 10 kHz and then averaged over 10 samples. For simple evaluation, the LBP algorithm is used for image construction as the objective of this work is to prove the PCB and system design. More advanced image reconstruction techniques may be applied in the future. The permittivity distribution in the tomogram shows that the problem is ill-posed. The distribution (see Fig. 9) is smeared out and the interface between air and plastic beads is not as straight as could be expected.

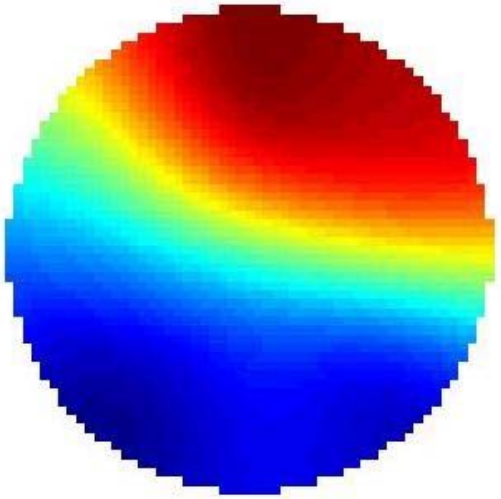

Fig. 9. An image of the projected permittivity distribution. The image was made by connecting the PCB to the test sensor and laying the sensor on the table. The beads in the tube then slide to the bottom and create the distribution shown on the tomogram. The blue color indicates a low permittivity and the red color indicates a high permittivity. The distribution shown on the image thus indicates that the plastic beads are gathered at one side of the sensor (in this case, the bottom of the tube.)

It would be useful to present a quantitative evaluation and of the accuracy of the tomogram. However, the actual permittivity distribution cannot be seen, since the tube is opaque. Qualitatively, the distribution is correct. If the tube is rotated along its axis on its side, the distribution will rotate on the screen. If one of the calibration situations are established, the plot will show a homogenous higher or lower distribution.

IV. Discussion and Conclusion

One error source in the charge transfer circuits is the charge injection caused by coupling capacitances in the CMOS switches. As expected, the charge injection current from the switches is very stable or constant for a specific channel. On channel B, for example, a value of 200 mV with a standard deviation of 20 mV was measured from one calibration to the next. On channel C the value was -70 mV with the same standard deviation. This shows that the calibration value on channel i cannot be used for channel j.

The SNR of capacitance measurements is 20 dB, but for the calibration it is as low as 10 dB. This is probably because the samples used for estimating the SNR of the capacitance measurements was taken without touching the sensor and at 1 kHz. The calibration data is taken a lot slower and the sensor is handled between each measurement. Both results are important. If a sensor is mounted, it will have a SNR of 20 dB between calibrations, but it will be sensitive to buildup of static charges.

It is evident that correction for a constant offset, on the measurement channels of the PCB, is not enough. There is

a systematic error on each channel, possibly due to different gains, deviation in component values and electrode placement. This is not a problem because the capacitance values used for image reconstruction are normalised by the two extreme data sets, which are measured when the sensor is filled with lower and higher permittivity materials, respectively. The procedure of charge injection compensation is actually not necessary for image reconstruction since deviations in gain and offset can be eliminated by normalisation.

A capacitance set contains 15 values and the image has 4096 pixels. Therefore, 61440 multiplications are needed to create an image. In principle, it should not be a problem to display e.g. 50 frames per second since it requires only slightly more than 3 million multiplications per second. The actual frame rate is less than one image per second.

In the future, circuits can be added to the PCB to facilitate calibration of each channel for charge injection. If charge injection is constant for each channel, charge injection compensation is actually already implemented by normalisation. On a system where the charge injection is expected to change between calibrations, the ability to perform quick calibration for charge injection could be an advantage. Another way to perform calibration is to set the excitation voltage to 0 so that no extra circuits are needed on the PCB.

The cost of the system is low and the size is small. A more compact design can easily be achieved. By means of the sensitivity map generated using COMSOL, 15 capacitance measurements were used to generate an image representing the permittivity distribution. The system works as expected and is able to produce a qualitatively correct tomogram of the distribution inside the constructed test sensor. The results presented in this paper serve as a proof of concept for the system.

REFERENCES

[1] W. Fang, "Reconstruction of permittivity profile from boundary capacitance data," *Appl. Math. and Computation,* vol.177, pp.178-188, 2006.

[2] W. Q. Yang, "Hardware design of electrical capacitance tomography systems," *Meas. Sci. Technol.,* vol.7, pp.225-232, 1996.

[3] G. Wegmann and A. Vittoz and A. Rahali, "Charge Injection in Analog MOS Switches," *IEEE J. Solid-State Circuits,* Vol. SC-22,No. 6, Dec. 1987

[4] Y. S. Kim, S. H. Lee, U. Z. Ijaz, K. Y. Kim and B. Y. Choi, "Sensitivity map generation in electrical capacitance tomography using mixed normalization models," *Meas. Sci. Technol. ,* Vol. 18, pp.20922102, 2007

Article

The following article concerns the design and testing of sensor A and presents the new inside-out geometry. The reconstruction of inside-out tomograms is discussed and the circular artifact is treated. The smoothed Landweber approach and the developed approach to defining an effective spatial resolution of an ECT sensor is proposed.

The article has not yet been sent in for review but has been written with the intention of submitting to Flow Measurement and Instrumentation.

Inside-out electrical capacitance tomography

J.Kjærsgaard-Rasmussen[a,*], K.E.Meyer[a]

[a] *Fluid Mechanics Section, Department of Mechanical Engineering, Technical University of Denmark*

Abstract

In this work we demonstrate the construction of an 'inside-out' sensor geometry for electrical capacitance tomography (ECT). The inside-out geometry has the electrodes placed around a tube, as usual, but measuring 'outwards'. The flow between the electrodes and an outer tube is reconstructed; allowing the inside-out sensor to move inside the outer tube. A test sensor was constructed and capacitances were measured using the charge transfer technique. Sensitivity matrices for the inside-out sensor were calculated with a finite elements approach and some special issues with the sensitivity matrices are discussed. An adaption of the Landweber algorithm which works very well for the new geometry is presented and a definition of the spatial resolution of an ECT sensor is suggested. Tomograms from a test run of an inside-out sensor are presented and measurements of watercut are compared with images obtained by a camera and a simple direct result based on the capacitance vector.

1. Introduction

Electrical capacitance tomography (ECT) is a measurement technique which uses capacitance measurements to produce tomograms of permittivity distributions [1]. The capacitances are measured between electrodes at the boundary of the reconstruction domain. Traditionally, the domain of reconstruction is a disc with the electrodes placed at the outer boundary. Other, simply connected, domains like cylinders [2, 3], squares [4] and cubes [5] have been investigated as well.

The most common implementation of ECT has 6-12 electrodes placed along the circumference of a non-conductive tube. The inter-electrode capacitances are then used to construct a cross-sectional image of the permittivity distribution inside the tube. The reconstruction of the permittivity distribution is a discrete inverse problem based on a linearization of the forward ECT problem; calculating a set of capacitances from a known permittivity distribution. This discretized linearization is stated in equation 1.

$$\delta \boldsymbol{c} = \boldsymbol{S}\delta\boldsymbol{\varepsilon} \tag{1}$$

The elements of vector $\delta\mathbf{c}$ are the changes in capacitance of each electrode pair and the elements of the vector $\delta\boldsymbol{\varepsilon}$ are the permittivity values of each pixel in the tomogram. The matrix $\boldsymbol{S}$ is called the sensitivity matrix and is the Jacobian of the system. $\boldsymbol{S}$ is usually calculated numerically by finite elements or finite differences but can also be constructed experimentally [6].

The objective of the work presented here, has been to investigate a new sensor geometry and to demonstrate that reconstruction can be handled with the usual methods but that it does cause artifacts in the tomograms. The reconstruction domain for the new geometry is a circular, concentric annulus, which enables the construction of a sensor that can be inserted into a tube and produce tomograms of the flow between the surface of the sensor and the inner wall of the tube. An inside-out sensor can then be moved in the longitudinal direction inside an outer tube; producing tomograms at different positions. The flow to be investigated will be a mixture of saltwater, hydrocarbons (oil and/or gas) and air. This geometry will be referred to as the inside-out geometry.

The consequence of the inside-out geometry is that the sensitivity matrices are of a significantly different shape than for the traditional case. This causes some artifacts, which need to be handled.

*Corresponding author
Email address: kem@mek.dtu.dk
(J.Kjærsgaard-Rasmussen)

The artifacts are most severe when linear back-projection is used for reconstruction, but other reconstruction methods also need to be suited to the inside-out geometry.

2. Materials and methods

2.1. Inside Out Geometry

The reconstruction domain, for the inside-out geometry, is an annulus. Figure 1 shows how the electrodes are placed close to the inner boundary of the annulus. The permittivity between the electrodes and the outer screen can be reconstructed from measurements of inter-electrode capacitances.

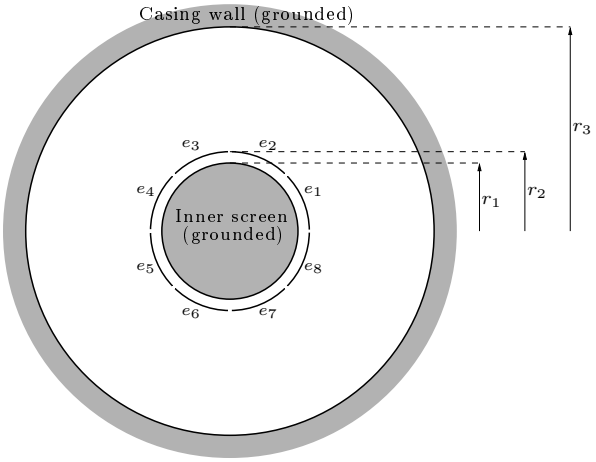

Figure 1: With an inside-out geometry, there are two grounding screens. One grounding screen is placed close to and inside of the electrodes and the other screen is placed outside of the electrodes.

The advantage of this geometry is that a sensor will be able to move inside the outer screen and thus be able to create tomograms at different sections of the flow in the annulus. The cylinders defined by the outside of the sensor-body and the inside of the outer boundary will be kept concentric, so the sensor will move parallel to the normal-vector of the plane of reconstruction. To avoid a long signal path for the control signal for the capacitance measurement circuits, the electronics can be contained inside the inner cylinder.

ECT sensitivity matrices for the capacitance between two electrodes can be calculated as inner products of the electric fields of the respective electrodes [7].

$$\boldsymbol{S}_{(i,j)k} = \boldsymbol{\nabla u_{ik}} \cdot \boldsymbol{\nabla u_{jk}} a_k \qquad (2)$$

where $\boldsymbol{S}_{(i,j)k}$ is the sensitivity of electrode-pair (i,j) at the k'th pixel, u_{nk} is the value of the potential of electrode n at the k'th pixel and a_k is the area of that pixel.

To obtain the potentials COMSOL was scripted from MATLAB. Using COMSOL made it possible to include all the design details of the sensor and thus obtain accurate simulations of the electric field. Figure 2 shows the mesh which was used for the finite elements method (FEM) simulations. The electrodes are mounted on the outside of a tube. The material of the tube has a permittivity value that differs from the permittivity between the tube and the screens, which is indicated by the red circular patch in the figure.

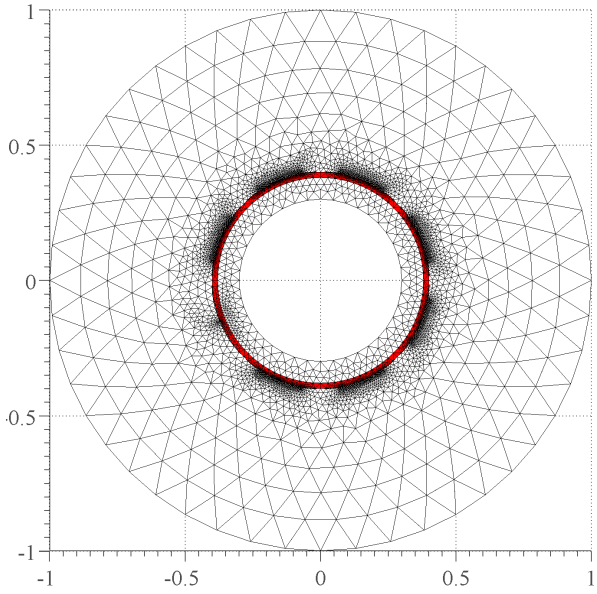

Figure 2: The figure shows a plot from COMSOL. The permittivity inside the model of the sensor has a relative value of 1 in most of the solution domain. The annulus (tube) just inside of the electrodes has a different permittivity. In this plot, the permittivity is set to 2, but the specific value depends of the material of the tube. Plastic, PEEK and ceramics are the three types of tube material that were used in this project.

The results of the FEM calculations was the electric field from one electrode, $\boldsymbol{u}_1$, sampled on an equidistant polar grid. The electrodes are equally distributed along the circumference, so $\boldsymbol{u}_i$ is rotationally symmetric with $\boldsymbol{u}_j$. It is thus only necessary to calculate a single FEM solution. The 7 remaining fields were obtained as rotations of $\boldsymbol{u}_1$ and then used to calculate the sensitivity matrix in

MATLAB via equation 2. The sensitivity matrix has a column for each pixel in the image and a row for each capacitance. The rows of the sensitivity matrix will be called sensitivity surfaces.

The sensitivity surfaces retain some of the rotational symmetry of the electrode-potentials. For example: $\boldsymbol{S}_{(1,2)k}$ is rotationally symmetric with $\boldsymbol{S}_{(2,3)k}$. There are four basic kinds of sensitivity surfaces, so all 28 surfaces are rotationally symmetric with one of four mother-surfaces. The four basic types depend on the distance between the electrode involved in that surface. The four basic sensitivity surfaces are shown in figure 3.

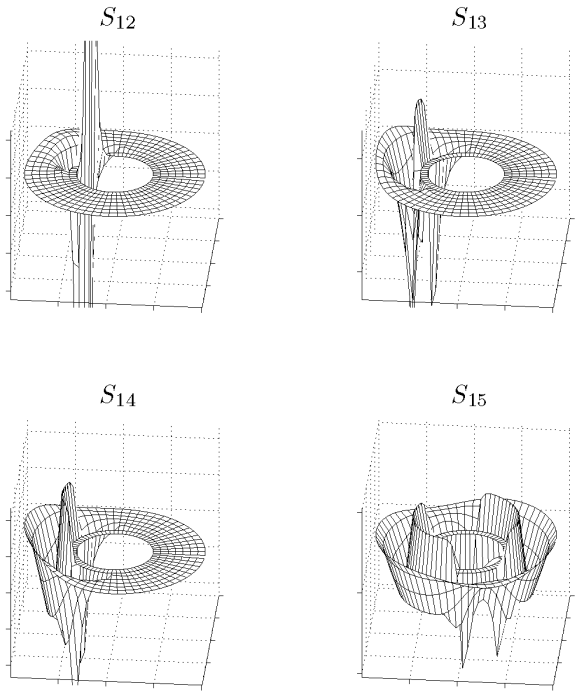

Figure 3: The figure shows the four basic sensitivity surfaces. $\boldsymbol{S}_{12}$ ($\boldsymbol{S}_{(1,2)k}$) is the sensitivity surface for the capacitance between electrodes 1 and 2 and so forth.

2.2. Reconstruction

Calculation of the sensitivity matrix for the inside-out geometry is relatively straightforward, since the usual methods can be used, but it turns out that the results cause some problems when they are used in the reconstruction.

A simple reconstruction method such as linear backprojection (LBP) uses a set of calibration measurements, $(c_{low}, \varepsilon_{low})$ and $(c_{high}, \varepsilon_{high})$, to normalize the measurements and resulting tomograms. In practice, this means recording the capacitances when the sensor contains only water ($(c_{high}, \varepsilon_{high})$) and then doing the same for air ($(c_{low}, \varepsilon_{low})$).

$$\tilde{c}_i = \frac{c_i - c_{low,i}}{c_{high,i} - c_{low,i}} \qquad g_k = \frac{\varepsilon_k - \varepsilon_{low}}{\varepsilon_{high} - \varepsilon_{low}}$$

where $\tilde{c}_i$ is the i'th normalized capacitance and g_k is the gray-level of the k'th pixel. Linear backprojection is a very fast technique because it uses a pseudo-inverse, $S^\dagger$, for the sensitivity matrix, to estimate the permittivity distribution via a single matrix multiplication.

$$\boldsymbol{g} = \boldsymbol{S}^\dagger \tilde{\boldsymbol{c}}$$

The pseudo-inverse is defined by a normalization of S, which ensures that each of the (normalized) capacitance vectors in the calibration set is mapped to the corresponding (normalized) permittivity distribution.

$$[S^\dagger]_{ij} = \frac{S_{ji}}{\sum_j S_{ji}}$$

This is a crude approach, but it provides reasonably accurate tomograms; especially for a conventional geometry. The sensitivity matrix can contain both negative and positive values, so one could worry about the denominator in the normalization and for the inside-out geometry this is a valid concern.

It turns out that the sum of the sensitivity for each capacitance vanishes for the pixels which lie close to a specific radius. Figure 4 shows a comparison of the sensitivity matrix for the conventional geometry and the inside out geometry. The average value of the sensitivity-sum,

$$s[r] = \frac{1}{N_\theta} \sum_{j:r_j=r} \sum_i S_{ij}, \tag{3}$$

at each radius is plotted. The choice of square brackets for indexing s is to emphasize that the radius is discretized; only certain r-values are valid. The number of pixels in the tangential direction is N_θ and $j : r_j = r$ means that the sum is over the indexes j that correspond to a pixel in the chosen radius r.

A conventional geometry results in a positive definite $s[r]$, but that is not the case for the inside out geometry. This results in some obvious problems

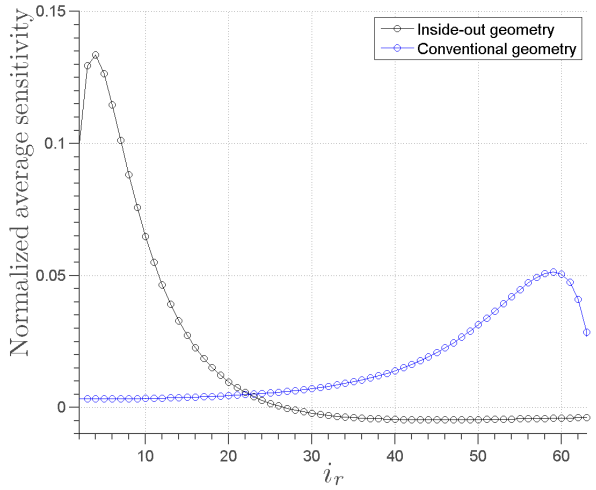

Figure 4: The figure illustrates how the average sensitivity of the inside-out geometry changes sign at a well-defined radius. The average sensitivity of a sensor with conventional geometry does not change sign, apart from very near to the electrodes. The radial vector of the conventional geometry spans from the center of the reconstruction domain to the outer screen. For the inside-out geometry it spans from the inner- to the outer screen.

with the normalization since it causes division by zero at certain locations. The pseudo-inverse thus diverges at the characteristic radius and this causes a circular artifact to appear in the reconstructed tomogram.

2.3. Smoothed Landweber

The Landweber algorithm is a flexible optimization-based technique which can be easily modified by the application of some fitting operator to each iterate of the algorithm [8, 9]. This flexibility caused a customized version of Landweber to perform better than several other reconstruction methods which were applied to the inside-out geometry.

The problems with the circular artifact from the LBP tomogram lead to the construction of an operator, Φ, which would counter the unwanted high frequency components of the LBP-artifact.

With a smoothing operator, the high activity in the area of the artifact is slowly moved to adjacent pixels. The Landweber algorithm does not re-introduce the artifact after it is removed. Since the algorithm propagates the solution in a direction which minimizes the residual, the act of actively removing the artifact seems to be justified.

The smoothing operator is periodic in the θ-direction and bounded in the radial direction. The gray-level of pixel i is altered by a mean operator to

$$g_i^* = \frac{4g_i + \sum_{k \in neighbors} g_k}{4 + \sum_{k \in neighbours} 1},$$

where g_i^* is the new value and g_i is the old one.

To avoid the smoothing operator dominating the Landweber iteration, it is applied during only a subset of the iterations. With active smoothing for 10% of the iterations, every L out of K iterations, the smoothed Landweber algorithm, in pseudo-code, is:

$\boldsymbol{\Delta\epsilon}_{[0]} = \boldsymbol{g}_{LBP}(c_{high} - c_{low})$
for $k = 1$ to K
  $\boldsymbol{\Delta\epsilon}_{[k]} = \boldsymbol{\Delta\epsilon}_{[k-1]} + \omega_L \boldsymbol{S}^T(\boldsymbol{\Delta c} - \boldsymbol{S}\boldsymbol{\Delta\epsilon}_{[k-1]})$
  if $\mod(k, L) = \frac{9}{10}L$
    $\boldsymbol{\Delta\epsilon}_{[0]} = \Phi\boldsymbol{\Delta\epsilon}_{[0]}$
  end
end

The initial guess for the permittivity change, $\boldsymbol{\Delta\epsilon}_{[0]}$, is supplied by the LBP solution $\boldsymbol{g}_{LBP}$ and the calibration capacitances. The optimization parameter ω_L controls the aggressiveness of the optimization.

The results of the smoothed Landweber algorithm can be compared with linear backprojection in some tomograms from a test of the sensor in figures 7 and 8.

2.4. Tomogram resolution

A question which is often asked by the interpreter of the tomogram is; what is the resolution? Such a question is in some respects meaningless since the resolution (in a traditional sense) of the tomogram is arbitrary. The number of base functions (pixels) for the permittivity can be set to any number, within reason.

The pixel-resolution of the tomogram is thus not the most vital parameter. Another, more meaningful, way to define the resolution is to ask how large a part of the reconstruction domain needs to be filled with high permittivity material, for the resulting capacitance change to be measurable. The change in capacitance is defined by equation 1 and

corresponds to

$$\tilde{c}_i = \sum_k g_k S_{ik} \tag{4}$$

Now, let the permittivity change that caused the capacitance, $\tilde{c}_i$, have a non-zero value only on a disk-shaped sub-domain of the reconstruction domain, Ω. The set of all such disk-shaped changes will be called Ω_D:

$$\Omega_D = \{w_i \in B_2 : w_i \subset \Omega\}, \tag{5}$$

where B_2 is the set off all disks (2-balls). The disks, w_i, have a a center $\boldsymbol{x}_i$ and area A_i.

The permittivity change is then

$$g_k = \begin{cases} 1 & \boldsymbol{x_k} \in \omega_i \\ 0 & \text{otherwise} \end{cases}, \tag{6}$$

where $\boldsymbol{x_k}$ is the position of the k'th pixel. The capacitance change then reduces to a sum over the indexes k that correspond to a pixel inside ω_i:

$$\tilde{c}_i = \sum_{k:\boldsymbol{x_k}\in\omega} g_k S_{ik}. \tag{7}$$

For the change, $\tilde{c}_i$, to be measurable, at least one of the i measured capacitances needs to change by an amount larger than the capacitance resolution of the charge-transfer circuits, ρ_c.

$$\rho_c \leq \left| \sum_{k:\boldsymbol{x_k}\in\omega_i} g_k S_{ik} \right| \tag{8}$$

The resolution depends on the position of ω_i; if it is located close to the electrodes, where the sensitivity is generally higher, the necessary size of ω_i is smaller than if the location is farther away from the electrodes.

The spatial resolution could be defined as the area of ω_i that ensures a measurable change, regardless of the position. This corresponds to finding the sub-set of Ω_D which contains disks that cause a change of exactly the same magnitude as the capacitance resolution and then finding the area of the largest of the disks in that sub-set.

$$\rho_A = \sup\{A_i | \omega_i \in \Omega_D \wedge \rho_c = \left| \sum_{k:\boldsymbol{x_k}\in\omega} g_k S_{ik} \right|\} \tag{9}$$

This expression could potentially be difficult to evaluate, but since we are looking for a minimum it is reasonable to expect that ω_i will be placed in the areas with small sensitivity. Fortunately, the variations in S in these areas are slow, so ρ_A can be approximated by investigation of a histogram of S.

Based on calibration measurements, figure 5 shows a histogram of the values of the highest bit-sensitivity

$$\frac{\partial c_b}{\partial \epsilon} = \frac{[\boldsymbol{S^b}]_{ij}}{a_j} \tag{10}$$

for each pixel. The bit-sensitivity, $\boldsymbol{S}^b$ is normalized such that

$$\tilde{c}_i^b = \sum_k \boldsymbol{S}_{ik}^b, \tag{11}$$

where $\tilde{c}_i^b$ is the value of the bit-wise change between the calibration measurements for electrode-pair i. The histogram shows that a large part of the reconstruction domain has the same low value for the bit-sensitivity.

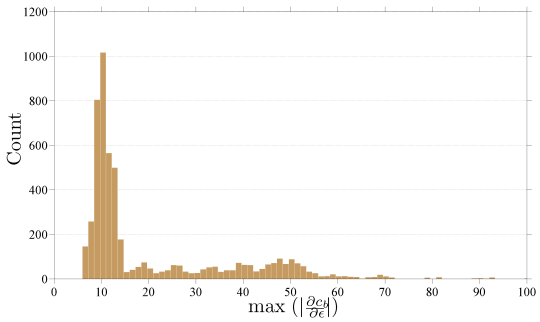

Figure 5: The plot shows that the reconstruction domain contains mostly pixels with a maximum sensitivity of approximately $\frac{10bit}{A}$, where A is the area of the domain.

$\frac{\partial c_b}{\partial \epsilon} = 10$ can be used to obtain an approximate value for ρ_A. The noise on the capacitance measurement circuits which were employed spreads over approximately 5 bits, so equation 7 reduces to

$$5 = \sum_j a_j 10 \Delta\epsilon_j \tag{12}$$

$$= 10 \sum_j a_j \Delta\epsilon_j \tag{13}$$

$$= 10 \Delta\epsilon \rho_A \tag{14}$$

where $\Delta\epsilon$ is the permittivity change between the calibration distributions and ρ_A is the area relative

to the total area. The resolution of the inside-out sensor is then

$$A_{res} = \frac{5}{10\Delta\epsilon} \approx 1\% \tag{15}$$

The meaning of 'resolution' is now based on detectable changes in capacitance measurements. A detectable change in capacitance will not necessarily produce a noticeable change in the tomogram since the tomogram depends on the exact shape of the sensitivity matrix in the associated area and on the choice of reconstruction method.

The exact value for the spatial resolution of 1% of the total area is a very rough estimate, but the derived expression for the spatial resolution is valuable since it shows how the spatial resolution depends on many factors. A high resolution leads to higher spatial resolution, but the medium also affects it, i.e. a sensor in oil/air will have a lower spatial resolution than a sensor in water/air. The geometry also affects the spatial resolution since a higher maximum sensitivity in each area of the annulus will lead to better resolution.

2.5. Geometry

A test-sensor was constructed. The outer radius of the sensor is 27.0mm and the electrodes are placed at a radius of 24.4mm. The electrodes are made from conductive aluminum tape, has an area of 9cm^2 and measures 50mm by 18mm. Inside of the electrodes, the inner screen is placed at 21.2mm.

To isolate the electrodes electrically from the reconstruction domain, they are mounted on the inside of a non-conducting tube which is shown in figure 2. The radius of the outer screen, r_3 can vary but will typically be in the interval $45mm < r_3 < 60mm$ and for the tests it was 48mm.

The ratio between the radius of the electrodes and the outer screen affect the shape of the sensitivity matrices and the location of the circular artifact. The choice of radii was based on the size of available housing for the sensor and standard sizes for the well-casing which was used as the outer screen. Optimization of this ratio has not been investigated.

2.6. Electronics

Capacitances are measured with charge-transfer (CT) circuits which have been well documented [10, 11]. The circuit boards need to fit inside the inner tube, so it is important that the design is compact. The design for the test sensor measured $132mm \times 100mm$, is powered by an external laboratory power supply and contains 8 identical CT channels, a multiplexer, shift-registers and a microcontroller.

Each electrode is associated with its own CT channel on the board. The state of each channel (active / measure / passive) is controlled by the microcontroller. Figure 6 shows the principal layout of the testprints.

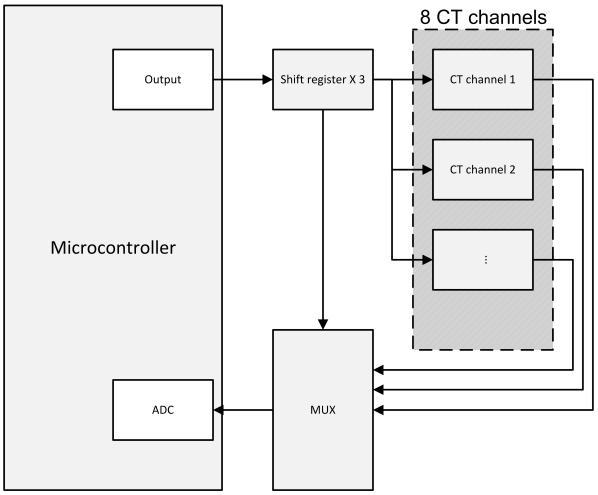

Figure 6: The figure shows the test print. The microcontroller sets the state of all the CT channels as well as the state of the MUX through the three shift registers. After a settling period, a number of measurements are taken by the analog to digital converter in the microcontroller.

The CT channels are controlled by a microcontroller through three 8-bit shift registers. The outputs of the eight channels are connected to an 8-channel multiplexer which in turn is also controlled by the microcontroller through the shift registers. The output of the multiplexer is connected to the analog to digital converter on the microcontroller. The analog to digital converter takes 336 capacitance measurements every second, which corresponds to a tomogram-framerate of 12Hz. The frames are transmitted from the microcontroller to a laptop PC via a small RS 232 module on an external print.

3. Results

The sensor was tested in a tank which was half filled with water. It was centralized inside an aluminum tube which could be raised and lowered in

the tank to move the air/water interface inside the reconstruction domain.

Tomograms produced by linear back-projection are presented in figure 7. The previously mentioned artifacts are present, but it is still possible to discern the distribution of water and air in the tomogram.

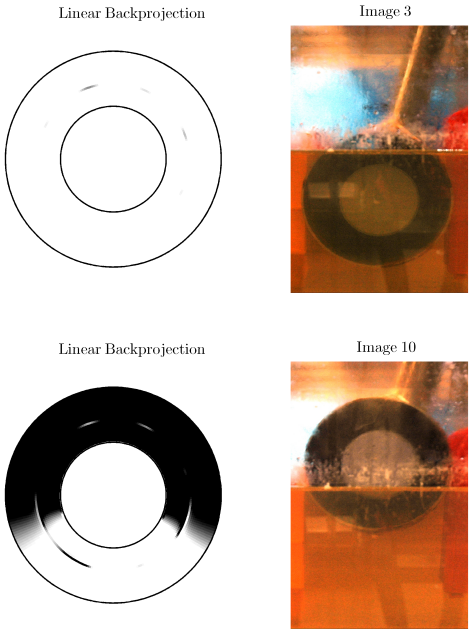

Figure 7: The figure shows a measurements in the test tank. The tomogram is on the left and the correponding 'flow' is on the right. The tomograms were produced by linear back-projection. The circular artifact, caused by normalization of the pseudo-inverse, is clearly visible.

Figure 8 shows tomograms produced by smoothed Landweber with the LBP tomograms as initial guess. The circular artifact is effectively removed by the smoothing and the horizontal interface between air and water is much better reproduced than with LBP.

Figure 9 shows a plot of the estimated watercut. The watercut has been estimated in three different ways. The 17 images were used to calculate an estimate of the watercut in the reconstruction domain and this is indicated by the 17 crosses on the plots.

The watercut was also estimated by a very rough method which is based directly on the 1-norm of the normalized capacitance vector.

$$w_c = \frac{||\tilde{\boldsymbol{c}}_i||_1}{28} = \frac{1}{28}\sum_i \tilde{c}_i \tag{16}$$

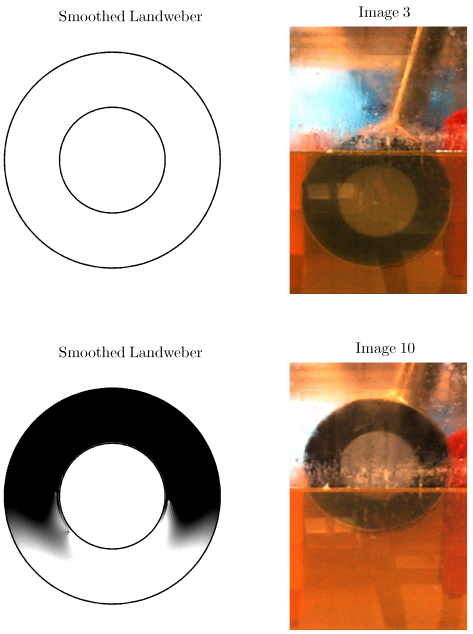

Figure 8: The figure shows a measurements in the test tank. The tomogram is on the left and the correponding 'flow' is on the right. The tomograms were produced by smoothed Landweber.

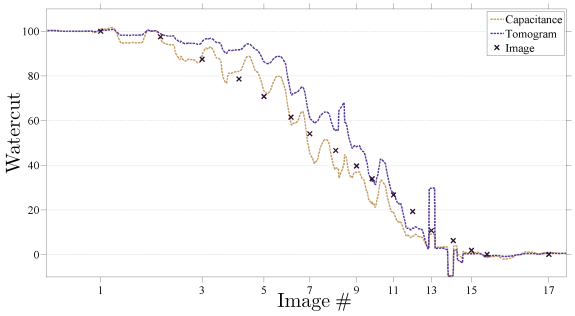

Figure 9: The figure shows the estimated watercut during the test. The watercut was estimated from the capacitance and the LBP tomogram for all frames and from the photo on 17 frames. The time when each of the 17 photos were taken are indicated on the x-axis.

where w_c is the capacitance based estimate of the watercut.

Finally the LBP tomogram was used to estimate the watercut.

$$w_t = \frac{\sum_k \boldsymbol{g}_k a_k}{A} \tag{17}$$

where A is the area inside the annulus and g_k

and a_k is the gray-level and area of the k'th pixel. The two watercut estimates are actually closely related. They are both weighted sums of the normalized capacitance vector, where all weights have the same value for w_c and the weights are largest for electrode-pairs that lie close to each other for w_t.

Both of the watercut estimates follow the estimation from the 17 images relatively well and especially the results from image 3 are noteworthy. The photo clearly shows that there is air inside the reconstruction domain but this barely registers on either of the tomograms. The graph in figure 9 does indicate that the watercut is somewhere near 90-95% though which seems reasonable. The air in the reconstruction domain is thus measurable, but not reproduced on the tomograms. As was briefly discussed after the derivation of the resolution, measurable changes in capacitance do not necessarily produce noticable changes in the tomogram.

4. Conclusions

An inside-out geometry has been presented and sensitivity matrices for the geometry have been calculated. The calculation was performed via a finite elements approach and the sensitivity matrices were produced in the conventional way, as inner products between the electric fields from electrode-pairs.

It was shown that the normalization of the pseudo-inverse used by linear-backprojection causes problems and that this problem is not present with sensors of a conventional geometry. A circular artifact appears at a characteristic radius in the inside-out LBP tomograms. A customized version of Landweber reconstruction was proposed and it was shown that this smoothed Landweber approach is able to handle the circular artifact and produce tomograms of higher quality than the LBP tomogram which is used as the initial guess in the algorithm.

The effective spatial resolution of tomograms was discussed and an expression which can be used as a basis for calculation of this resolution was proposed.

A test sensor was produced and it was shown that the effective spatial resolution was approximately 1% of the total area. The sensor was tested in a tank which was half filled with water. The results serve mainly as a proof-of-concept, but show that measurements of the watercut with an inside-out sensor in layered flows is possible.

[1] S.M. Huang, A.B. Plaskowski, C.G. Xie, and M.S. Beck. Capacitance-based tomographic flow imaging system. *Electronics Letters*, 24(7):418–419, 1988.

[2] Warsito Warsito, Marashdeh, Qussai, Fan, and Liang-Shih. Electrical capacitance volume tomography. *IEEE SENSORS JOURNAL*, 7(3-4):525–535, MAR-APR 2007.

[3] R. Wajman, R. Banasiak, L. Mazurkiewicz, T. Dyakowski, and D. Sankowski. Spatial imaging with 3D capacitance measurements. *MEASUREMENT SCIENCE & TECHNOLOGY*, 17(8):2113–2118, AUG 2006.

[4] W.Q. Yang and S. Liu. Electrical capacitance tomography with square sensor. *ELECTRONICS LETTERS*, 35(4):295–296, FEB 18 1999.

[5] Mark A. Nurge. Electrical capacitance volume tomography with high contrast dielectrics using a cuboid sensor geometry. *MEASUREMENT SCIENCE & TECHNOLOGY*, 18(5):1511–1520, MAY 2007.

[6] WQ Yang and WF Conway. Measurement of sensitivity distributions of capacitance tomography sensors. *REVIEW OF SCIENTIFIC INSTRUMENTS*, 69(1):233–236, JAN 1998.

[7] W Fang and E Cumberbatch. Matrix properties of data from electrical capacitance data. *Journal of Engineering Mathematics*, 14(51):127–146, 2005.

[8] JD Jang, SH Lee, KY Kim, and BY Choi. Modified iterative Landweber method in electrical capacitance tomography. *MEASUREMENT SCIENCE & TECHNOLOGY*, 17(7):1909–1917, JUL 2006.

[9] Geng Lu, Lihui Peng, Baofen Zhang, and Yanbiao Liao. Preconditioned landweber iteration algorithm for electrical capacitance tomography. *Flow Measurement and Instrumentation*, 16(2-3):163 – 167, 2005. Tomographic Techniques for Multiphase Flow Measurements.

[10] W Q Yang. Hardware design of electrical capacitance tomography systems. *Measurement Science and Technology*, 7(3):225–232, 1996.

[11] SM HUANG, CG XIE, R THORN, D SNOWDEN, and MS BECK. DESIGN OF SENSOR ELECTRONICS FOR ELECTRICAL CAPACITANCE TOMOGRAPHY. *IEE PROCEEDINGS-G CIRCUITS DEVICES AND SYSTEMS*, 139(1):83–88, FEB 1992.

Nomenclature

a_i	The area of the i'th pixel.
$\boldsymbol{c}_{high}$	A vector of 28 calibration capacitances for the high-permittivity distribution.
$\tilde{\boldsymbol{c}}_i$	The normalized capacitance between the i'th electrode-pair.
$\boldsymbol{c}_{low}$	A vector of 28 calibration capacitances for the low-permittivity distribution.
$\boldsymbol{g}_i$	Normalized grey level vector. i indexes the pixel.
e_i	The i'th electrode.
N_e	The number of electrodes in the sensor.
q_{ij}	The charge on e_j caused by applying a potential to e_i. Also written q_k, where k is the electrode-pair (i, j).
$\boldsymbol{S}_{ji}$	The sensitivity matrix. i indexes the electrode pair and j indexes the pixel.
$\boldsymbol{S}_{ij}^{\dagger}$	The pseudo-inverse of the sensitivity matrix. i indexes the electrode pair and j indexes the pixel.
u_i	The potential field caused by applying a potential to e_i and grounding the other electrodes.
w_c	Estimated watercut. Calculated from capacitance vector.
w_t	Estimated watercut. Calculated from a tomogram.
$\boldsymbol{x}_i$	The position of the i'th pixel.
$\delta\Omega$	The boundary of the reconstruction domain for ECT.
$\boldsymbol{\varepsilon}_{high}$	The high-permittivity calibration distribution.
$\boldsymbol{\varepsilon}_{low}$	The low-permittivity calibration distribution.
$\boldsymbol{\varepsilon}_i$	The permittivity distribution $(\varepsilon(x, y))$. i indexes the pixel.
Ω	The reconstruction domain for ECT.
ρ_A	The effective resolution of the tomogram.
ρ_c	The resolution of the capacitance measurements.

Appendix A

Wireline communication

Data from the ECT sensor is transmitted over the wireline to the controlbox. It is possible to have several sensors on the same toolstring, all communicating over the SNAP protocol on the internal databus of the toolstring. The data is handled by a central module and transmitted topside over the wireline, where it is received by a COM module inside the controlbox. A schematic of the setup is shown in figure A.1. The COM hardware and software has been developed and produced by the R&D department at Welltec.

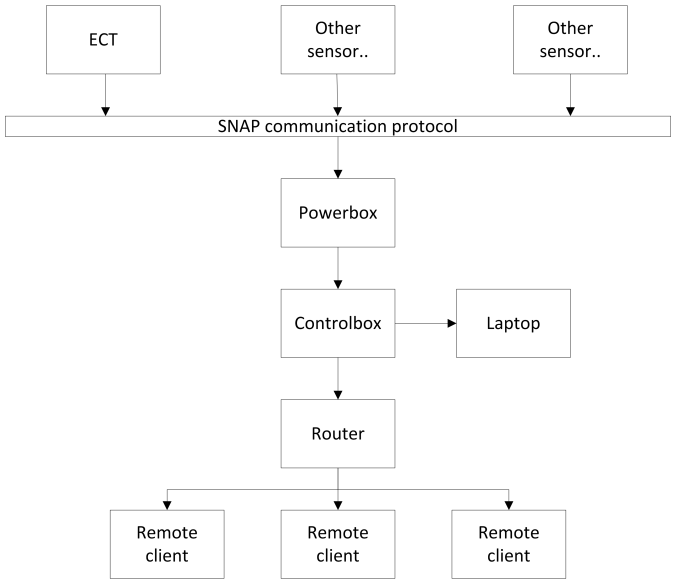

Figure A.1: The figure shows a schematic of the wireline COM.

Each data package from the sensor contains 68 bytes. The capacitance measurements are made with 16 bit resolution, so they make up 56 bytes of the package. The rest of the package contains the header, information about the datatype and tooltype, measurements from the accelerometer as well as temperature data. Table A.1 shows the

structure of an ECT package.

The capacitance measurements and the temperature value are resolved with 16 bits. All 16-bit numbers are sent in big-endian order.

ECT Data					
Byte number	**HEX**	**DEC**	**Data**	**Byte order**	**Group**
1	BC	188	Start package		**Header**
2	0	0	D addr.		
3	4	4	S addr.		
4	40	64	Length		
5	1	1	Datatype		
6	1	1	Toolnumber		
7			c_{12}	Small	**Capacitance measurements**
8				Big	
9			c_{13}	Small	
10				Big	
11			c_{14}	Small	
12				Big	
⋮	⋮				
59			c_{68}	Small	
60				Big	
61			c_{78}	Small	
62				Big	
63			Sequence number		
64			a_X		**Acceler-ometer**
65			a_Y		
66			a_Z		
67			T	Small	**T**
68				Big	

Table A.1: The table shows the structure of the data from the ECT sensor. The first four bytes comprise the header of the package. The 5'th and 6'th byte contain information about the tooltype (1:ECT sensor) and the datatype from that tool (1:Capacitance measurements). The next 56 bytes contain the capacitance measurements. Bytes 64 to 66 are output from the accelerometer and the final two bytes contains a temperature measurement.

APPENDIX A

Appendix B

The User Interface

The ectGUI is an interface to the Well Flow Imager. Figure B.1 shows the components in the data-transmission string from sensor to user interface. Besides presenting live

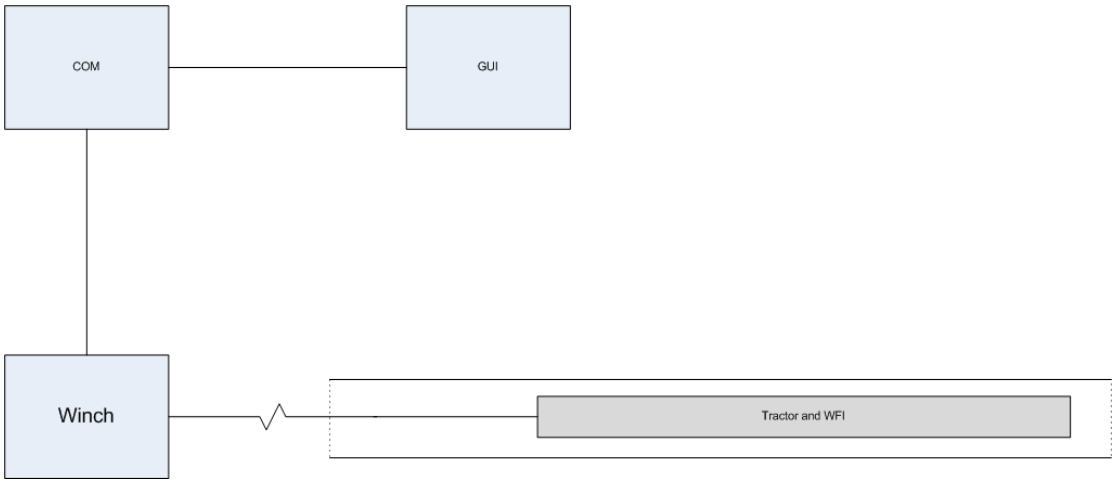

Figure B.1: The diagram shows how the WFI is connected to the interface at the top. The WFI is mounted on the tractor which makes it mobile inside the well. Communication is carried out over the wireline both back and forth. As capacitance data are sent over the wireline, the COM module decodes the information and the decoded data are made available to the reconstruction module. After reconstruction, the interpreted permittivity distribution is presented in the GUI.

images, ectGUI shows a live histogram and a history of the measurements from the latest few minutes.

There are two main versions of the software, both written in MATLAB. One version has been written for testing purposes and another was written for use by field engineers (FE's). The testing version runs natively in MATLAB and makes it possible to inspect

and manipulate data directly as well as to access any part of the program as desired. The FE version has been compiled so it can be interfaced from the FE cockpit. It has much fewer features, although many hidden functionalities have been maintained. The version referred to in this mini-guide is the FE version.

Besides live imaging it is possible to load a data file from a previous run and of course to continuously save the current run to file.

Setup

To get everything up and running, it is necessary to make a few choices. Imaging depends on a sensitivity matrix and a calibration set, so these need to be specified.

If a sensitivity matrix is not selected, a default one will be used, but it is important to choose a sensitivity matrix corresponding to the current sensor and casing, to achieve proper imaging results.

A calibration file must also be loaded. If one is not loaded, a default calibration set will be used. As with the sensitivity matrix, it is important to use a proper calibration file to obtain high quality imaging. It is possible to produce a calibration set from the current run, so the calibration can be updated live if desired.

Quick example

For a quick demonstration, an example of a data file can be loaded. This is done by, after starting up the program, selecting (see figure B.2):
`File -> Load...`
The data are now loaded and a sensitivity file needs to be loaded. This is done under
`ECT -> Sensitivity Matrix...`
The final thing to do is to load the calibration file. Do that under
`ECT -> Calibration File...`
Pressing the play button will initiate playback of the recorded data.

Calibration

The calibration file contains two datasets. One set is the measured capacitances from a previous run in air and the other is the measured capacitances while the sensor was in water. A calibration file can be loaded under
`ECT->Calibration File...`
Calibration files are saved in `.mat` format. If all channels do not measure 0 and 1, or

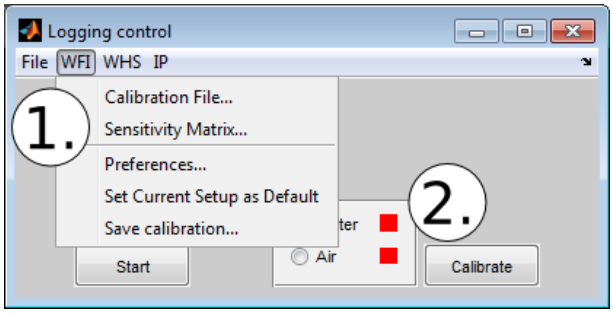

Figure B.2: The control window contains all the menus (1). Settings are controlled from the central window and calibration is also carried out from here (2)

very close to those values, when the sensor is in air and water, respectively, another calibration file needs to be loaded. When the sensor is in a mixture of air and water, it is possible for a capacitance value to go outside the range from the calibration, this is because there are both areas with negative and positive sensitivity inside the sensor area.

Sensitivity Matrix

The sensitivity matrix is used to convert the measured capacitances into an image to be presented in the GUI. The sensitivity matrix is thus an extremely important part of producing an accurate image. The sensitivity file is created from simulations of the electrical field between the sensor and the casing. A file with sensitivity data for the sensor and casing can be loaded under

`Settings->Sensitivity Matrix...`

Sensitivity matrices are also saved in .mat format.

There should be a sensitivity matrix constructed for every sensor geometry and it is essential for correct image reconstruction that a proper sensitivity matrix is loaded.

Color Scale

The result of the image reconstruction is a list of numbers. To turn the numbers into an image, the numbers need to be translated into colours. The calibration is supposed to put the values of water and air to 1 and 0, respectively. The default colour range is thus from 1 to 0, but sometimes it is advisable to change that range.

This can be done by clicking on the histogram (see figure B.2) on the upper right. A left click will move the lower value and a right click will move the higher value.

Sometimes a choice of about 0.4 as the lowest colour value will give a less noisy image.

Adjusting the color scale will not give a drastic change in the image, but it can sometimes give an image with better contrast.

B.1 Data Viewers

There are three different plots that display data from the ECT sensor. They are shown in figure B.3. The central display is the reconstructed image, but the two graphs can be very helpful as well.

The Histogram

The histogram shows the number of pixels with a specific value. When the sensor is covered in water a peak centered around 1 should be shown on the histogram since most of the pixels would then have that value. Depending on the chosen colorscale,

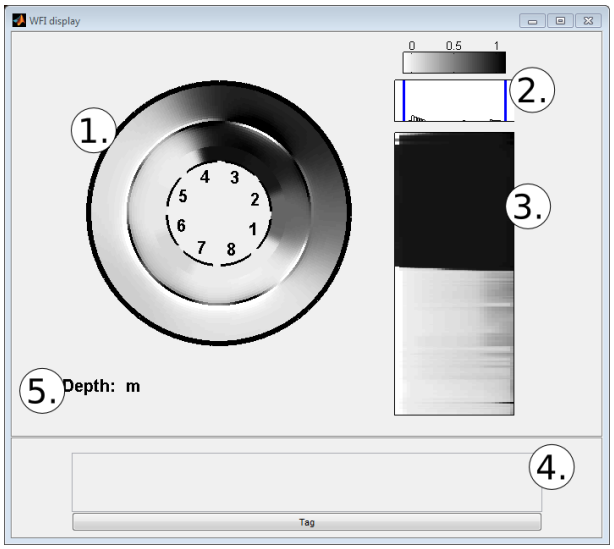

Figure B.3: The WFI window contains several views of the data from the WFI sensor. The tomogram (1) is the central part of the interface. A live histogram (2) of the tomogram is also shown. A history of the phase distribution over the last 5 minutes is shown on the right side of the window (3) and a depth indicator (5) is placed beneath the tomogram. Finally it is possible to add comments to the data as it is logged by using the tag box (4).

patches in the image with two different but similar values can be difficult to distinguish. On the histogram the will instead show up as two distinct, but close-lying peaks. The 'contrast' can sometimes be better on the histogram than in the image.

Flow history

The flow history represents the phase distribution in the last couple of minutes. Each line in the flow history corresponds to the phase distribution at a certain time in the past.

If a tomogram is displayed as an image with P pixels and contains V different pixel values, then the corresponding line in the flow history will contain V line-segments, L_v, each with a length corresponding to the number of pixels with the specific value v

$$L_v = \frac{N_v}{N}.$$

The P line-segments are ordered so that the segment corresponding to the lowest pixel-value is the leftmost, then the segment corresponding to the next highest pixel-value and so on.

Winch Com

To read depth data from the winch, it is necessary to first open up the com port of the winch. Afterwards, depth data will be read from the winch every second and when a tag is made. If the com port is not opened NaN values will be recorded for the depth.

The default value for the winch com-port is com3.

Raw Data

It is possible to open up a small window that shows the raw data coming from the ECT sensor over the wireline. The window is shown in figure B.4. This is a useful feature for debugging. Choosing `Raw Data` will open a window showing the raw data values

Figure B.4: The raw data window makes it easy to see if there is a problem with any of the channels.

being read over the com port. The values are ordered so that when the sensor is in a homogenous distribution, the values in each column should be similar. The leftmost

column contain all adjacent electrode pairs; ie. 1-2, 2-3 etc.. The next column contain all pairs that have a distance of two electrode-widths between their centers; ie. 1-3, 2-4 etc.. Pairs with distances of 3 and 4 electrode-widths are in the next two columns. As can be seen in figure B.4, there are only 4 pairs with a center distance of 4 electrode-widths.

Appendix C

Tank test

This chapter shows all the images and matching tomograms that were made for the test which is reported in the article in section 8.4.

C.1 Linear backprojection

These are the tomograms which were reconstructed through linear backprojection.

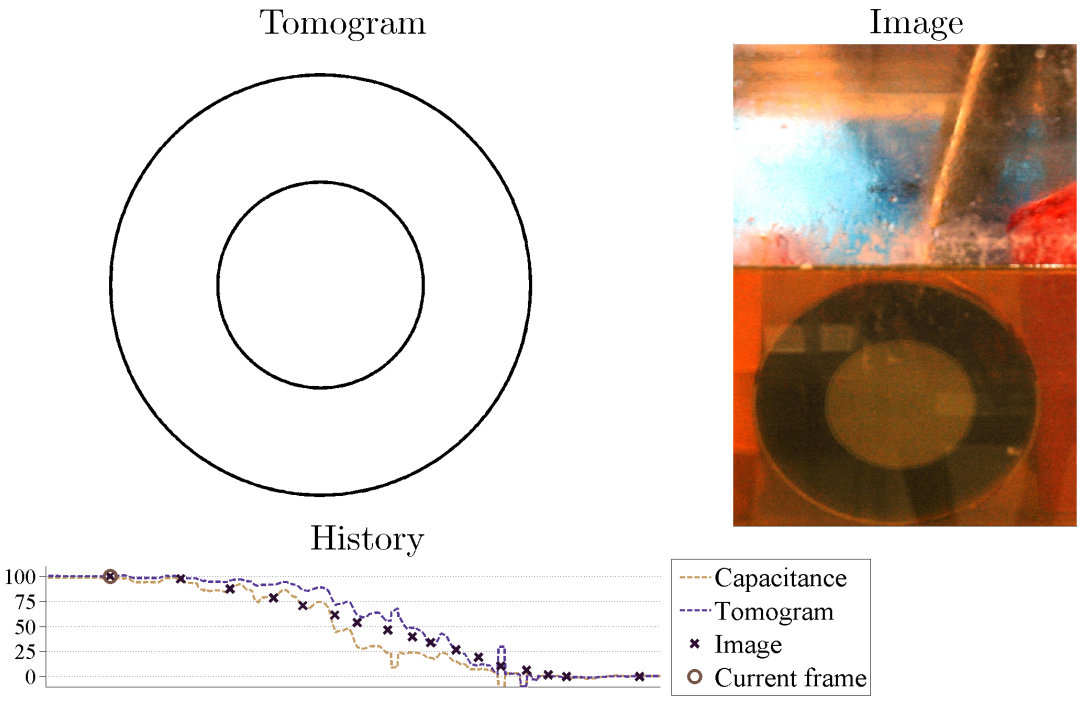

Figure C.1: T

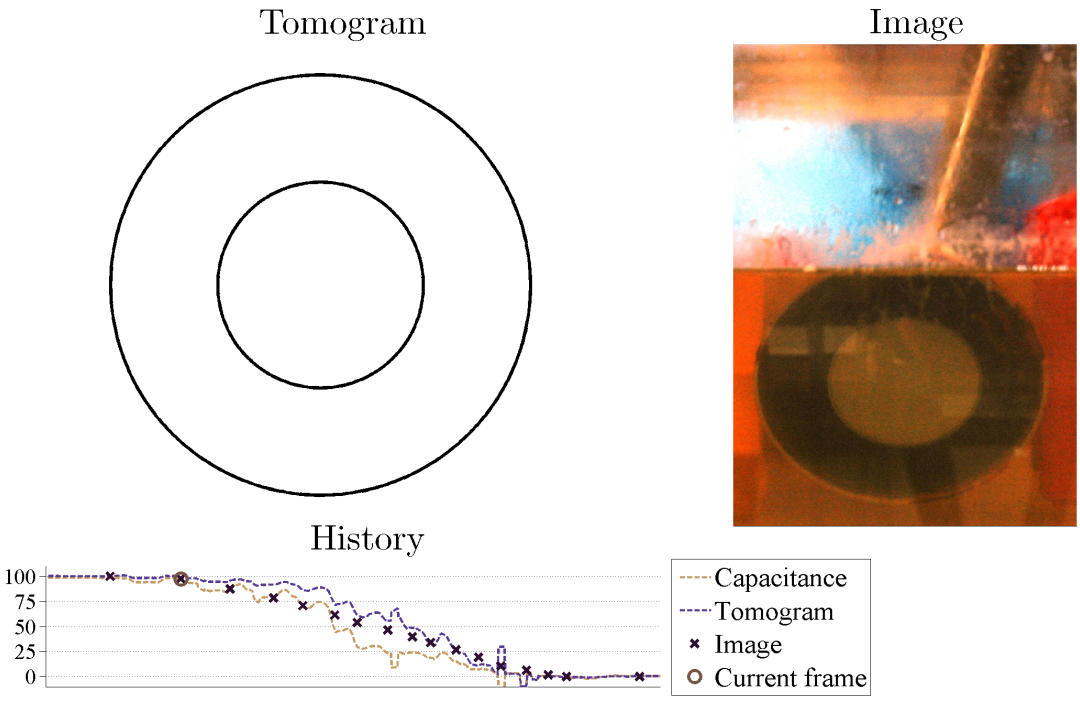

Figure C.2: T

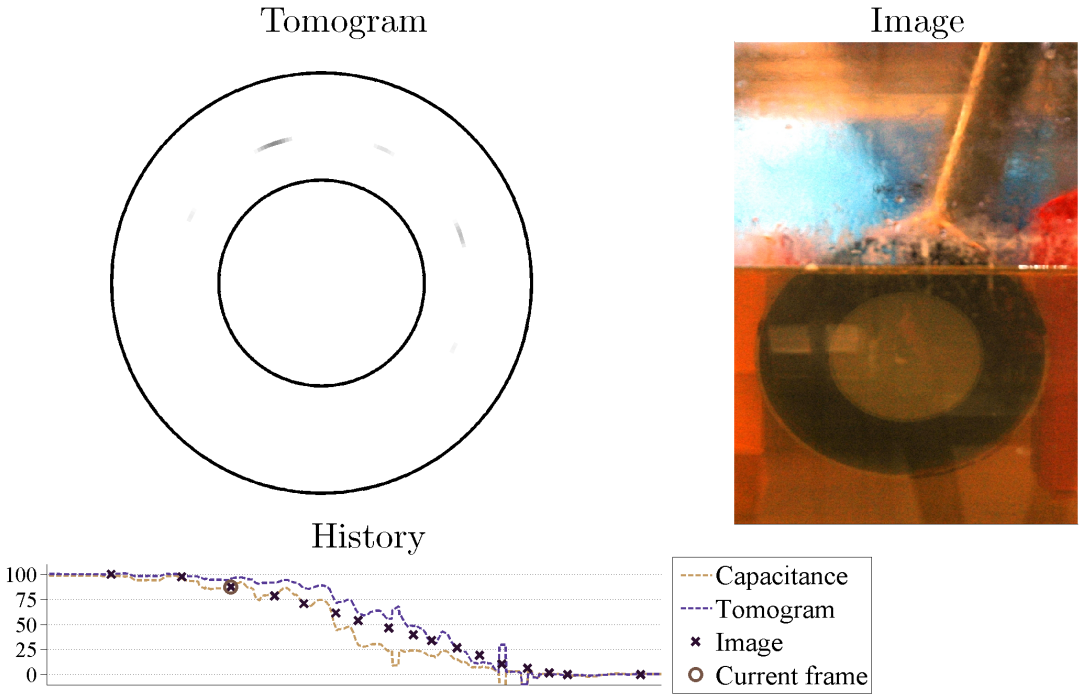

Figure C.3: T

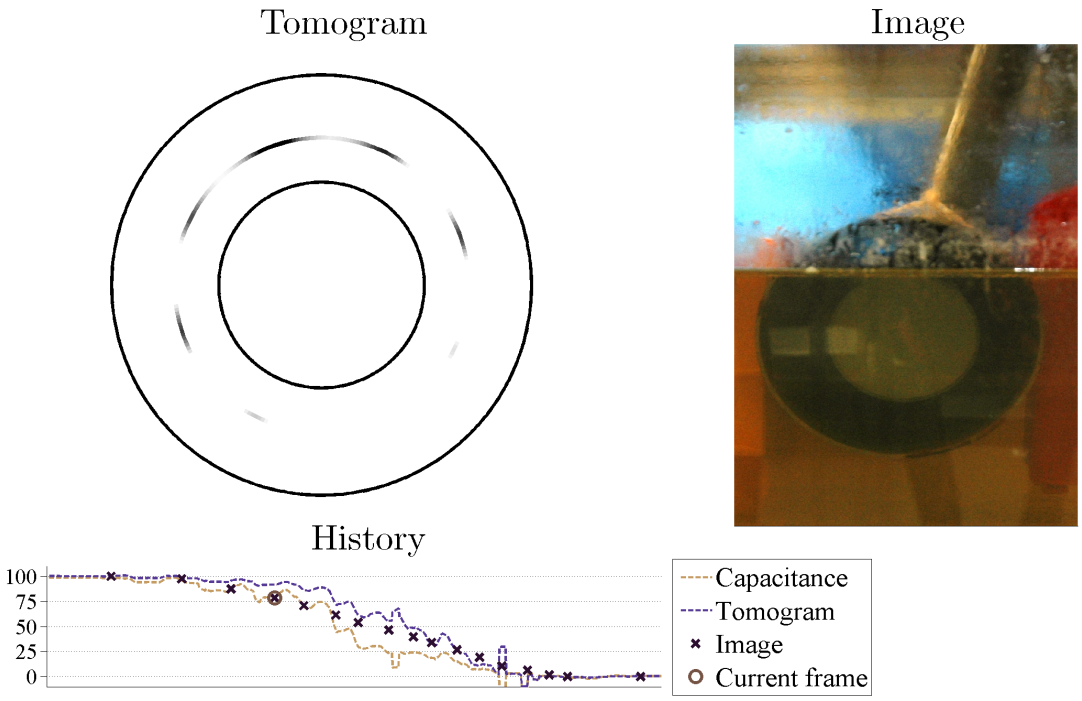

Figure C.4: T

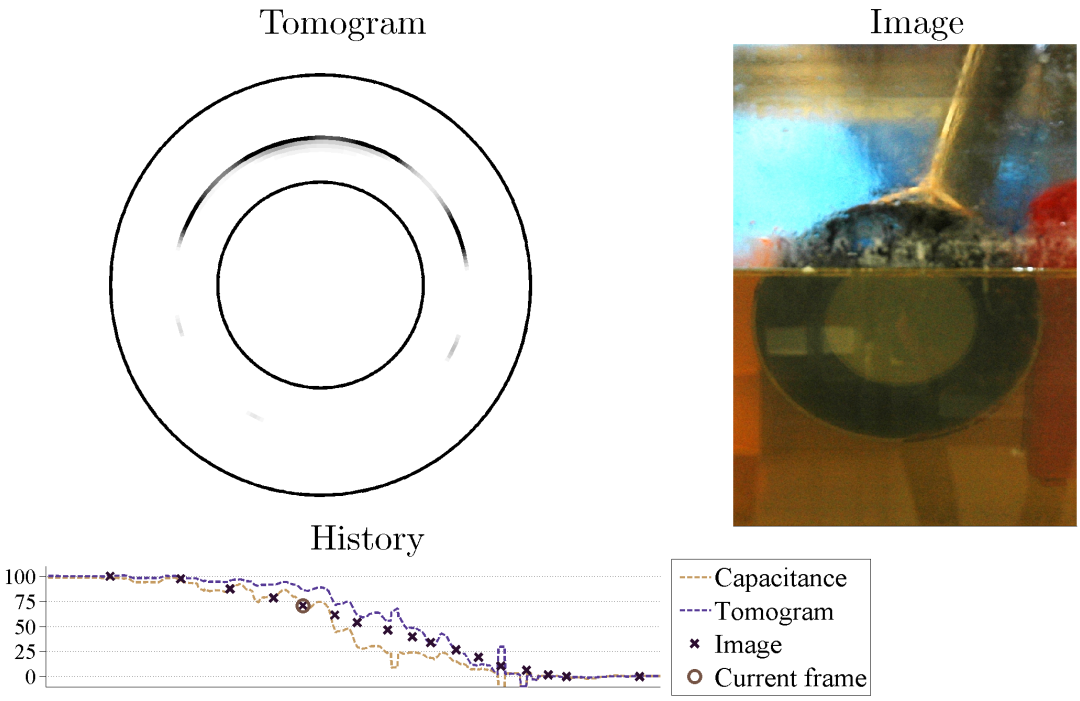

Figure C.5: T

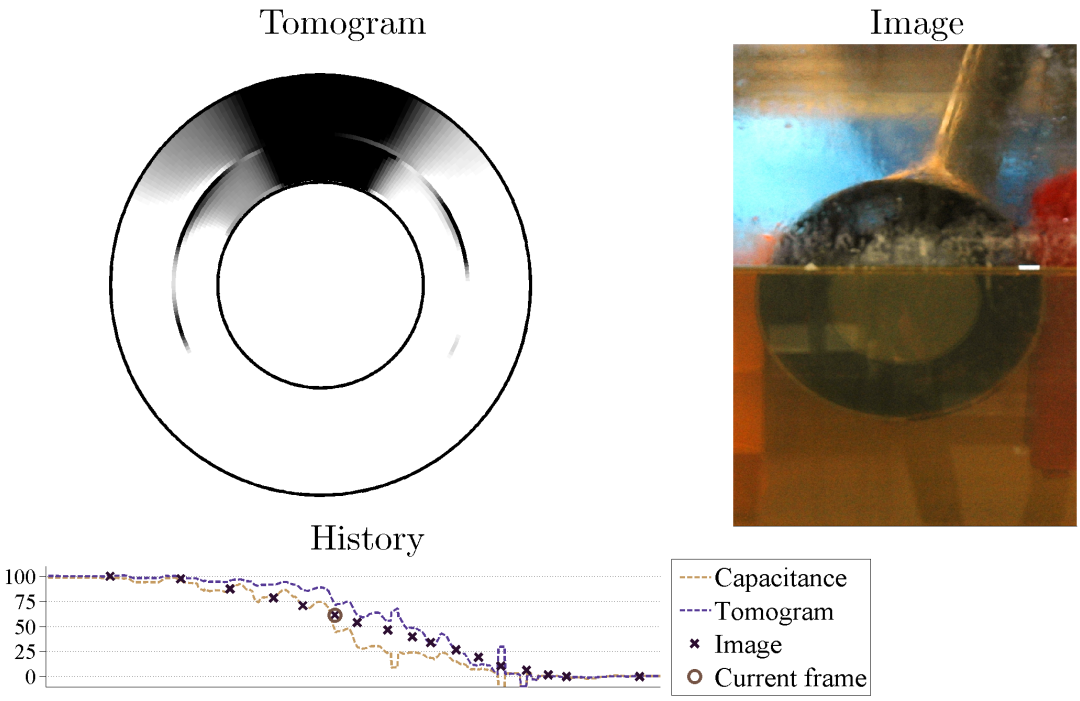

Figure C.6: T

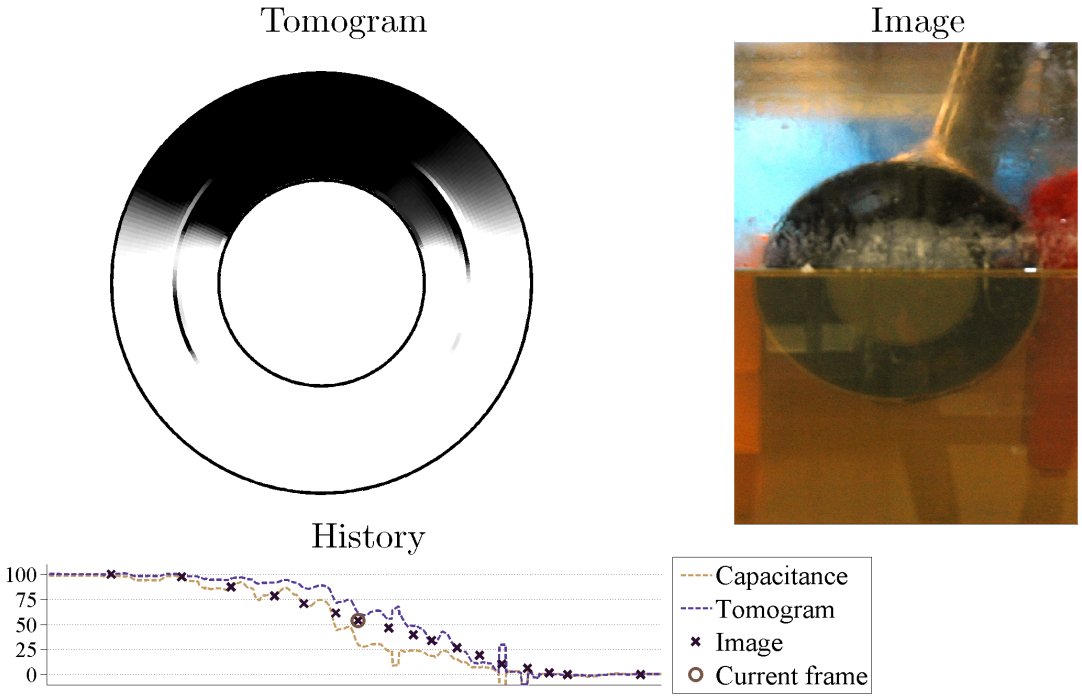

Figure C.7: T

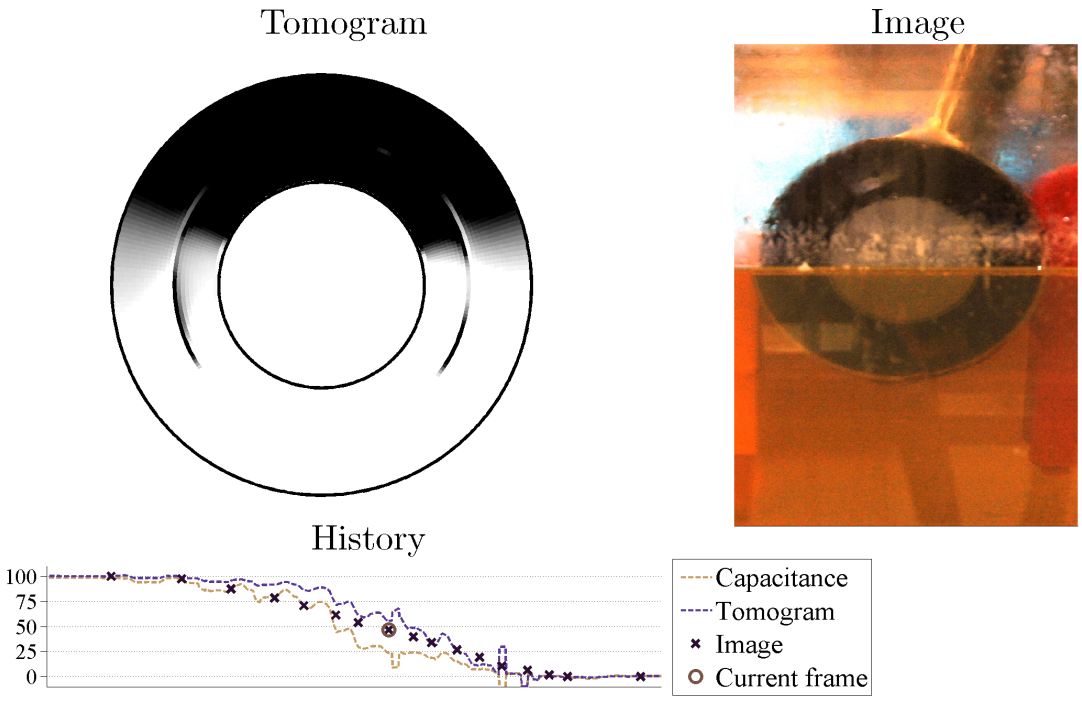

Figure C.8: T

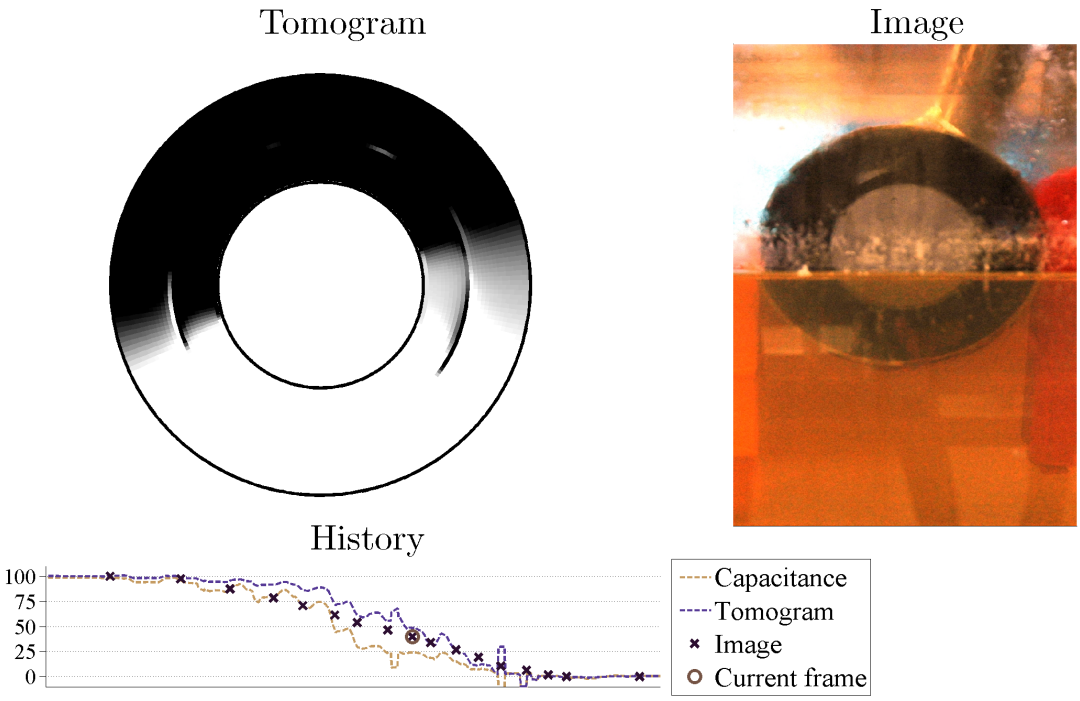

Figure C.9: T

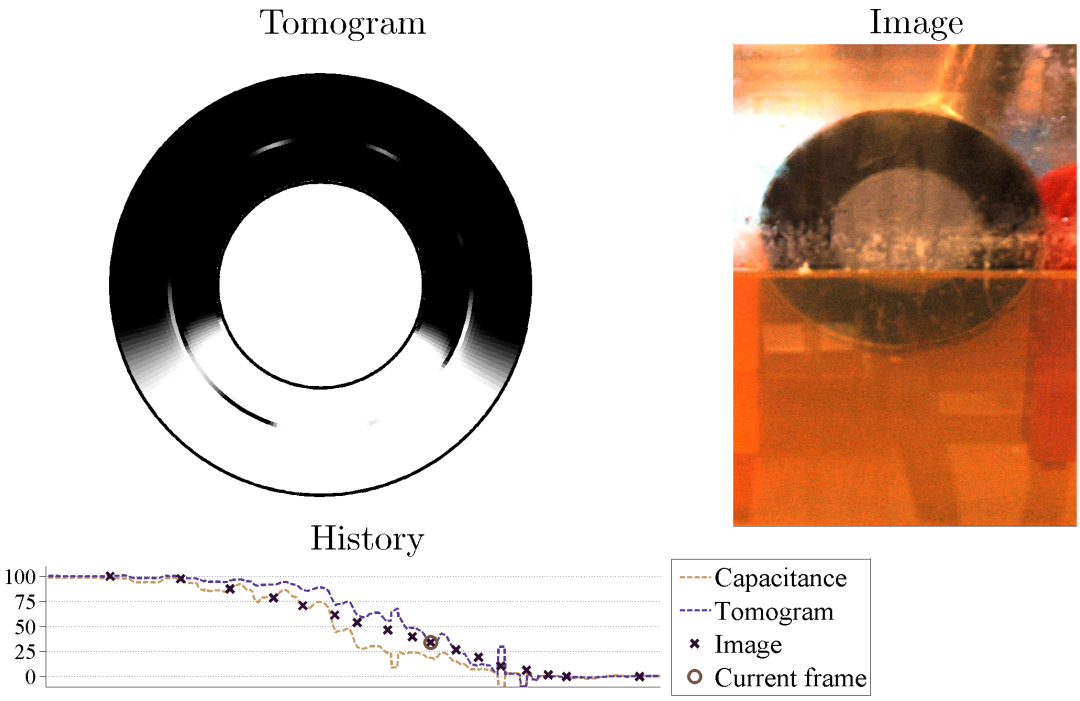

Figure C.10: T

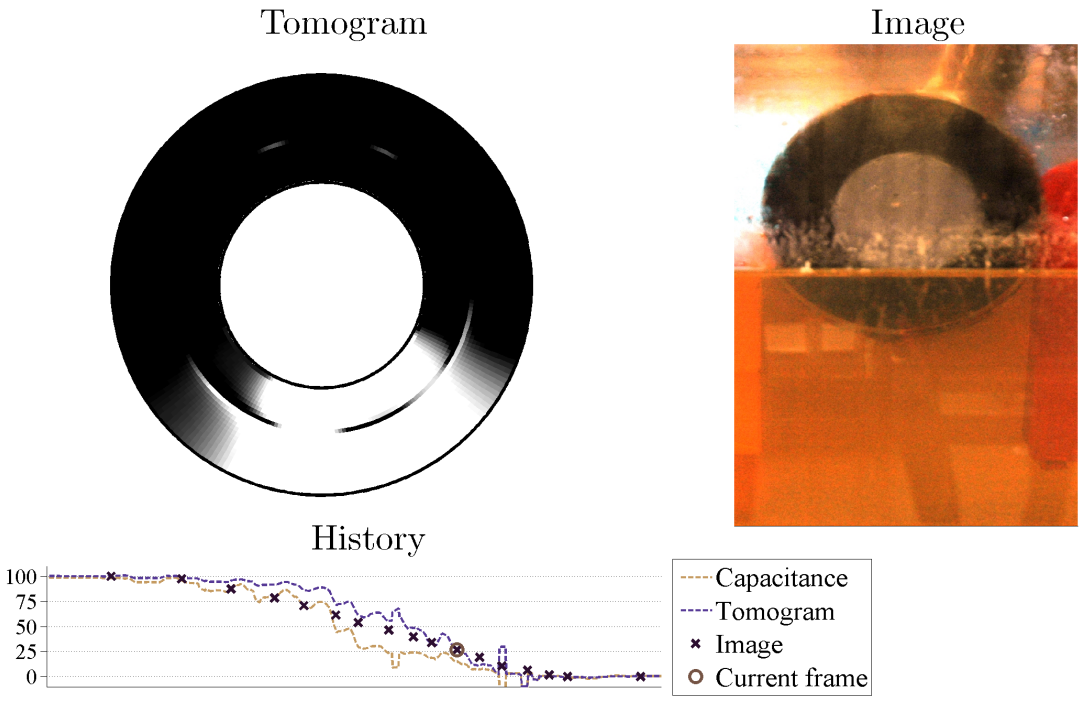

Figure C.11: T

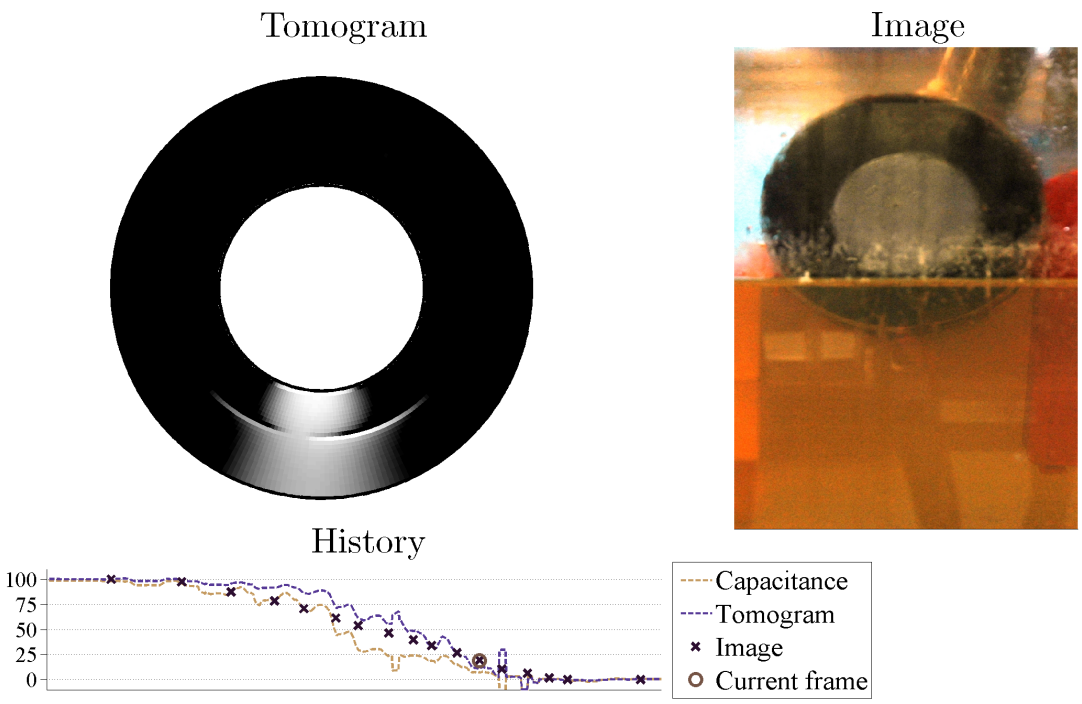

Figure C.12: T

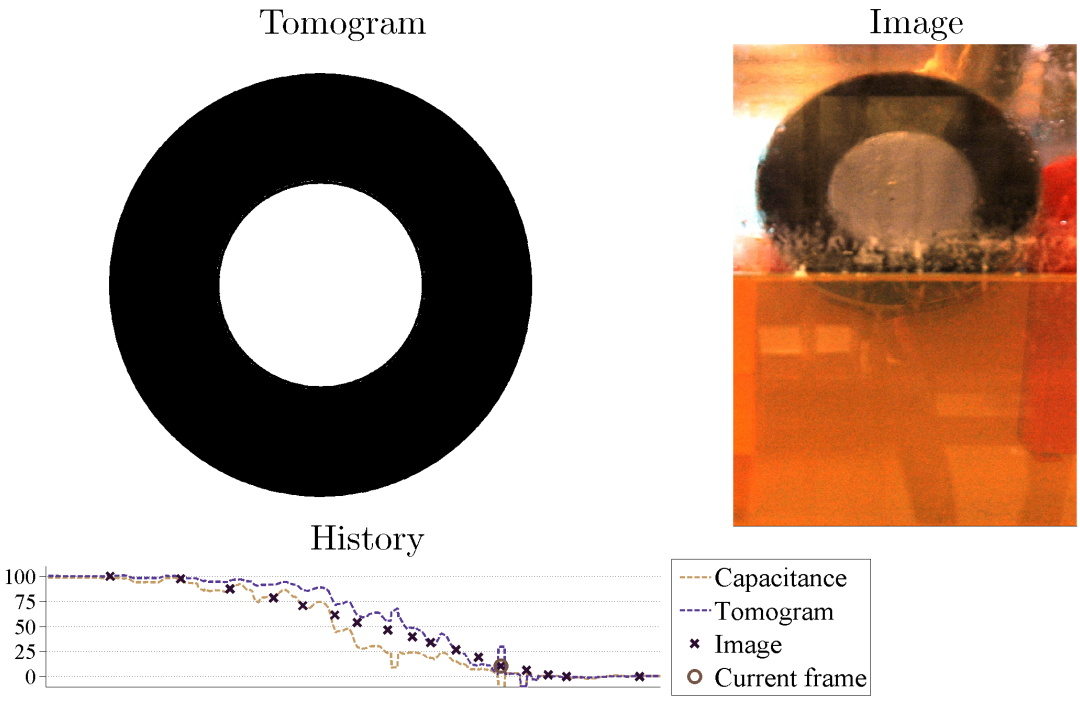

Figure C.13: T

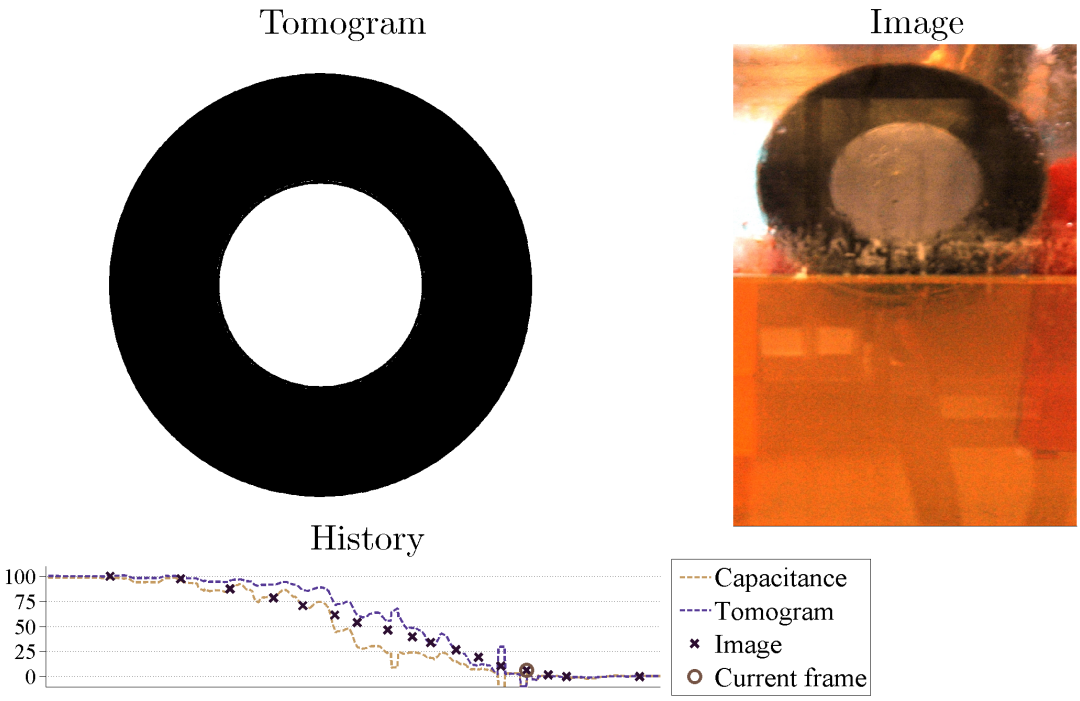

Figure C.14: T

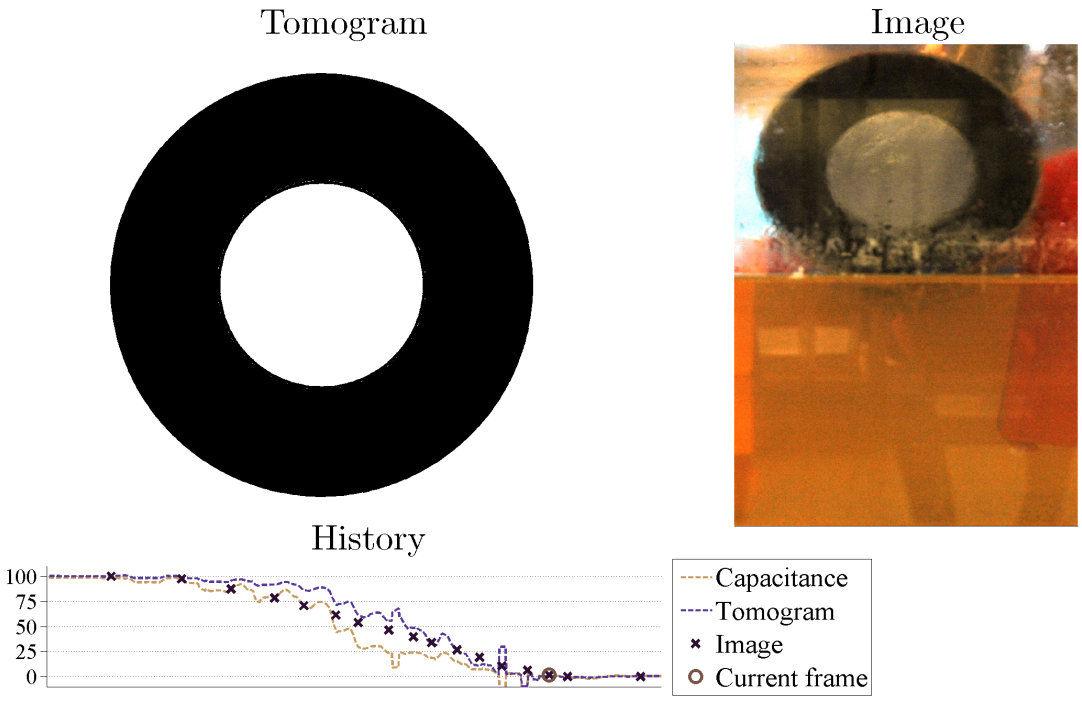

Figure C.15: T

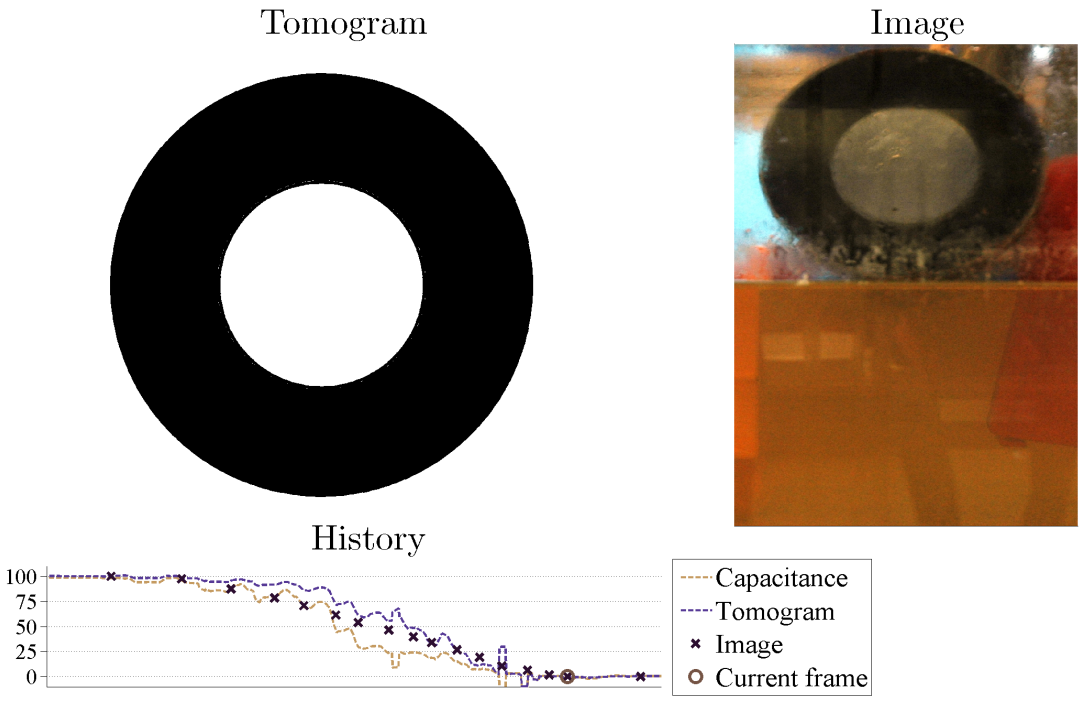

Figure C.16: T

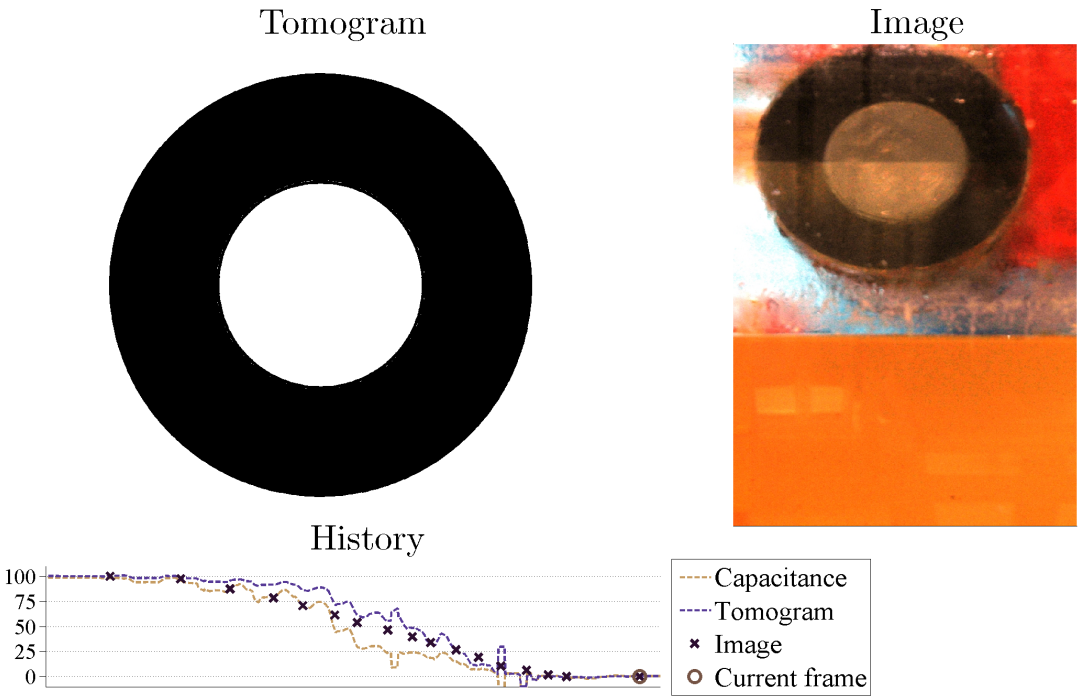
Tomogram
Image
History
100
75
50
25
0
Capacitance
Tomogram
Image
Current frame

Figure C.17: T

C.2 Smoothed Landweber

These are the tomograms which were reconstructed through smoothed Landweber.

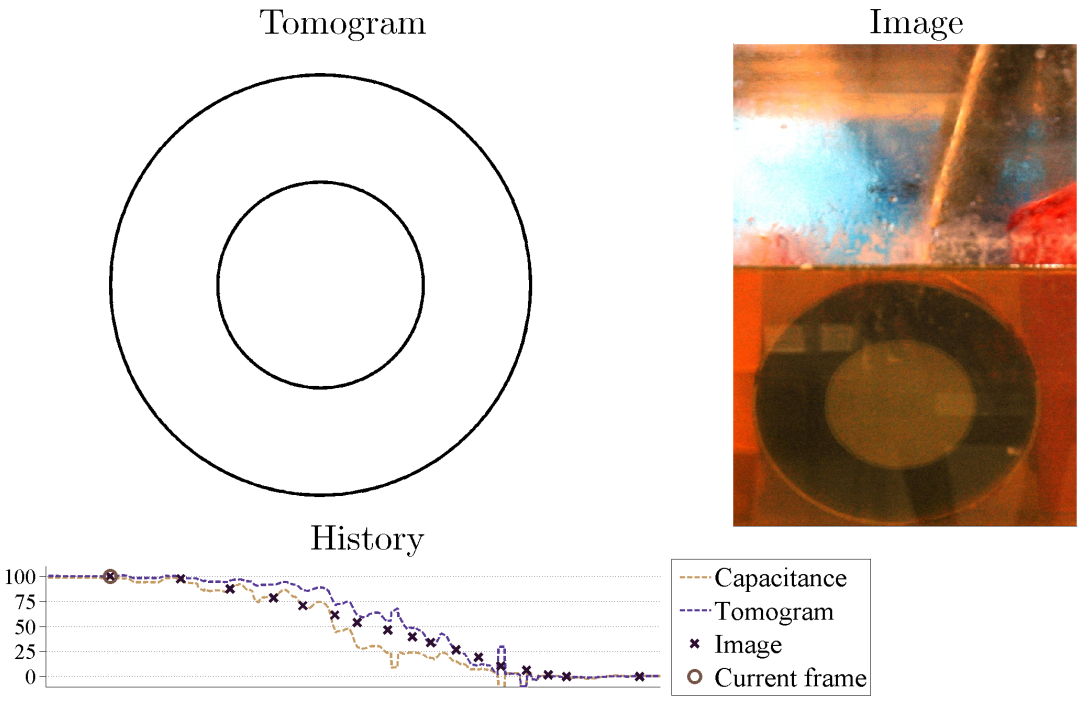

Figure C.18: T

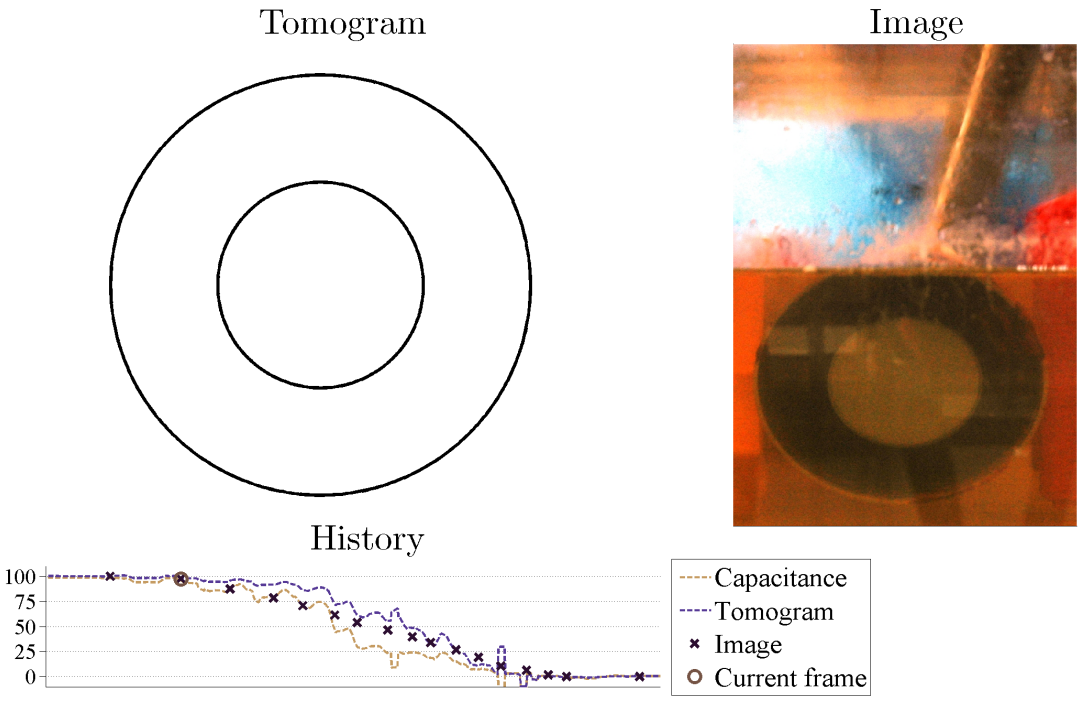

Figure C.19: T

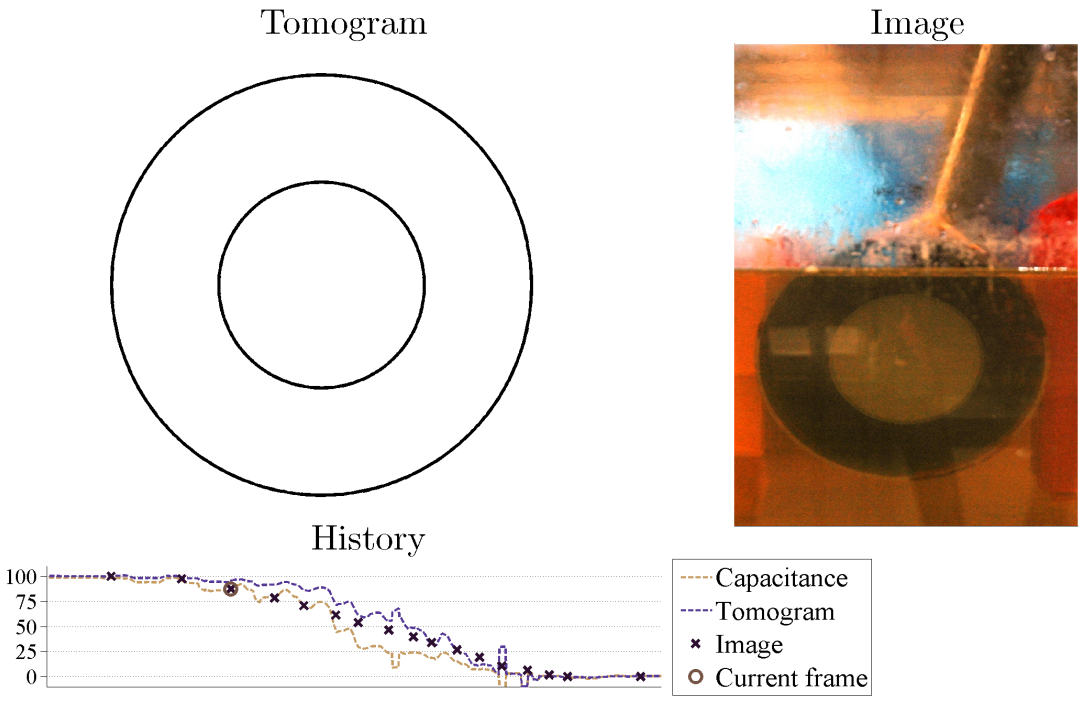

Figure C.20: T

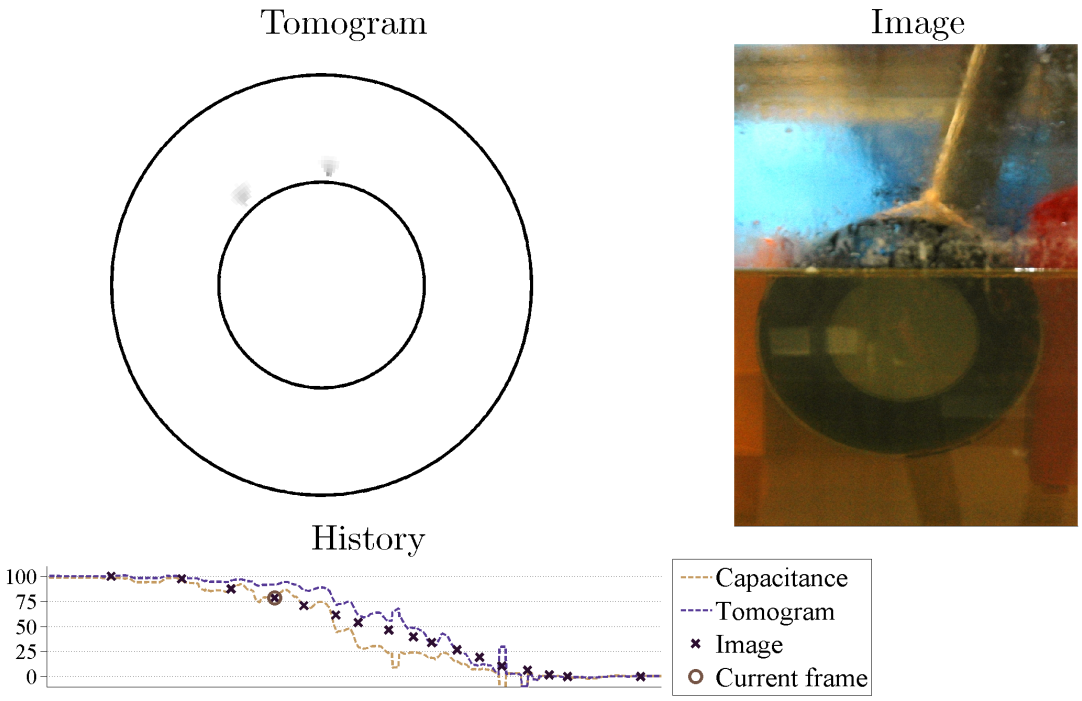

Figure C.21: T

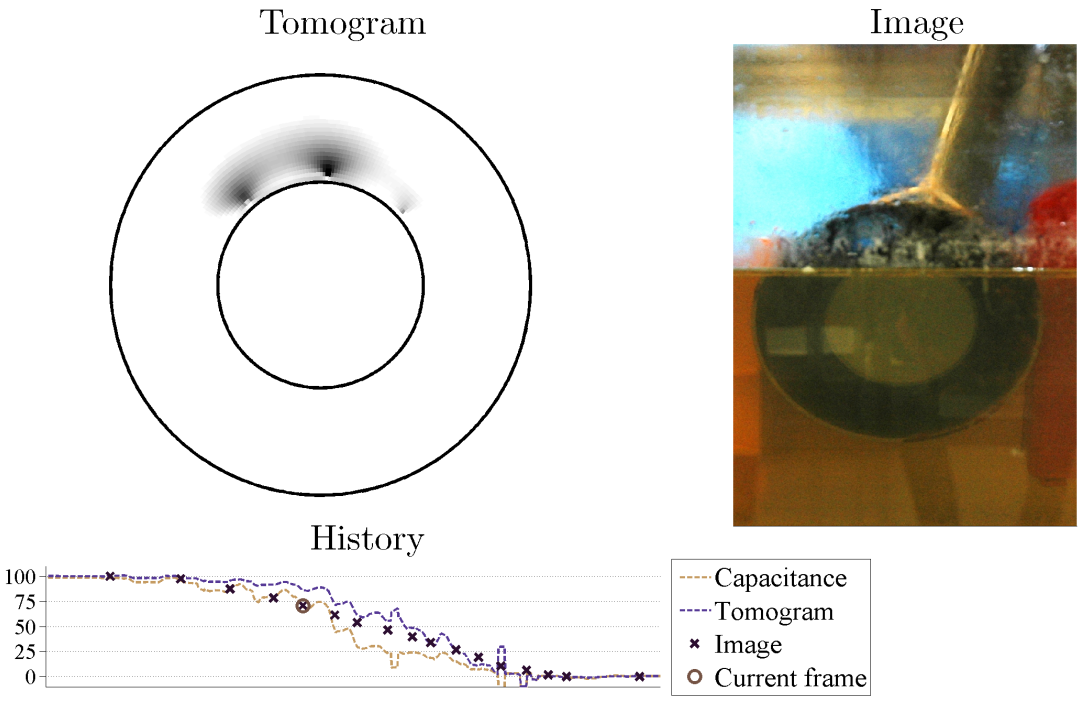

Figure C.22: T

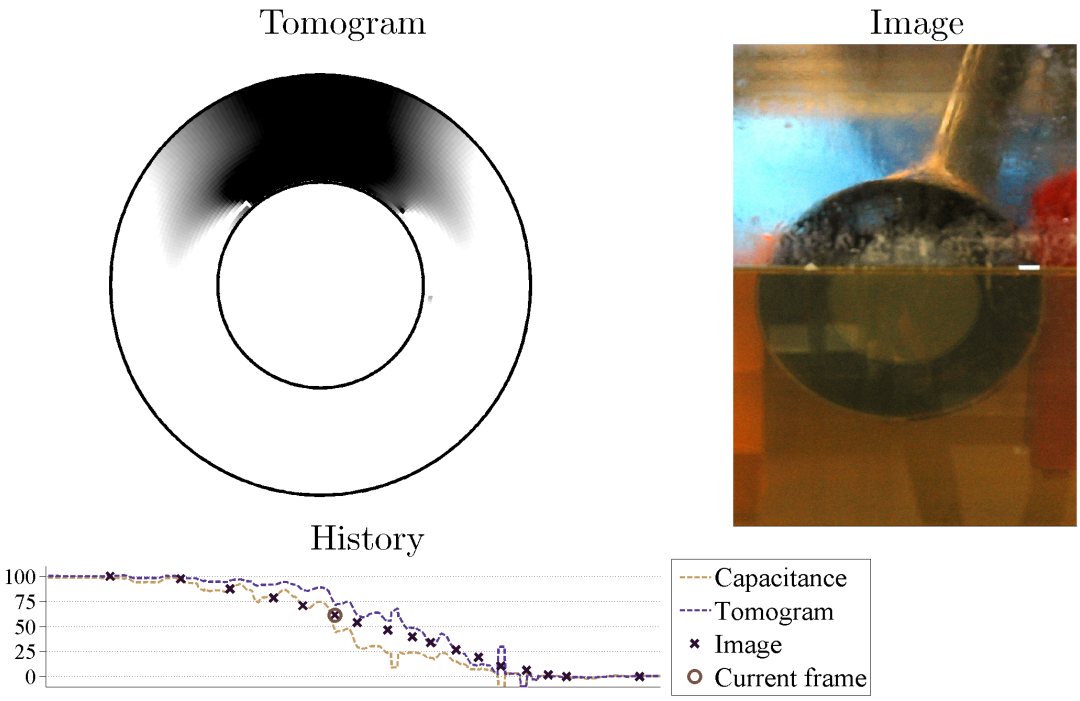

Figure C.23: T

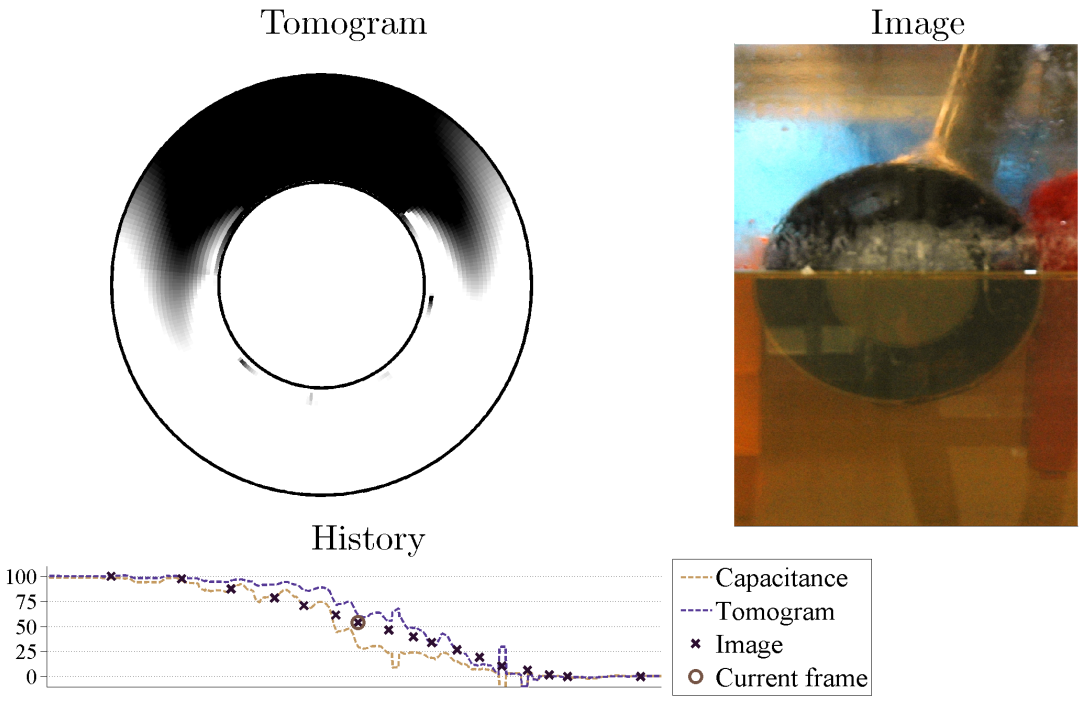

Figure C.24: T

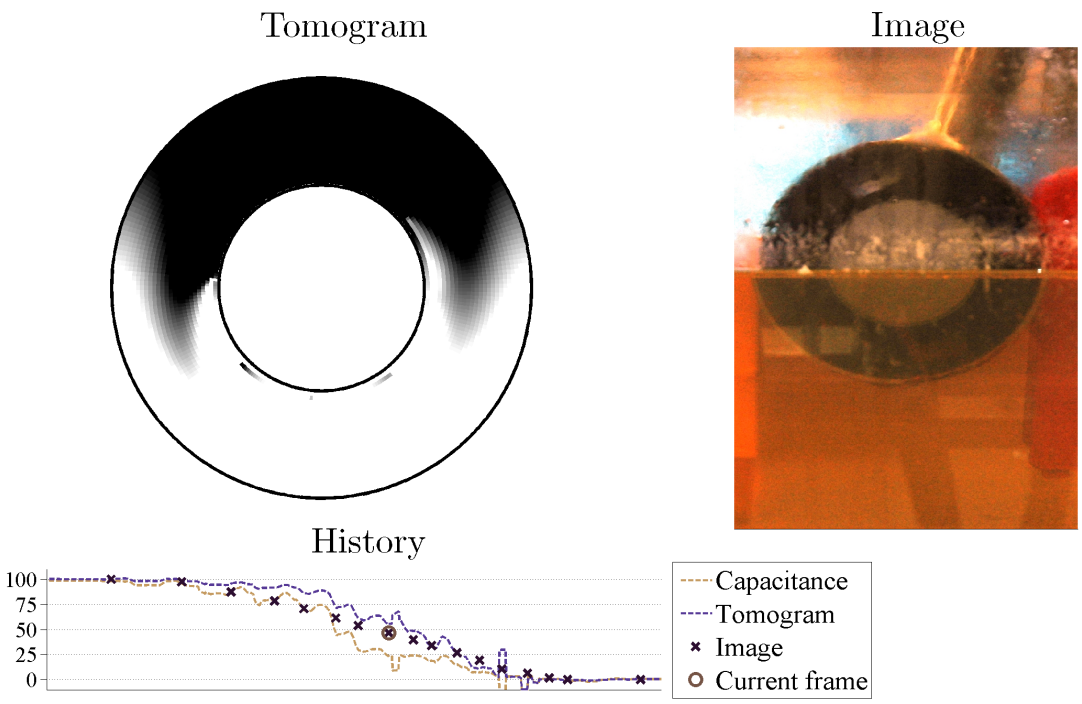

Figure C.25: T

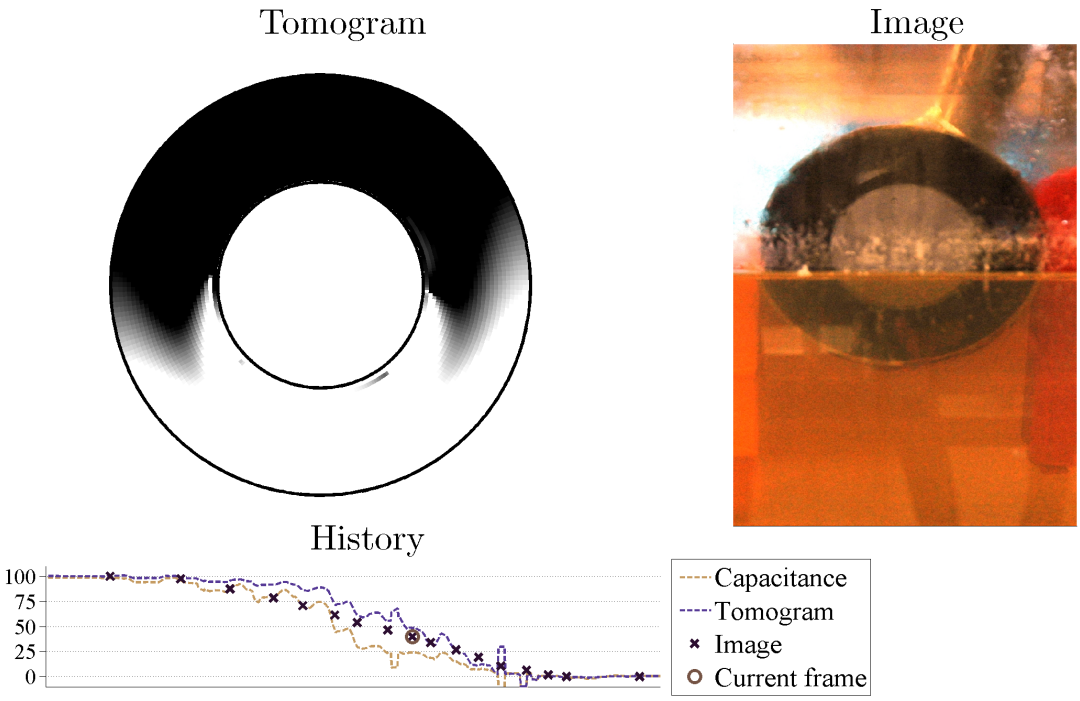

Figure C.26: T

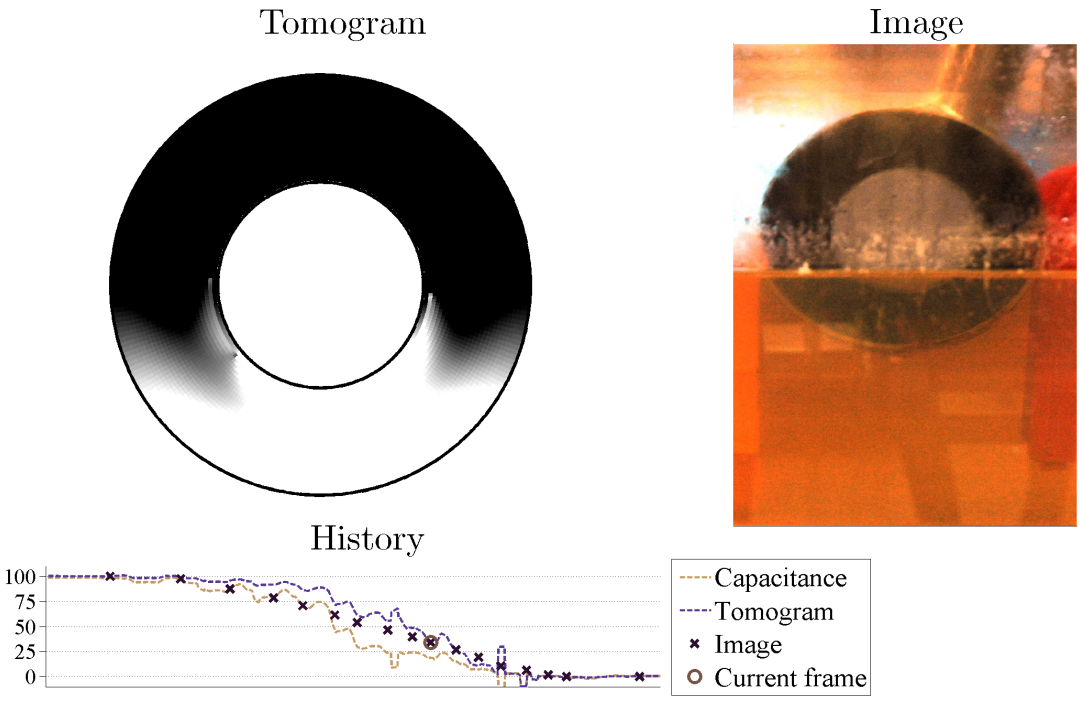

Figure C.27: T

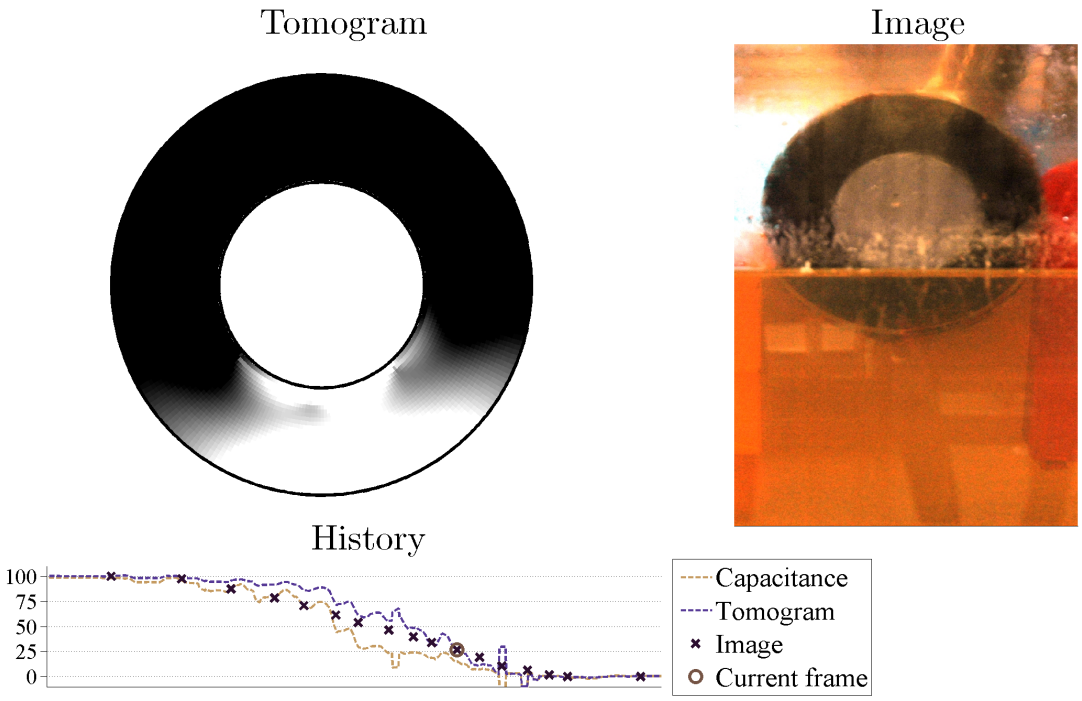

Figure C.28: T

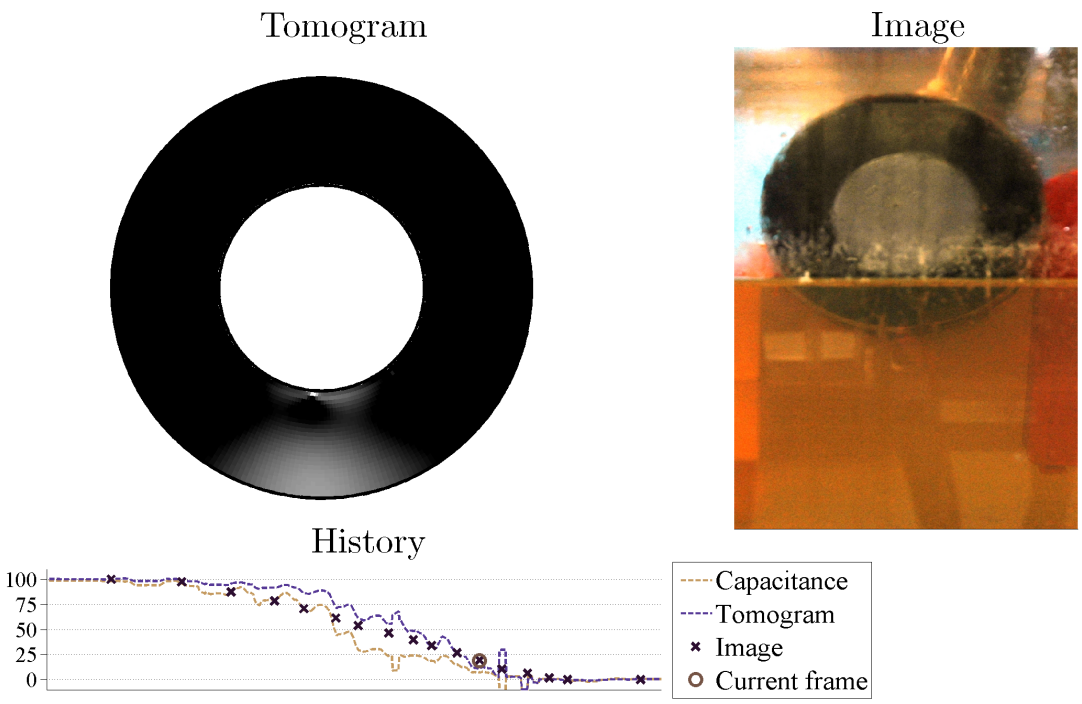

Figure C.29: T

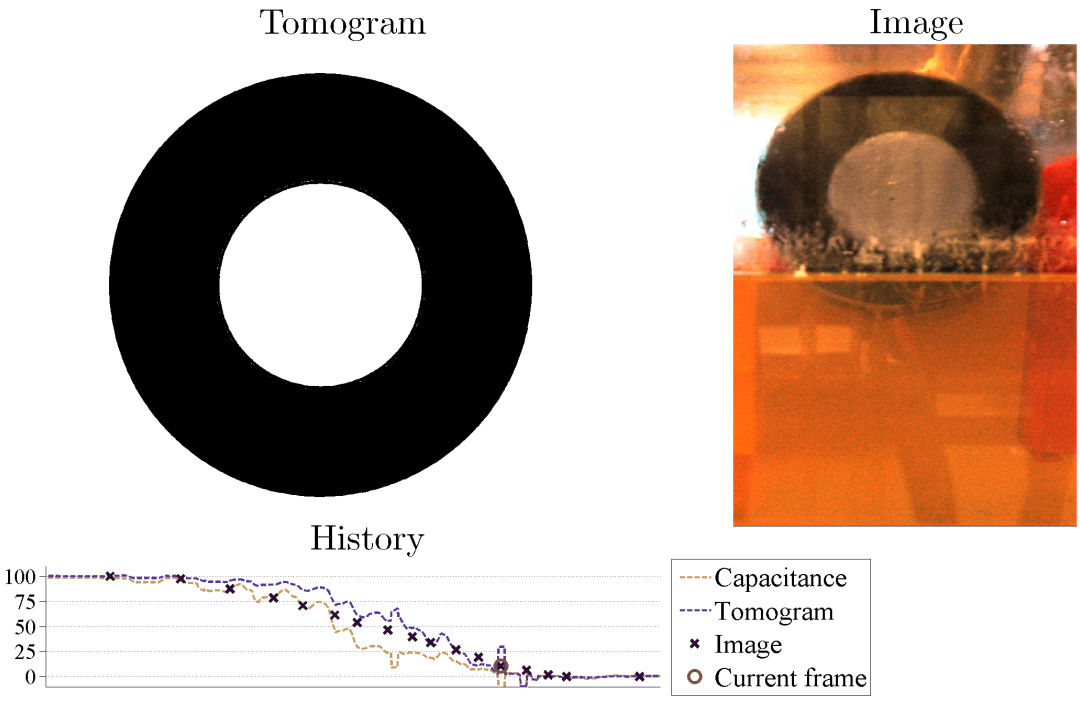

Figure C.30: T

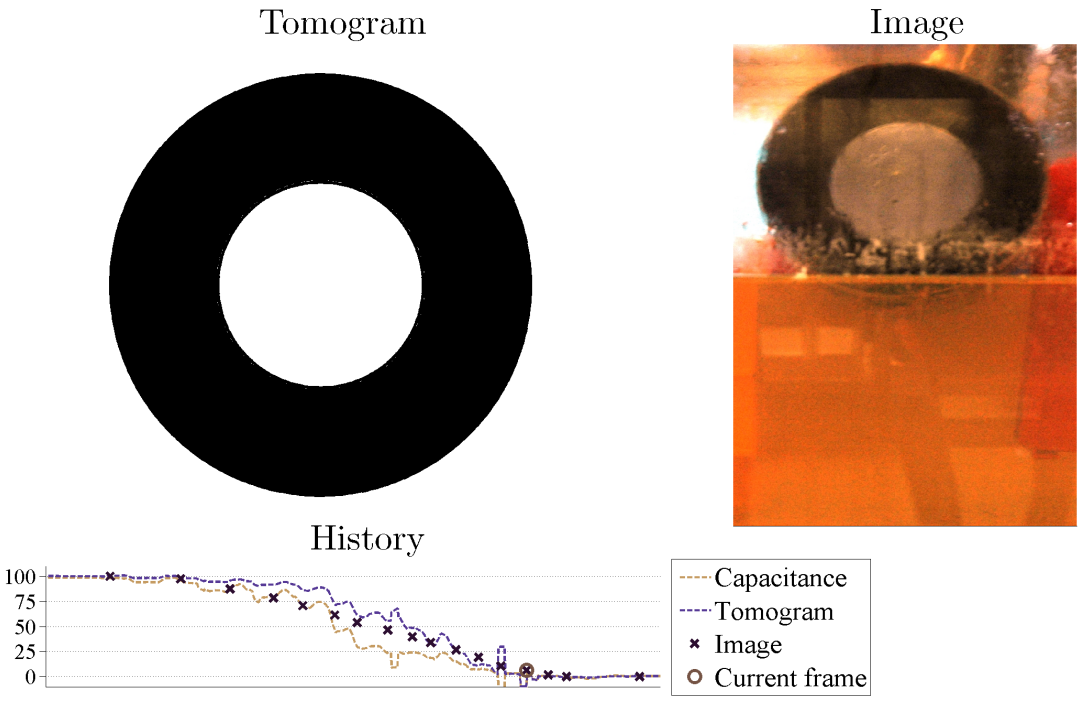

Figure C.31: T

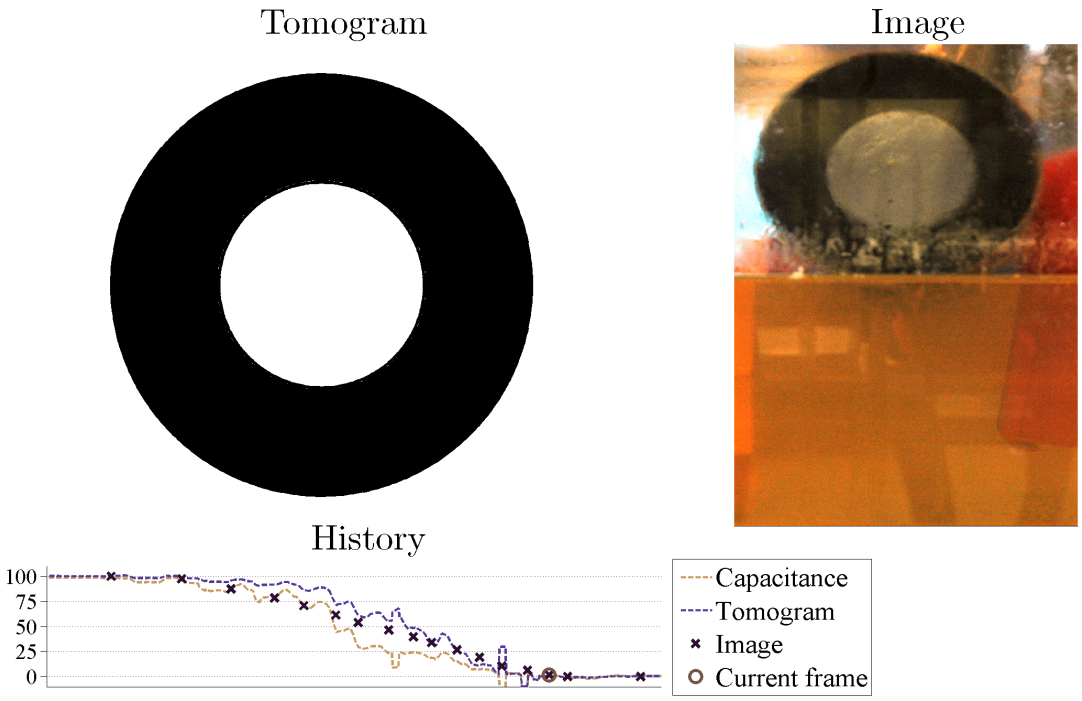

Figure C.32: T

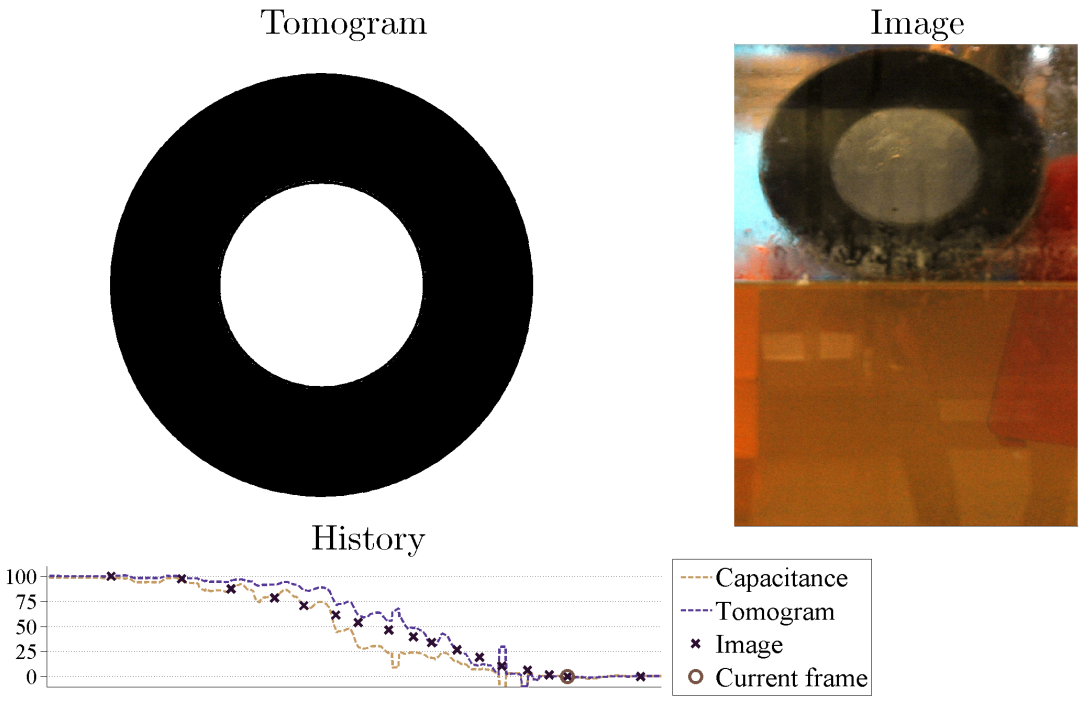

Figure C.33: T

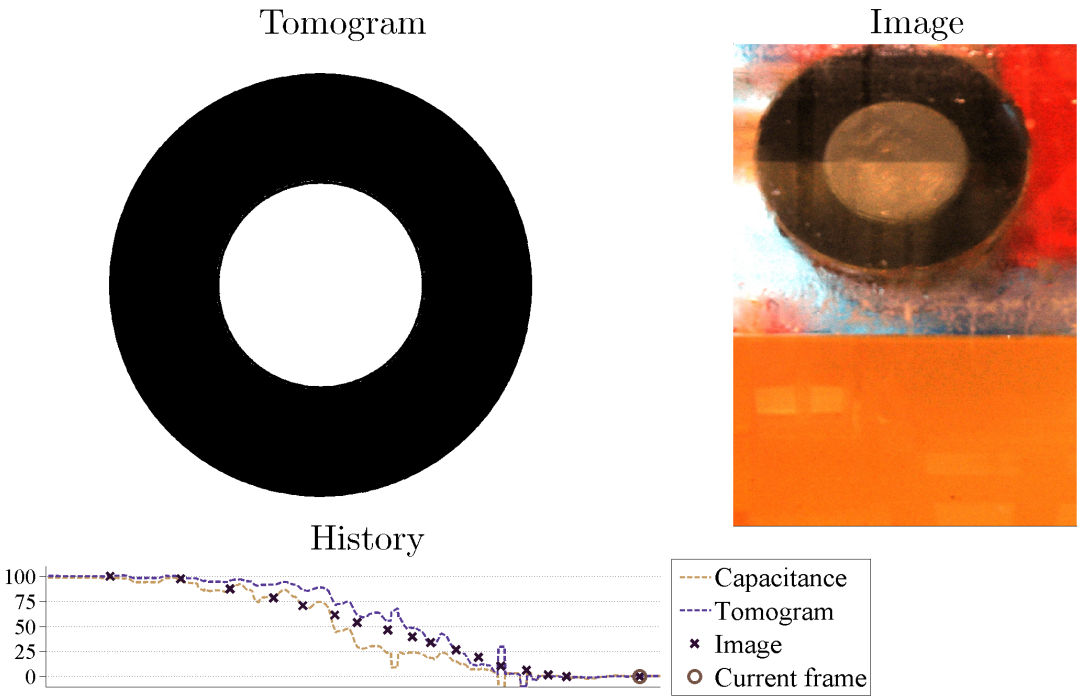
Tomogram
Image
History
100
75
50
25
0
Capacitance
Tomogram
Image
Current frame

Figure C.34: T

Appendix D

Testing the Sensor

To make sure that the sensor is performing in the intended way a set of tests were developed. The tests are a part of this report but developing a simple and effective set of tests was a goal in itself since it will help ensure that the WFI tools work before they are sent out to a Welltec base.

Test the excitation of the electrodes. Electrode 1 should be excited for the longest and electrode 8 should never be excited

D.1 Testing the circuits

The circuitry for the prototype sensor is distributed over 10 prints. Testing the working order of the circuits can be complicated, so a testing procedure has been devised. The testing procedure is useful both in the testing stage and later as a post-production test.

Applying a DC signal to an electrode is sufficient to perform a simple test. The two op-amps of the charge transfer circuit can then be tested, one by one, by selecting to connect the DC signal through their respective switches.

The resulting circuit layout is shown in figure D.1. The capacitors over the op-amps, have been omitted on the diagram since the excitation signal is constant. To test both sides of the circuit, the switches are closed alternately. When a switch is open (open circuit), the output from the corresponding op-amp is equal to the reference voltage on the input side (2.5V).

If the current injected into the electrode is directed into the op-amp A, the voltage on the op-amp B is thus 2.5V. The current is

$$i = \frac{V_{in} - 2.5V}{10k\Omega}$$

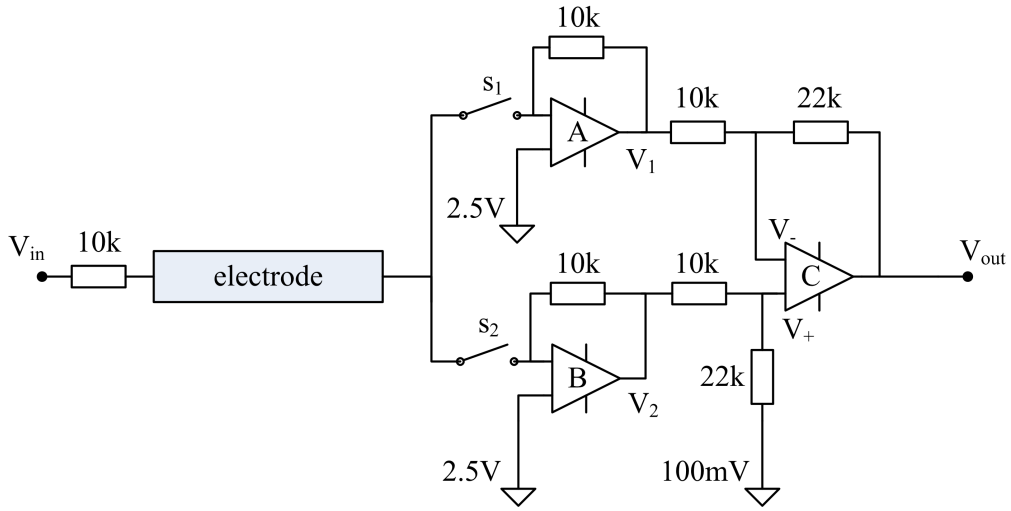

Figure D.1: The figure shows a schematic of how the circuit responds to the test input. A current is injected into the electrode through a resistor. The potential of the electrode will be kept at 2.5V by the op-amp which is connected to the electrode by closing one of the switches.

The same current must run through the resistor to the output node of the op-amp

$$\begin{aligned} 2.5V - V_n &= i \cdot 10k\Omega \\ V_n &= 2.5V - \frac{V_{in} - 2.5V}{10k\Omega} \cdot 10k\Omega \\ &= 5V - V_{in} \end{aligned}$$

The A and B op-amp are set up in the same way, so the op-amp B obeys the same relation between input and output voltage.

The output of op-amp C depends on which switch is open. If s_1 is closed, the op-amp receives 2.5V from op-amp B and vice versa.

$$V_- = \begin{cases} V_n & s_1 \text{ closed} \\ 2.5V & s_1 \text{ open} \end{cases} \qquad V_+ = \begin{cases} 2.5V & s_1 \text{ closed} \\ V_n & s_1 \text{ open} \end{cases}$$

When s_1 is open, s_2 is closed and vice versa. The potential V_2 is found by considering the current running into the 100mV reference.

$$V_+ = \frac{22}{32} V_2 + \frac{10}{32} 100mV$$

The current running from V_1 to V_{out} is

$$i = \frac{V_1 - V_-}{10k\Omega}$$

The output voltage must draw the same current through the 22kΩ resistor.

$$\begin{aligned} V_- - V_{out} &= i \cdot 22k\Omega \\ V_{out} &= V_- - \frac{V_1 - V_-}{10k\Omega} \cdot 22k\Omega \\ &= \frac{32}{10}V_- - \frac{22}{10}V_1 \\ &= 2.2(V_2 - V_1) + 100mV \end{aligned}$$

The output as a function of which switch is closed then becomes

$$\begin{aligned} V_{out} &= \begin{cases} 5.6V - 2.2V_n & s_1 \text{ closed} \\ 2.2V_n - 5.4V & s_1 \text{ open} \end{cases} \\ &= \begin{cases} 2.2V_{in} - 5.4V & s_1 \text{ closed} \\ 5.6V - 2.2V_{in} & s_1 \text{ open} \end{cases} \end{aligned}$$

If the output of the CT circuit behaves as predicted, the op-amps are working correctly and the resistors have been mounted correctly. The output does not depend on the capacitors, so it is still possible for the value of the capacitors to be wrong.

References

[1] S.M. Huang, A.B. Plaskowski, C.G. Xie, and M.S. Beck. Capacitance-based tomographic flow imaging system. *Electronics Letters*, 24(7):418–419, 1988.

[2] C.G. Xie, A. Plaskowski, and M.S. Beck. 8-electrode capacitance system for 2-component flow identification .1. Tomographic flow imaging. *IEE PROCEEDINGS-A-SCIENCE MEASUREMENT AND TECHNOLOGY*, 136(4):173–183, JUL 1989.

[3] W.Q. Yang. Hardware design of electrical capacitance tomography systems. *Measurement Science and Technology*, 7(3):225–232, 1996.

[4] B.S. Hoyle. Process tomography using ultrasonic sensors. *MEASUREMENT SCIENCE & TECHNOLOGY*, 7(3):272–280, MAR 1996.

[5] L.J. Xu, Y.T. Han, L.A. Xu, and J.S. Yang. Application of ultrasonic tomography to monitoring gas/liquid flow. *CHEMICAL ENGINEERING SCIENCE*, 52(13):2171–2183, JUL 1997. International Conference on Frontiers in Industrial Process Tomography, SAN LUIS OBISPO, CA, OCT 29-NOV 03, 1995.

[6] J. Carlson and R.K. Ing. Ultrasonic speckle correlation imaging of 2D particle velocity profiles in multiphase flows. *FLOW MEASUREMENT AND INSTRUMENTATION*, 14(4-5):193–200, AUG-OCT 2003.

[7] J. Westerweel. Fundamentals of digital particle image velocimetry. *MEASUREMENT SCIENCE & TECHNOLOGY*, 8(12):1379–1392, DEC 1997.

[8] R.D. Keane and R.J. Adrian. Theory of cross-correlation analysis of PIV images. *APPLIED SCIENTIFIC RESEARCH*, 49(3):191–215, JUL 1992.

[9] Flow scanner on Schlumberger webpage , April 2010. [online] `http://www.slb.com/services/production/production_logging/flow_scanner.aspx`.

[10] L.M. Fingerson. Thermal anemometry, current state, and future-directions. *REVIEW OF SCIENTIFIC INSTRUMENTS*, 65(2):285–300, FEB 1994.

[11] C. Tropea. Laser-Doppler anemometry - recent developments and future challenges. *MEASUREMENT SCIENCE & TECHNOLOGY*, 6(6):605–619, JUN 1995.

[12] S.R. Wylie, A. Shaw, and A.I. Al-Shamma'a. RF sensor for multiphase flow measurement through an oil pipeline. *MEASUREMENT SCIENCE & TECHNOLOGY*, 17(8):2141–2149, AUG 2006. 13th Conference on Sensors and Their Applications, Chatham, ENGLAND, SEP 06-08, 2005.

[13] A. Jaworek and A. Krupa. Gas/liquid ratio measurements by rf resonance capacitance sensor. *SENSORS AND ACTUATORS A-PHYSICAL*, 113(2):133–139, JUL 5 2004.

[14] W.J. Richards, M.R. Gibbons, and K.C. Shields. Neutron tomography developments and applications. *APPLIED RADIATION AND ISOTOPES*, 61(4):551–559, OCT 2004. 4th International Topical Meeting on Neutron Radiography, State Coll, PA, JUN 03-06, 2001.

[15] P. Reimers, J. Goebbels, H.P. Weise, and K. Wilding. Some aspects of industrial non-destructive evaluation by X-ray and gamma-ray computed tomography. *NUCLEAR INSTRUMENTS & METHODS IN PHYSICS RESEARCH SECTION A-ACCELERATORS SPECTROMETERS DETECTORS AND ASSOCIATED EQUIPMENT*, 221(1):201–206, 1984.

[16] I. Ismail, J.C. Gamio, S.F.A. Bukhari, and W.Q. Yang. Tomography for multi-phase flow measurement in the oil industry. *FLOW MEASUREMENT AND INSTRUMENTATION*, 16(2-3):145–155, APR-JUN 2005. 4th International Symposium on Measurement Techniques for Multiphase Flows, Hangzhou, PEOPLES R CHINA, SEP 10-12, 2003.

[17] U. Datta, T. Dyakowski, and S. Mylvaganam. Estimation of particulate velocity components in pneumatic transport using pixel based correlation with dual plane ECT. *CHEMICAL ENGINEERING JOURNAL*, 130(2-3, Sp. Iss. SI):87–99, JUN 1 2007. 4th World Congress on Industrial Process Tompgraphy, Aizu, JAPAN, SEP 05-08, 2005.

[18] C.G. Xie, S.M. Huang, B.S. Hoyle, R. Thorn, C. Lenn, D. Snowden, and M.S. Beck. Electrical Capacitance Tomography for Flow Imaging - System Model For Development of Image-Reconstruction Algorithms and Design of Primary Sensors. *IEE PROCEEDINGS-G CIRCUITS DEVICES AND SYSTEMS*, 139(1):89–98, 1992.

[19] S.M. Huang, J. Fielden, R.G. Green, and M.S. Beck. A New Capacitance Transducer for Industrial Applications. *JOURNAL OF PHYSICS E-SCIENTIFIC INSTRUMENTS*, 21(3):251–256, MAR 1988.

[20] R. Wajman, R. Banasiak, L. Mazurkiewicz, T. Dyakowski, and D. Sankowski. Spatial imaging with 3D capacitance measurements. *MEASUREMENT SCIENCE & TECHNOLOGY*, 17(8):2113–2118, AUG 2006.

[21] M.A. Nurge. Electrical capacitance volume tomography with high contrast dielectrics using a cuboid sensor geometry. *MEASUREMENT SCIENCE & TECHNOLOGY*, 18(5):1511–1520, MAY 2007.

[22] S.M. Huang, C.G. Xie, R. Thorn, D. Snowden, and M.S. Beck. Design of Sensor Electronics for Electrical Capacitance Tomography. *IEE PROCEEDINGS-G CIRCUITS DEVICES AND SYSTEMS*, 139(1):83–88, FEB 1992.

[23] S.M. Huang, R.G. Green, A. Plaskowski, and M.S. Beck. A High-Frequency Stray-Immune Capacitance Transducer Based on The Charge-Transfer Principle. *IEEE TRANSACTIONS ON INSTRUMENTATION AND MEASUREMENT*, 37(3):368–373, SEP 1988.

[24] W.Q. Yang. Further developments in an ac-based capacitance tomography system. *REVIEW OF SCIENTIFIC INSTRUMENTS*, 72(10):3902–3907, OCT 2001.

[25] D. Lu, F. Shao, and Z. Guo. A high voltage method for measuring low capacitance for tomography. *Rev Sci Instrum*, 80(5):053704, 2009.

[26] F.T. Kuhn and P.A. vanHalderen. Design of an active-differentiator-based capacitance transducer for electrical capacitance tomography. *MEASUREMENT SCIENCE & TECHNOLOGY*, 8(8):947–950, AUG 1997.

[27] K.J. Alme and S. Mylvaganarn. Electrical capacitance tomography - Sensor models, design, simulations, and experimental verification. *IEEE SENSORS JOURNAL*, 6(5):1256–1266, OCT 2006.

[28] W.Q. Yang and L Peng. Image reconstruction algorithms for electrical capacitance tomography. *Measurement Science and Technology*, 14(1):R1–R13, 2003.

[29] Jing Lei, Shi Liu, Zhihong Li, and Meng Sun. An image reconstruction algorithm based on the extended Tikhonov regularization method for electrical capacitance tomography. *MEASUREMENT*, 42(3):368–376, APR 2009.

[30] J.D. Jang, S.H. Lee, K.Y. Kim, and B.Y. Choi. Modified iterative Landweber method in electrical capacitance tomography. *MEASUREMENT SCIENCE & TECHNOLOGY*, 17(7):1909–1917, JUL 2006.

[31] G. Lu, L. Peng, B. Zhang, and Y. Liao. Preconditioned landweber iteration algorithm for electrical capacitance tomography. *Flow Measurement and Instrumentation*, 16(2-3):163 – 167, 2005. Tomographic Techniques for Multiphase Flow Measurements.

[32] H.S. Tapp, E.K. Kemsley, R.H. Wilson, and M.L. Holley. Image improvement in soft-field tomography through the use of chemometrics. *MEASUREMENT SCIENCE & TECHNOLOGY*, 9(4):592–598, APR 1998.

[33] G. Steiner. Application and data fusion of different sensor modalities in tomographic imaging. *Elektrotechnik und Informationstechnik*, 124(7-8):232–239, 2007.

[34] W.F. Fang and E. Cumberbatch. Matrix properties of data from electrical capacitance tomography. *JOURNAL of ENGINEERING MATHEMATICS*, 51(2):127–146, FEB 2005.

[35] W. Fang. Reconstruction of permittivity profile from boundary capacitance data. *APPLIED MATHEMATICS AND COMPUTATION*, 177(1):178–188, JUN 1 2006.

[36] COMSOL webpage , April 2010. [online] `http://www.comsol.com/products/multiphysics/`.

[37] M.X. Tang, W. Wang, J. Wheeler, M. McCormick, and X.Z. Dong. The number of electrodes and basis functions in EIT image reconstruction. *PHYSIOLOGICAL MEASUREMENT*, 23(1):129–140, FEB 2002.

[38] G. Wegmann, E.A. Vittoz, and F. Rahali. Charge injection in analog MOS switches. *IEEE JOURNAL OF SOLID-STATE CIRCUITS*, 22(6):1091–1097, DEC 1987.

[39] J. Hallundbæk and J. Kjærsgaard-Rasmussen. Logging tool. (09174664.4 - 1240), 12 2009.

[40] A.J. Rostocki, R. Wisniewski, and T. Wilczynska. High pressure phase transition in rape-seed oil. *Journal of Molecular Liquids*, 135(1-3):120 – 122, 2007.

[41] W.Q. Yang and T.A. York. New AC-based capacitance tomography system. *IEE PROCEEDINGS-SCIENCE MEASUREMENT AND TECHNOLOGY*, 146(1):47–53, JAN 1999.

[42] M.R. Rzasa. The measuring method for tests of horizontal two-phase gas-liquid flows, using optical and capacitance tomography. *NUCLEAR ENGINEERING AND DESIGN*, 239(4):699–707, APR 2009.

[43] J. Kjaersgaard-Rasmussen and W. Q. Yang. A Compact Electrical Capacitance Tomography System. In *2008 IEEE INTERNATIONAL WORKSHOP ON IMAGING SYSTEMS AND TECHNIQUES*, IEEE International Workshop on Imaging Systems and Techniques, pages 174–179, 345 E 47TH ST, NEW YORK, NY 10017 USA, 2008. IEEE, IEEE. IEEE International Workshop on Imaging Systems and Techniques, Chania, GREECE, SEP 10-12, 2008.

[44] Information about LabVIEW on National Instruments' webpage , April 2010. [online] `http://www.ni.com/labview/whatis/`.

DTU Mechanical Engineering
Section of Fluid Mechanics
Technical University of Denmark

Nils Koppels Allé, Bld. 403
DK- 2800 Kgs. Lyngby
Denmark
Phone (+45) 45 25 43 00
Fax (+45) 45 88 43 25

www.mek.dtu.dk